ISSN 0077–880X

THE UNIVERSITY OF
NEW SOUTH WALES

STUDIES FROM
SCHOOL OF CIVIL AND ENVIRONMENTAL ENGINEERING

3D FINITE ELEMENT MODELLING OF PUNCHING TYPE PROBLEMS USING DIANA

Y R KHWAOUNJOO, S J FOSTER, R I GILBERT

UNICIV REPORT No. R–393 AUGUST 2000
THE UNIVERSITY OF NEW SOUTH WALES
SYDNEY 2052 AUSTRALIA
http:/www.civeng.unsw.edu.au

ISBN : 85841 360 4

3D FINITE ELEMENT MODELLING OF PUNCHING TYPE PROBLEMS USING DIANA

by

Y.R. Khwaounjoo, BSc (Engineering) MEng

Doctoral Student, School of Civil and Environmental Engineering, UNSW

S.J. Foster BE MEngSc PhD

Senior Lecturer, School of Civil and Environmental Engineering, UNSW

R.I. Gilbert BE PhD

Professor, Head of School, Civil and Environmental Engineering, UNSW

ABSTRACT

The results of finite element analyses on concrete structures are influenced by many factors. Material models, aspect ratio and integration schemes being some of the most important. In this study the capability of the finite element program DIANA to model punching type problems is assessed using 20-node isoparametric brick elements and embedded bar elements.

The study is comprised of two parts. Part one deals with the degree of mesh refinement necessary to obtain accurate solutions. The behaviour of reinforced concrete slabs resting on a central square column with different amounts of steel are investigated. The results are compared with the results obtained from classical solutions for punching shear and with the yield line method for flexure.

Sensitivity tests of different parameters show that the results of the finite element analyses are influenced by many parameters. These parameters must be carefully selected in order to get the best possible results. The analyses show that the aspect ratio for elements away from the critical region can be increased without affecting the results. Two elements through the thickness of the slab are shown to be sufficient to obtain consistent results when using 20 node isoparametric brick elements. Compared to 3 x 3 x 3 Gaussian integration, a 2 x 2 x 2 numerical integration scheme gives good results without sacrificing the accuracy and significantly decreases the solution time.

The second part of the study deals with the analyses of different types of reinforced concrete problems to verify the versatility of DIANA. Conventionally reinforced as well as prestressed concrete structures were chosen from well-documented test reports. The conclusion is that DIANA is capable of modelling a wide range of nonlinear reinforced concrete problems including the complex punching shear problem in slab-column connections.

Key words: punching shear, DIANA, finite element, slab-column connections, reinforced concrete, prestressed concrete.

Table of Contents

List of symbols

A_{st}	Area of reinforcing steel
b	width of the panel
c	cohesion, a parameter
d	effective depth
d_0	diameter of the rigid plate/disk
d_1	maximum diameter of the failure surface
d_c	depth of a square column
E_c	modulus of elasticity of concrete
E_{cf}	slope of the softening branch
E_s	modulus of elasticity of steel
f	potential function
f_{cm}	cylinder strength of the concrete
f_{cp}	compressive strength of the in place concrete
f_{fc}	multiplying factor to get E_{cf}
f_{sy}	yield stress of the reinforcing bars
f_t	tensile strength of the concrete
g	plastic potential function
G_f	fracture energy
h	equivalent length of the mesh
h_0	depth of conical part in the failure surface
K	spring stiffness
l, m	material parameters for Nielsen et al. (1978) model
m	moment per unit length of the slab
P	projection matrix

P_{flex}	flexural load capacity
P_u	failure load in pullout of the plate embedded in the concrete
q	projection vector
α	threshold angle , tensioning softening parameter
β	shear retention factor
ϕ	angle of friction
ψ	dilatancy angle
ρ	steel reinforcement ratio
θ	inclination of punching failure surface with respect to the horizontal plane
ν	effectiveness factor
ξ	multiplier to E_c
κ	equivalent plastic strain, state variable
ϕ_0	initial angle of friction
$\{\varepsilon\}$	strain vector
$\{\sigma\}$, σ	stress vector
$\overline{c}$	equivalent cohesion
$\dot{\varepsilon}_3^p$	rate of plastic strain
$\dot{\kappa}$	rate of state variable

1 Introduction

1.1 General

The finite element method is a powerful tool for the analyses of the structures with many different types of elements available. The element type selected to solve a given problem depends on the problem being investigated. Whenever possible two-dimensional models are used due to the relatively large time, and hence cost, associated in performing three-dimensional analyses. However for particular types of problems, such as punching shear, nonlinear three dimensional analyses are required to accurately model the structure (Park and Gamble, 1980, Sunidja et al., 1982). For these models 20-node isoparametric brick elements are the most popular and most widely used elements because of their efficiency and accuracy. In fact, the results of any finite element analysis depend on many factors. For example, element aspect ratio, element type, integration scheme, discretization pattern are some of the major factors that can influence the results of solid models. Many studies have already been undertaken on the accuracy of finite element modelling. For example, studies by Noor and Bubuska (1987), Roddemann and Jansen (1993), Chiang and Tang (1995), Chiang and Lee (1994) have shown that the accuracy of the finite element analysis depends on the suitability of element being used to model the problem being investigated.

In this study the suitability of DIANA (1997) to model punching type problems is investigated. The elements used are the 20-node concrete elements with embedded reinforcement, mesh patterns integration schemes and material parameters being investigated. A number of different problem types are also investigated in order to review the versatility of the model.

1.2 Objectives

The specific objectives of this study are:

- investigate different material models for 3D finite element modelling of punching type problems.
- investigate various finite element meshes.
- study the effect of different integration schemes on the solution time and accuracy.
- verify the applicability of DIANA for the modelling of punching type problems.

1.3 Scope

The results of any finite element modelling are affected by mesh type, size and arrangement. In this study punching type problems involving simple reinforced and unreinforced plates were investigated using solid elements with three translational degrees of freedom per node. The primary variables studied are the element aspect ratio and the number of element layers required through the thickness of the slab to accurately model the failure. The problems were formulated considering punching and pullout tests on plain and reinforced concrete panels. The pullout of a solid plate embedded in plain concrete was studied using different meshes and behaviour of reinforced concrete slabs with different quantities of reinforcement were also studied.

In the second part of the study the results of the finite element analyses on different test specimens were compared with test data to verify the finite element model. The findings of the first part of the study were implemented in the second part of the study.

1.4 Organisation of the Report

The report consists of seven sections. The different material models for the concrete and the reinforcing steel are discussed in Section 2. A brief account of the solution procedure adopted in the analyses is also given.

Section 3 deals with the aspect ratio and the integration scheme used (2 x 2 x 2 and 3 x 3 x 3 Gaussian integration schemes are investigated).

The effect of reinforcement content in the load carrying capacity of slabs is presented in Section 4.

In Section 5, the sensitivity of the different finite element modelling parameters are discussed on the basis of ultimate load, load-deflection and load-steel strain histories.

Verification of the finite element model against experimental studies is presented in Section 6. The influence of specific parameters and boundary conditions of the test specimen in the response of punching problem of flat plate-column connections are also reviewed.

The conclusions of the study are presented in Section 7.

2 Material Modelling and Solution Procedure

2.1 Introduction

Different material models are used to represent the behaviour of the concrete and the reinforcing steel at various stress states. In this study the model developed by Rots (1988) and implemented in DIANA version 6.2 (1997) is used. A smeared tension cracking model for the concrete with a plasticity model for compression is used and is discussed briefly in the following sections.

2.2 General Constitutive Relationships

For small displacements, without an appreciable change in geometry the total strain ε can be decomposed into an elastic component (ε^e) and an inelastic (plastic) component (ε^p). That is,

$$\varepsilon = \varepsilon^e + \varepsilon^p \tag{2.1}$$

The flow theory of plasticity is implemented to describe the elasto-plastic material behaviour. The total stress at any time (t) is a function of the total strain ε and it is also a function of stress and strain history. The stress and strain history of the material is taken into account implicitly by introducing an internal parameter κ, which is governed by a specific evolutionary law. Here κ represents an equivalent plastic strain of the concrete at different levels of stress. The elastic relationship between the total stress σ and the elastic strain ε^e is given by

$$\sigma = D\varepsilon^e \tag{2.2}$$

where

$$\sigma = \begin{bmatrix} \sigma_{xx} & \sigma_{yy} & \sigma_{zz} & \sigma_{xy} & \sigma_{yz} & \sigma_{zx} \end{bmatrix}^T ; \tag{2.3a}$$

$$\varepsilon^e = \begin{bmatrix} \varepsilon^e_{xx} & \varepsilon^e_{yy} & \varepsilon^e_{zz} & \gamma^e_{xy} & \gamma^e_{yz} & \gamma^e_{zx} \end{bmatrix}^T \tag{2.3b}$$

The material elasticity relationship, D, is given by

$$D = \frac{E(1-\mu)}{(1+\mu)(1-2\mu)} \begin{bmatrix} 1 & E^* & E^* & 0 & 0 & 0 \\ E^* & 1 & E^* & 0 & 0 & 0 \\ E^* & E^* & 1 & 0 & 0 & 0 \\ 0 & 0 & 0 & G^* & 0 & 0 \\ 0 & 0 & 0 & 0 & G^* & 0 \\ 0 & 0 & 0 & 0 & 0 & G^* \end{bmatrix} \tag{2.4}$$

where E is the elastic modulus, μ the Poisson's ratio, $E^* = \frac{\mu}{(1-\mu)}$ and $G^* = \frac{(1-2\mu)}{2(1-\mu)}$.

The yield condition governs the state of stress at the initiation of plastic flow. The yield condition is a function of the stress vector and the internal state parameter (a is a hardening parameter). If the value of the yield condition is less than zero, the system is in an elastic state. A state with the yield condition greater than zero is not admissible for rate-independent plasticity. Therefore, the yield condition is given by

$$f(\sigma, \kappa) = 0 \tag{2.5}$$

The inelastic strain rate vector is a function of the state of stress and for the j-th plastic potential functions $g_j = g_j(\sigma, \kappa)$ $(j = 1,n)$ and is given by

$$\dot{\varepsilon}^p = \sum_{j=1}^{n} \dot{\lambda}_j \frac{\partial g_i}{\partial \sigma} \tag{2.6}$$

The proportionality constant $(\dot{\lambda}_j)$ is a scalar such that $\dot{\lambda}_j \geq 0$. If the yield function is less than zero, no plastic flow will occur and $\dot{\lambda}_j = 0$.

The evolution of the internal state parameter $\dot{\kappa}$ is given as a function of the stress vector σ and the plastic strain rate vector $\dot{\varepsilon}^p$, ie. $\dot{\kappa} = \dot{\kappa}(\sigma, \dot{\varepsilon}^p)$. Using the consistency condition $\dot{f} = 0$ the relationship between the stress rate vector and the strain rate vector is derived as

$$\dot{\sigma} = \left[D - \frac{D \frac{\partial g}{\partial \sigma} \frac{\partial f}{\partial \sigma}^T D}{E_P + \frac{\partial f}{\partial \sigma}^T D \frac{\partial g}{\partial \sigma}} \right] \dot{\varepsilon} \qquad \text{..... where} \quad E_P = -\frac{\partial f}{\partial k} \frac{\partial \kappa}{\partial \lambda} \tag{2.7}$$

Concrete possesses a nonlinear volume change during hardening. Experimental results indicate that under compressive loadings, inelastic volume contraction occurs at the

initiation of yielding and volume dilatation occurs at about 75 to 90 percent of the ultimate stress (Chen and Han, 1987). Inflection points are usually observed and this sort of behaviour violates the associated flow rule. A plastic potential function g other than the loading function f is therefore required to define the flow rule. In such cases a non-associated flow rule $f \neq g$ is adopted. For $f \neq g$ the tangent stiffness matrix on the right hand side of equation 2.7 becomes asymmetric.

2.3 Concrete in Compression

The compression behaviour of the concrete was modelled using a nonlinear constitutive law. The uniaxial compression curve, shown in Figure 2.1, is represented by a cohesion-equivalent plastic strain. Effects of confinement provided by triaxial compressive stresses (if any) are modelled using the Drucker-Prager yield criterion. The general yield condition of this model in principal stress space is

$$f(\sigma,\kappa)=\sqrt{\tfrac{1}{2}\sigma^T P\sigma}+\alpha_f q\sigma-\beta_0\bar{c}(\kappa) \tag{2.8}$$

where $\sigma=\{\sigma_1\sigma_2\sigma_3\sigma_{12}\sigma_{23}\sigma_{31}\}^T$, q is the projection vector given by $q=\{1\,1\,1\,0\,0\,0\}$ and P is the projection matrix, where

$$P=\begin{bmatrix} 2 & -1 & -1 & 0 & 0 & 0 \\ -1 & 2 & -1 & 0 & 0 & 0 \\ -1 & -1 & 2 & 0 & 0 & 0 \\ 0 & 0 & 0 & 6 & 0 & 0 \\ 0 & 0 & 0 & 0 & 6 & 0 \\ 0 & 0 & 0 & 0 & 0 & 6 \end{bmatrix} \tag{2.9}$$

The scalars α_f and β are given by

$$\alpha_f=\frac{2\sin\phi(\kappa)}{3-\sin\phi(\kappa)} \qquad \beta_0=\frac{6\cos\phi_0}{3-\sin\phi_0} \tag{2.10}$$

where ϕ is the angle of internal friction, ϕ_0 the initial angle of internal friction, c the cohesion, $\bar{c}(\kappa)$ is an equivalent cohesion and is a function of the equivalent plastic strain, κ.

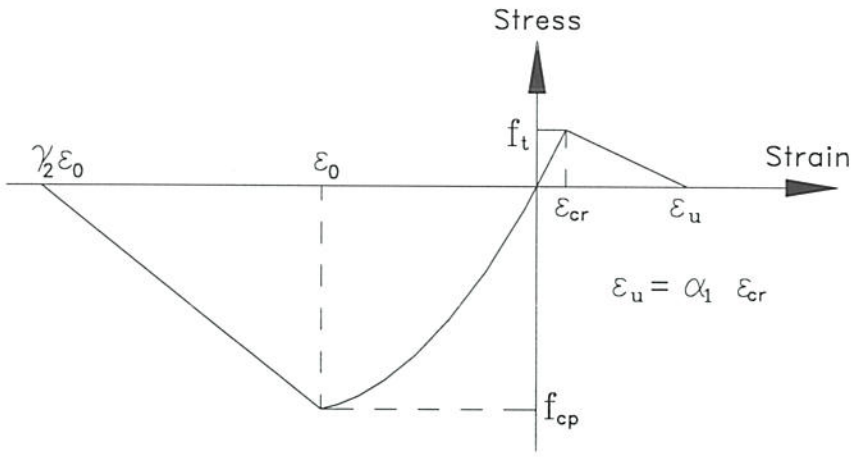

Figure 2.1 - Stress-strain curve for concrete in uniaxial compression and tension.

The Drucker-Prager yield condition with tension cut-off is shown in Figure 2.2. In this figure it is shown that the deviatoric stress vector r ($r = \sqrt{2\,J_2}$) makes an angle θ with the first principal stress in the state of stress projected on the deviatoric plane. The length along the hydrostatic axis (ξ) is given by $\xi = I_1/\sqrt{3}$. The first invariant of the stress tensor, I_1 and the second invariant of the deviatoric stress tensor, J_2 are given by

$$I_1 = \sigma_1 + \sigma_2 + \sigma_3 \tag{2.11a}$$

$$J_2 = \frac{1}{6}\left[(\sigma_1 - \sigma_2)^2 + (\sigma_2 - \sigma_3)^2 + (\sigma_3 - \sigma_1)^2\right] \tag{2.11b}$$

where σ_i *(i=1, 2, 3)* are principal stresses and r', ξ' are values of r and ξ corresponding to the tensile strength of the concrete, f_t.

After yielding of the concrete a non-associated flow rule is used with the plastic potential (g) given by,

$$g(\sigma, \kappa) = \sqrt{\tfrac{1}{2}\sigma^T P \sigma} + \alpha_g q \sigma \tag{2.12}$$

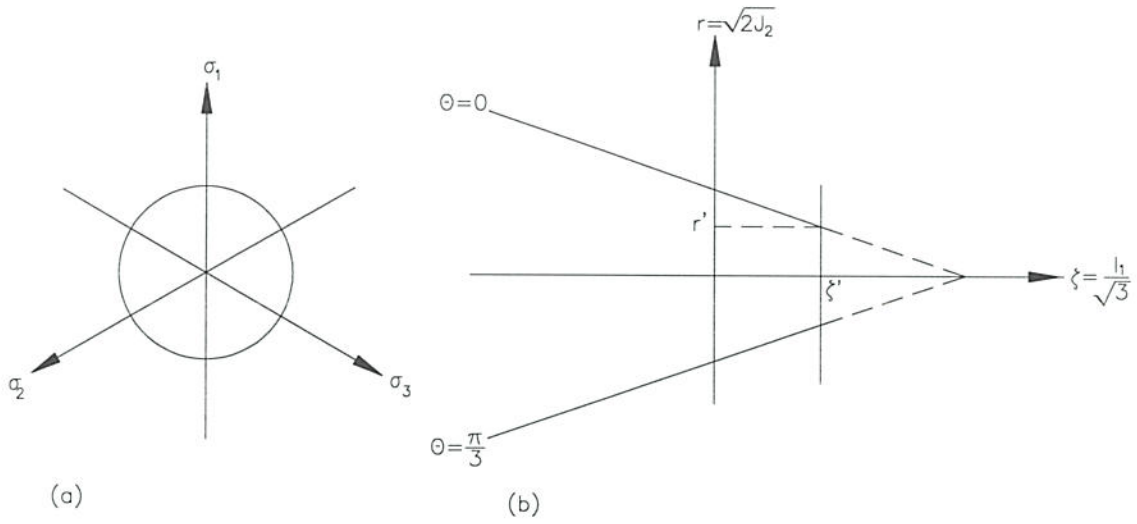

Figure 2.2 - Drucker-Prager yield condition with tension cut-off (a) π-Plane b) Meridian planes $\theta = 0^{\circ}$ and $\theta = \pi/3$.

with

$$\alpha_g = \frac{2\sin\psi(\kappa)}{3-\sin\psi(\kappa)} \tag{2.13}$$

and where $\psi(\kappa)$ is the dilatancy angle required to model volume changes due to shear distortions. The dilatancy angle represents the ratio of plastic volume change over plastic shear strain. For three-dimensional structures under low levels of confinement $\psi(\kappa)$ was found to affect the load carrying capacity (Vermeer and de Borst, 1984) but its effect vanishes with high confining pressures and ranges from 0 to 20 degrees. The relationship between the friction angle (ϕ) and the dilatancy angle (ψ) is taken as

$$|\phi - \psi| \leq 20^0 \tag{2.14}$$

The relationship between the state variable and the rate of plastic strain in the minor principal direction ($\dot{\varepsilon}_3^p$) is given by

$$\dot{\kappa} = -\frac{\sqrt{1+2\alpha_g^2}}{1-\alpha_g}\dot{\varepsilon}_3^p \tag{2.15}$$

For the case of uniaxial compression, the equivalent cohesion, $\overline{c}$, is

$$\bar{c} = f_{cp}\frac{1-\alpha_f}{\beta_0} \tag{2.16}$$

where f_{cp} is the uniaxial compression strength of the concrete and α_f and β_0 are as defined by equation 2.10.

For concrete, the angle of internal friction is reported to be within the range of 30 to 35 degrees (Vermeer and de Borst, 1984), although in some cases angles as high as $\phi = 37^\circ$ have been used (Nielsen et al., 1978). In this study the angle of internal friction was taken as $\phi = 30^\circ$. The cohesion–plastic strain curve for the concrete (pre-peak) is based on the concrete stress-strain curve generated using Hognestad's (1951) stress-strain model with a strain in the concrete at the peak uniaxial compression stress of 0.002. In this study the dilatancy angle was taken as $\psi = 12.6^\circ$, as recommended by Vermeer and de Borst (1984).

2.4 Cracked Concrete

The multi-directional smeared crack model of de Borst and Nauta (1985) and Rots (1988) is used for the cracked concrete. The total strain ε is decomposed into an elastic strain ε^e and a crack strain ε^{cr}, that is

$$\varepsilon = \varepsilon^e + \varepsilon^{cr} \tag{2.17}$$

The strain vectors in equation 2.17 relate to the global coordinate axes and for the three dimensional configuration they have six components. The global crack strain vector ε^{cr} is given as

$$\varepsilon^{cr} = \left[\varepsilon_{xx}^{cr} \quad \varepsilon_{yy}^{cr} \quad \varepsilon_{zz}^{cr} \quad \gamma_{xy}^{cr} \quad \gamma_{yz}^{cr} \quad \gamma_{zx}^{cr}\right]^T \tag{2.18}$$

where x, y, and z refer to global coordinate axes. The crack stress-strain laws are defined with the local coordinate system aligned with the crack plane as shown in Figure 2.3. The crack traction vector e^{cr} in local coordinates is

$$e^{cr} = \left[\varepsilon_{nn}^{cr} \quad \gamma_{ns}^{cr} \quad \gamma_{nt}^{cr}\right]^T \tag{2.19}$$

where ε_{nn}^{cr} is the normal strain for the mode I crack and γ_{ns}^{cr}, γ_{nt}^{cr}, respectively, are the shear strains for the mode II and mode III cracks and the subscripts n, s, and t refer to the local material coordinate axes (see Figure 2.3). The relationship between local crack strain e^{cr} and global crack strain ε^{cr} is

$$\varepsilon^{cr} = N\, e^{cr} \tag{2.20}$$

where N is the transformation matrix

$$N = \begin{bmatrix} l_x^2 & l_x l_y & l_z l_x \\ m_x^2 & m_x m_y & m_z m_x \\ n_x^2 & n_x n_y & n_z n_x \\ 2l_x m_x & l_x m_y + l_y m_x & l_z m_x + l_x m_z \\ 2m_x n_x & m_x n_y + m_y n_x & m_z n_x + m_x n_z \\ 2n_x l_x & n_x l_y + n_y l_x & n_z l_x + n_x l_z \end{bmatrix} \tag{2.21}$$

and where l_x, m_x and n_x are the direction cosines for the strain normal to the crack plane (n-axis) relative to the global co-ordinate system (similarly the direction cosines with the subscript y refer to the s-axis and those with the subscript z to the local t-axis).

The traction across the crack is defined by a vector t^{cr} and is expressed as

$$t^{cr} = \begin{bmatrix} t_n^{cr} & t_s^{cr} & t_t^{cr} \end{bmatrix}^T \tag{2.22}$$

where t_n^{cr} is the mode I normal traction and t_s^{cr}, t_t^{cr} are mode II and mode III shear tractions, respectively. The relationship between the global stress and the local tractions are given by

$$t^{cr} = N^T \sigma \tag{2.23}$$

In the case of the multi-directional cracks that simultaneously occur at a sampling point, the crack strain ε^{cr} is further decomposed as the sum of the global primary crack ε_1^{cr} and the global crack strain increment owing to the secondary cracks, that is

$$\varepsilon^{cr} = \varepsilon_1^{cr} + \varepsilon_2^{cr} + \ldots\ldots \tag{2.24}$$

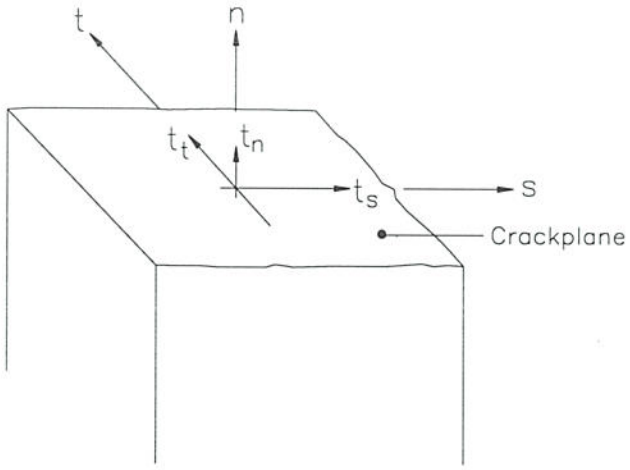

Figure 2.3 – Local coordinate system and traction across a crack.

Each (fixed) crack is assigned its own local crack strain vector e_i^{cr}, its own traction vector t_i^{cr} and its own transformation matrix N_i according to equations 2.19 to 2.22.

The relationship between the crack-strain and traction for the multi-crack system is

$$t^{cr} = \hat{D}^{cr}\, e^{cr} \tag{2.25}$$

where

$$t^{cr} = \begin{bmatrix} t_1^{cr} & t_2^{cr} & t_3^{cr} \end{bmatrix}^T ; \qquad \hat{D}^{cr} = \begin{bmatrix} D_{11}^{cr} & D_{12}^{cr} & \ldots \\ D_{21}^{cr} & D_{22}^{cr} & \ldots \\ \ldots & \ldots & \ldots \end{bmatrix} \quad \text{and} \quad e^{cr} = \begin{bmatrix} e_1^{cr} & e_2^{cr} & \ldots \end{bmatrix}^T .$$

Finally the relationship between global stress σ and global strain ε is given by

$$\sigma = \left[D^{co} - D^{co}\, \hat{N} \left[\hat{D}^{cr} + \hat{N}^T\, D^{co}\, \hat{N} \right]^{-1} \hat{N}^T D^{co} \right] \varepsilon \tag{2.26}$$

where D^e is stiffness matrix corresponding to elastic strain (Rots, 1988). The cracking stiffness $\hat{D}^{cr}$ is the corresponding matrix assembled for all the cracks formed at a sampling point with D^{cr} for the n-th crack denoted as D_n^{cr} and given by

$$D_n^{cr} = \begin{bmatrix} \frac{E\,E_t}{E-E_t} & 0 & 0 \\ 0 & \frac{\beta}{1-\beta}\frac{E}{2(1+\mu)} & 0 \\ 0 & 0 & \frac{\beta}{1-\beta}\frac{E}{2(1+\mu)} \end{bmatrix} \tag{2.27}$$

where E and E_t are the tangent moduli of elasticity for the ascending and descending branches of the concrete stress strain relationship for tension. The Poisson's ratio is given by μ and β is a shear retention factor to account for the effects of aggregate interlock and dowel shear. The transformation matrix for n cracks is

$$\hat{N} = [N_1 \quad N_2 \quad N_3 \quad \ldots \quad \ldots] \tag{2.28}$$

For concrete in tension a linear tension cut-off model was used with smeared cracking added to the plasticity model discussed above. A crack arises if the major principal tensile stress (σ_1) exceeds either the uniaxial tensile strength of the concrete or if

$$\sigma_1 \geq f_t\left(1 + {}^{\sigma_3}\!/_{f_c}\right) \tag{2.29}$$

where σ_3 is the minor principal stress and f_{cp} is the strength of the concrete. Multiple cracking at a gauss point can occur provided that the principal tensile stress exceeds the maximum stress condition and the angle between the principal tensile stress and an existing crack exceeds a threshold angle α.

With the use of a threshold angle the number of possible crack formations at a point is controlled between the fixed single crack model (α = 90 degrees) and the rotating crack model (α = 0 degree). In this investigation a value of α = 15 degrees was used.

The uniaxial stress-strain curve used for modelling the concrete is shown in Figure 2.1. In the case of plain concrete, crack propagation and fracture are primarily dependent on the behaviour of the material in tension. It has been well established that this response is primarily controlled by the formation of micro-cracks (Rots et al., 1985). Upon loading, a limited numbers of such cracks can develop anywhere in the specimen but if at a point in the specimen the tensile stress reaches the limiting strength (f_t) all additional deformation due to micro-cracking localises within the fracture zone. In the fracture zone the stress

gradually decreases while the strain increases. This phenomenon is known as tensile strain softening.

After cracking the stiffness of the reinforced concrete structure is reduced. However, a concrete block between two adjacent cracks is capable of resisting tensile forces by the bond between the concrete and the reinforcement. Due to the tension stress between cracks caused by the influence of the bonded reinforcement a higher stiffness is observed in the reinforced concrete as compared with the effect of the reinforcement alone. This is referred to as tension stiffening.

A number of models have been developed to consider the tension stiffening effect. The first approach to modelling tension stiffening was introduced by Scanlon (1971). Scanlon used a modified stress-strain curve for the concrete in tension by assigning a component to the descending branch to account for the retained stiffness upon cracking. Gilbert and Warner (1978) artificially increased the stiffness of the reinforcing bars by modifying the stress-strain response of steel. This method produced satisfactory results in different reinforced concrete slab analysed by Gilbert and Warner (1978). However, its application in analysing orthogonally reinforced concrete panels was not always as successful (Hu and Schnobrich, 1988). Lin et al. (1975), Cope (1986) and Prakhya and Morley (1990) developed various approaches based on experimental observations to incorporate the tension stiffening effect. Others such as Petersson and Gustavasson (1980), Bazant and Oh (1983, 1984) and Sih and DiTommaso (1985) developed models using a fracture energy approach.

In this investigation the tension softening and tension stiffening effects in the cracked concrete were simulated using the simple linear tension-softening model, as shown in Figure 2.1. The slope of the descending branch is adjusted to allow for tension softening and tension stiffening using the model of van Mier (1987). The strain for zero stress, post cracking (ε_u) is expressed in terms of the cracking strain (ε_{cr}) such that

$$\varepsilon_u = \alpha_1 \varepsilon_{cr} = 2G_f / h\ f_t \qquad \text{(for unreinforced concrete sections)} \qquad (2.30a)$$

$$\varepsilon_u = \alpha_1 \varepsilon_{cr} = \alpha_2 f_y / Es \qquad \text{(for reinforced concrete sections)} \qquad (2.30b)$$

where $\varepsilon_{cr} = f_t / E_c$; G_f is the fracture energy; h is the crack band width (equivalent length of the mesh); f_t is the tensile strength of the concrete and E_s and E_c are moduli of elasticity of steel and concrete, respectively. For solid elements h is calculated as the cube root of the volume of the elements.

Different investigators have selected various shapes for the softening response of concrete in tension and different strain levels for ε_u. In most cases the selection of the multiplier α_1 depended on the experience of the analyst with the specific problem. For example, Lin (1973) used a value of about $\alpha_1 = 5$, Gilbert and Warner (1978) and Al-Manaseer and Phillips (1987) adopted a value of $\alpha_1 = 10$. Abdel-Rahman (1982) assigned values between $\alpha_1 = 10$ and $\alpha_1 = 25$ and van Mier (1987) used $\alpha_1 = \alpha_2 \frac{E_c}{E_s} \frac{f_{sy}}{f_t}$ where α_2 is in the range of 0.3 to 0.8. Barzegar and Schnobrich (1990) presented different expressions for different problem types for ultimate cracking strain using a nonlinear tension-stiffening model similar to that used by Scanlon (1971). In summary the tension stiffening effect is considered in different ways by different investigators based on the experience of the investigator.

In this study, equation 2.30 is used with $\alpha_2 = 0.5$ for reinforcing bars with $f_{sy} \leq 550$ MPa and $\alpha_2 = 0.4$ for bars with $f_{sy} > 550$ MPa. Sensitivity tests for the influence of ε_u are presented in Section 6.

The development of cracks in concrete reduces the shear stiffness but (not to zero) because of aggregate interlock (Suidan and Schnobrich 1973, Channakeshava and Iyengar 1988, Barzegar 1989). This effect is taken into account by the introduction of a shear retention factor (β). In this study a constant shear retention factor is used with $\beta = 0.2$ unless stated otherwise. Sensitivity testing for the influence of β is presented in Section 6.

2.5 Reinforcing steel

A bi-linear or tri-linear elasto-plastic model was adopted for the conventional and prestressing reinforcement as shown in Figure 2.4a and Figure 2.4b, respectively. In Figure 2.4b, f_{sy1} is the steel stress corresponding to the strain of ε_{sy1} and E_P is the tangent

modulus of the steel stress-strain diagram in the post elastic region. Perfect bond was assumed between the concrete and all conventional reinforcement and for the prestressing steel when grouted prestressing systems were used.

2.6 Solution Procedure

Many solution procedures are available to solve the nonlinear finite element problems. The solution procedure adopted is important as it influences the time required for solution, disk space and the accuracy of the results. In nonlinear problems the solution procedure has to be carefully chosen in order to get the results efficiently without losing accuracy of solution.

In this study a modified Newton Raphson iteration procedure was used with the stiffness matrix updated at the start of each load step. Load control was used in the early (elastic) part of the analyses and load-displacement control via an updated normal arc-length procedure was used in the latter part of the analyses. Except where mentioned specifically convergence was set at 1 percent of the energy norm with a maximum of 50 iterations for any one load step.

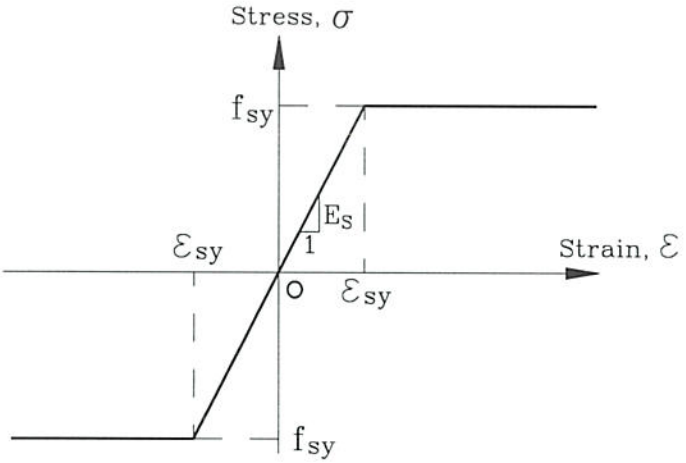

(a) Elasto-plastic bi-linear stress-strain curve.

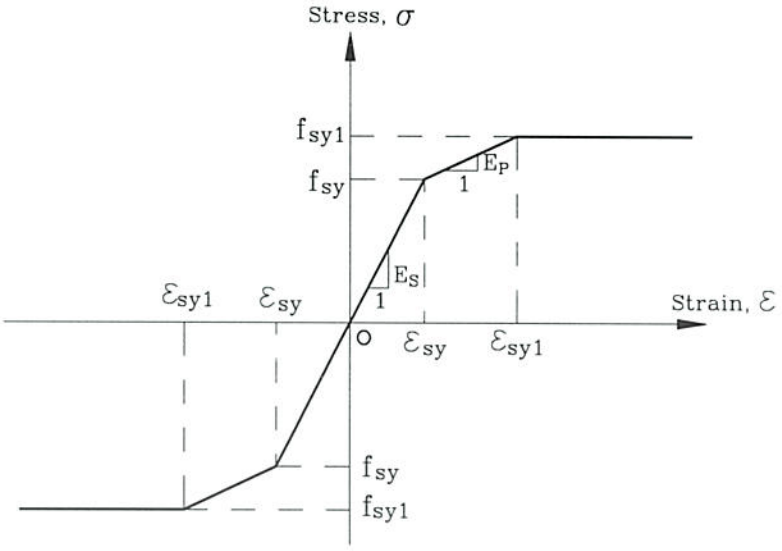

(b) Elasto-plastic tri-linear stress-strain curve

Figure 2.4 – Material model for steel.

3 Sensitivity of Mesh Grading and Integration

3.1 Introduction

The accuracy of the solutions obtained using finite element modelling depends on many factors with mesh grading, the element aspect ratio and the integration scheme being some of the most important. The effects of the element aspect ratio and the number of Guassian integration points, both in plan and through the section, for punching problems are discussed in this section. The analyses were carried out using 20-node solid isoparametric elements with Gaussian integration on a 2 x 2 x 2 or 3 x 3 x 3 quadrature.

3.2 Pullout of an Embedded Plate

To study the effects of aspect ratio on punching type problems a plate of uniform thickness was modelled under a centrally applied load. Meshes of different aspect ratio are considered. The slab, shown in

Figure 3.1, consisted of a concrete plate of 1.7 m square in plan and with a 100 mm square rigid plate embedded at a depth of 100 mm from top surface of the slab. The depth of concrete was taken to be large compared to the depth of the plate from the top and, thus, the base was modelled as restrained in the Z-direction. The rigid plate action was modelled using constant displacement for the nodes representing the plate and it was taken that the plate is not bonded to the concrete. The problem was investigated using 20 node isoparametric brick elements with the aspect ratios shown in Figure 3.2. One quarter of the plate was modelled due to symmetry.

The meshes (shown in Figure 3.2) were developed to investigate the effect of increasing the mesh size away from the critical zone. Details of the meshes are given in Table 3.1. For all the analyses undertaken in this study, the concrete is modelled with an in-situ uniaxial compressive strength of $f_{cp} = 25$ MPa, a tensile strength of $f_t = 1.65$ MPa and an initial modulus of elasticity of $E_c = 25300$ MPa. The values of the tension softening parameter α_1 (as defined by Equation 2.30) were calculated for each model and are given in Table 3.2. The fracture energy was based on the CEB-FIP (1990) model code recommendation and is taken as 85 Nm/m^2 assuming maximum aggregate size of 32 mm for plain concrete.

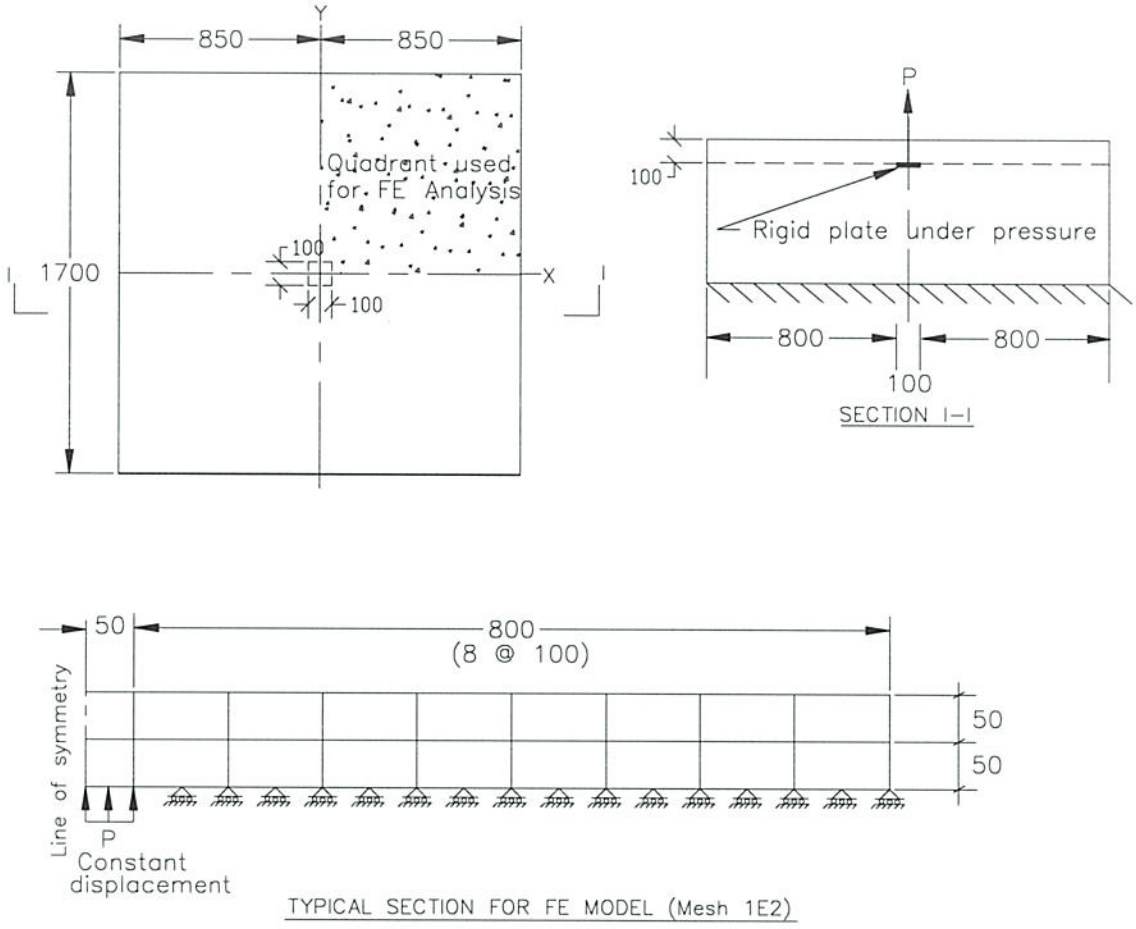

Figure 3.1 - Square concrete mass under concentric load.

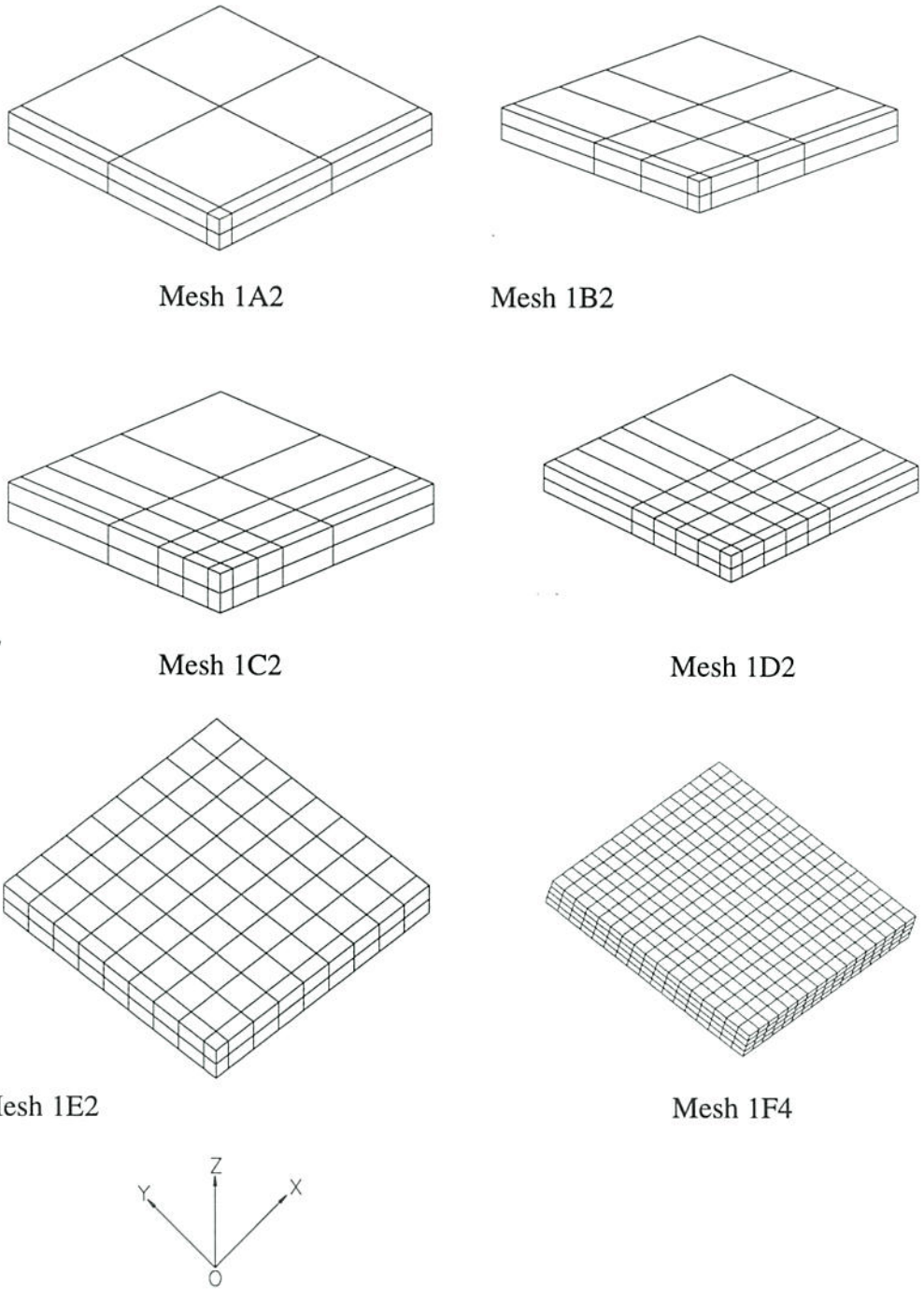

Figure 3.2 - Finite element meshes used to study the effects of aspect ratio.

Table 3.1 - Properties of the different FE models having 2 and 4 elements through the thickness.

Model	No. of Nodes	No. of Elements	Total DOF	Aspect ratios near the critical area*.			
				Maximum		Minimum	
				x/y	Max(x, y)/z	x/y	Min(x, y)/z
1A2	152	18	366	8	8	1	1
1B2	245	32	604	4	4	1	1
1C2	356	50	890	2	2	1	1
1D2	497	72	1260	2	2	1	1
1E2	1040	162	2694	2	2	1	1
1F4	5976	1734	16506	1	2	1	2

Note: * x/y is the aspect ratio of an element in the plan of the slab.
Max(x ,y)/z and Min(x,y)/z are the maximum and the minimum aspect ratios through the thickness respectively.

Table 3.2 – Values of α_1 of ε_u for different models.

Model	1A2	1B2	1C2	1D2	1E2	1F4
$\alpha 1$	10.5	13.3	15.4	15.4	15.4	40.0

The other parameters needed to define the concrete material laws were taken as

$\phi = 30^0$ $\quad \psi = 12.6^0$ $\quad \alpha = 15^0$
$\mu = 0.2$ $\quad \beta = 0.2$ $\quad \varepsilon_0 = 0.002$

where μ is the Poison's ratio and other parameters are as defined in Section 2.

The results of the finite element analyses are presented in Table 3.3 and the load versus deflection curves are shown in Figure 3.3. The responses in the elastic region are similar for all cases, however, with the propagation of cracks the aspect ratio adopted in the critical region significantly influences the results. In models 1C2 and 1D2, with larger meshes in the region away from the critical zone, the pattern of load-deflection curves are

similar to that of the uniformly meshed model 1E2. In all cases the responses of the two layer mesh slabs are seen to be in the same range as predicted by the refined 4 layered mesh 1F4 showing that some of the other meshes are somewhat stiffer than mesh 1F4. The ultimate load for the two layered meshes are close to each other with the difference between the extremes being about 10 percent of the value predicted by mesh 1F4. It is concluded that away from the critical region the mesh has little influence on the failure load and the load versus deflection response. However, there is some effect on the post cracking behaviour with the increase in the number of elements through the thickness. It is to be noted here that the values of α_1 were based on equation 2.30 and a large variation occurs between analyses due to the varying mesh sizes. Taking $\alpha_1 = 20$ for mesh 1F4 reduces the ultimate load from 218 kN to 188 kN and thus the fracture load is sensitive to the value of α_1 adopted.

The computation time required for nonlinear three dimensional analyses is an important factor in the mesh sizing. The CPU times for each of the models is given in Table 3.4. The analyses were performed on a DEC Alpha running UNIX with a single 300 MHz processor and 128 megabytes of RAM. Reviewing the analytical results together with the CPU time, models 1C2, 1D2, and 1E2 are found to be the most efficient. Of these three models, model 1D2 is the cheapest with a minium of sacrifice in the accuracy of the results. This model is chosen for further investigation.

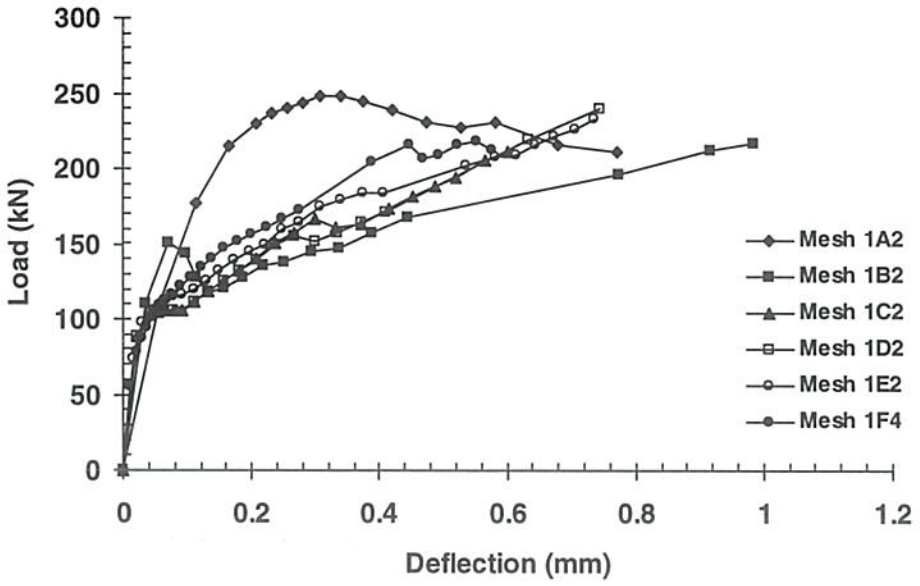

Figure 3.3 - Load – deflection curves for model 1A2 to 1F4 (3 x 3 x 3 Gaussian quadrature)

Table 3.3 - Ultimate load from the numerical analyses for the models with two or four elements along the thickness.

Model	1A2	1B2	1C2	1D2	1E2	1F4
Ultimate load (kN)	249	217	212	240	233	218

Table 3.4 - CPU times for models 1A2 to 1E2 and 1F4 (3 x 3 x 3 Gauss point integration)

Model	Total DOF	CPU time (s) for			
		Linear analysis		Nonlinear analysis	
		Absolute	Relative to 1A2	Absolute	Relative to 1A2
1A2	366	3.3	1.0	225	1.0
1B2	604	4.5	1.4	346	1.5
1C2	890	6.1	1.8	543	2.4
1D2	1260	7.8	2.4	704	3.1
1E2	2694	18.8	5.7	4312	19.1
1F4	16506	548	166	27160	121

Models similar to 1D2 were discretised with 1, 3 and 4 layers through the thickness of the slab. The models are designated as 1D1, 1D3, and 1D4 and are shown in Figure 3.4. Details of meshes 1D1 to 1D4 are given in Table 3.5 and the values of α_l used are presented in Table 3.6.

The ultimate loads obtained for slabs 1D1 to 1D4 are tabulated in Table 3.7. Except for mesh 1D1 the failure loads are in the same range with the maximum difference of less than two percent. A variation of 22 % was obtained between model 1D1 and 1D2. The load versus deflection behaviour is plotted for each case in Figure 3.5 where it is shown that similar results are obtained for meshes 1D2, 1D3, and 1D4. It is concluded, therefore, that two elements through the thickness of the slab are sufficient to obtain accurate results.

Table 3.5 - Properties of FE models with different numbers of elements through the thickness.

Model	Total nodes	Total elements	Total DOF	Aspect ratios near the critical area *			
				Maximum		Minimum	
				x/y	Max(x, y)/z	x/y	Min(x, y)/z
1D1	315	36	754	2	1	1	0.5
1D2	497	72	1260	2	2	1	1
1D3	679	108	1766	2	3	1	1.5
1D4	861	144	2272	2	4	1	2

Note: * x/y is the aspect ratio of an element in the plan of the slab.
Max(x ,y)/z and Min(x,y)/z are the maximum and the minimum aspect ratios through the thickness for the , respectively

Table 3.6 – Values of α_1 of ε_u for different models.

Model	1D1	1D2	1D3	1D4
α_1	12.1	15.4	17.7	19.3

Table 3.7 - Ultimate load from the numerical analyses with different numbers of elements through the thickness.

Model	Ultimate load (kN)
1D1	293
1D2	240
1D3	243
1D4	242

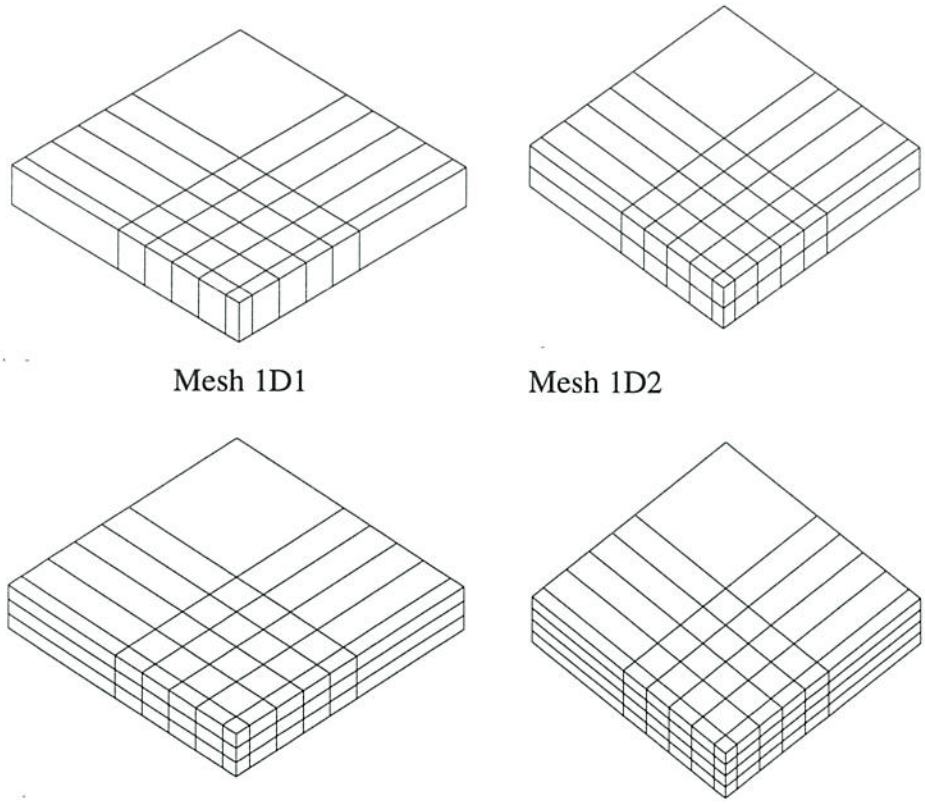

Figure 3.4 – Finite element meshes used to study the effects of different division through the thickness of the slab.

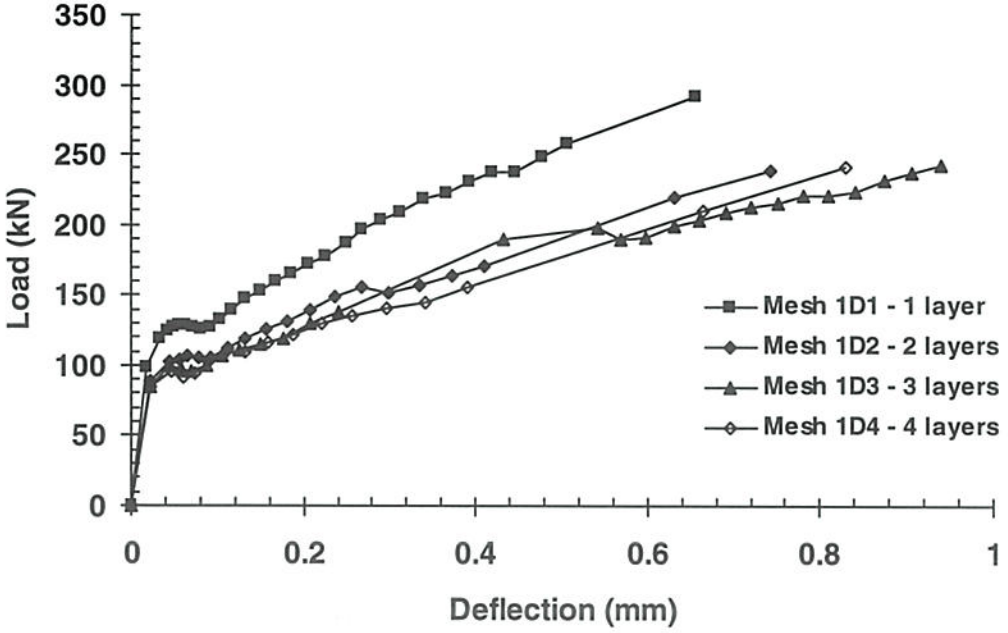

Figure 3.5 – Comparison of the load versus deflection curves for the 1D mesh with one to four layers through the thickness.

To study the influence of the order of integration on the results of finite element analyses models 1D2 and 1E2 were analysed using 2 x 2 x 2 Gaussian quadrature (designated as 1D2-2 and 1E2-2) and 3 x 3 x 3 Gaussian quadrature (designated as 1D2-3 and 1E2-3).

The load versus deflection curves for mesh 1D2-2 and 1E2-2 are compared in Figure 3.6 and Figure 3.7 with the corresponding curves using the 3 x 3 x 3 Gaussian integration (that is meshes 1D2-3 and 1E2-3). The figures show that the order of integration scheme has no significant effect on the numerical results. The ultimate loads for each analysis are given in Table 3.8.

The CPU time for each of the analyses are shown in Table 3.9 and it is seen that reducing the integration order from 3 x 3 x 3 to 2 x 2 x 2 reduced the CPU time by a significant amount. Thus, it is concluded that the reduced 2 x 2 x 2 integration gives adequate accuracy and efficient solution times.

Table 3.8 - Ultimate loads for slabs 1D and 1E with different sampling points.

Model	Ultimate Load (kN)	Gaussian Quadrature
1D2-2	208	2 x 2 x 2
1D2-3	240	3 x 3 x 3
1E2-2	250	2 x 2 x 2
1E2-3	233	3 x 3 x 3

Table 3.9 – Solution time for slabs 1D and 1E for different integration quadrature

		CPU time (seconds)	
Model	Total DOF	Linear analysis	Nonlinear analysis
1D2-2	1260	5.8	215
1D2-3	1260	7.8	704
1E2-2	2694	14.4	724
1E2-3	2694	18.8	4310

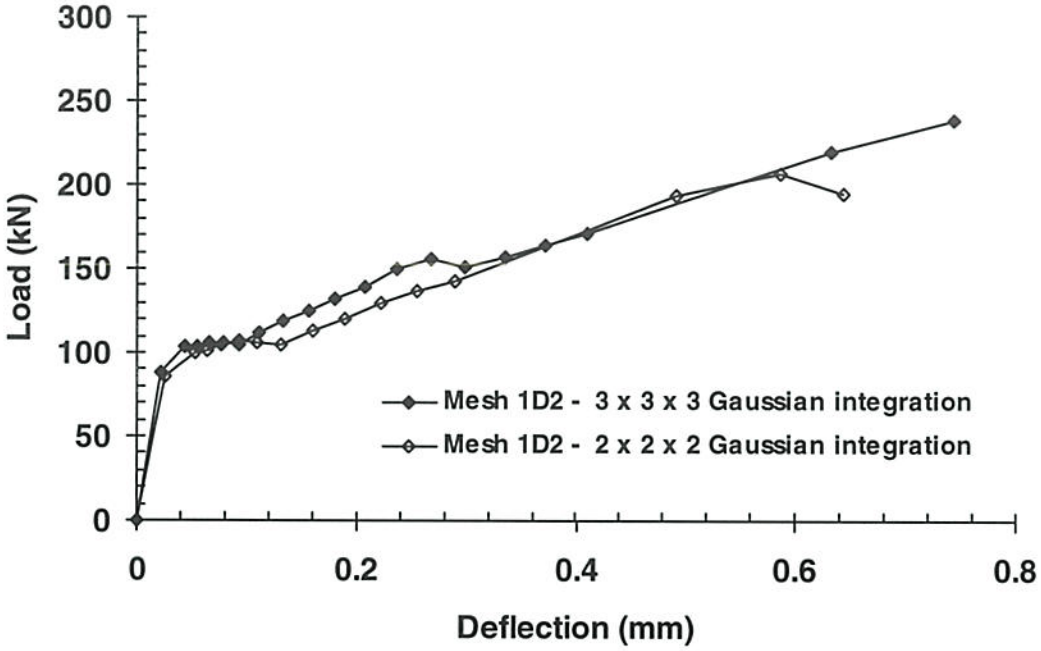

Figure 3.6 - Load versus deflection curves for model 1D2 with different integration schemes.

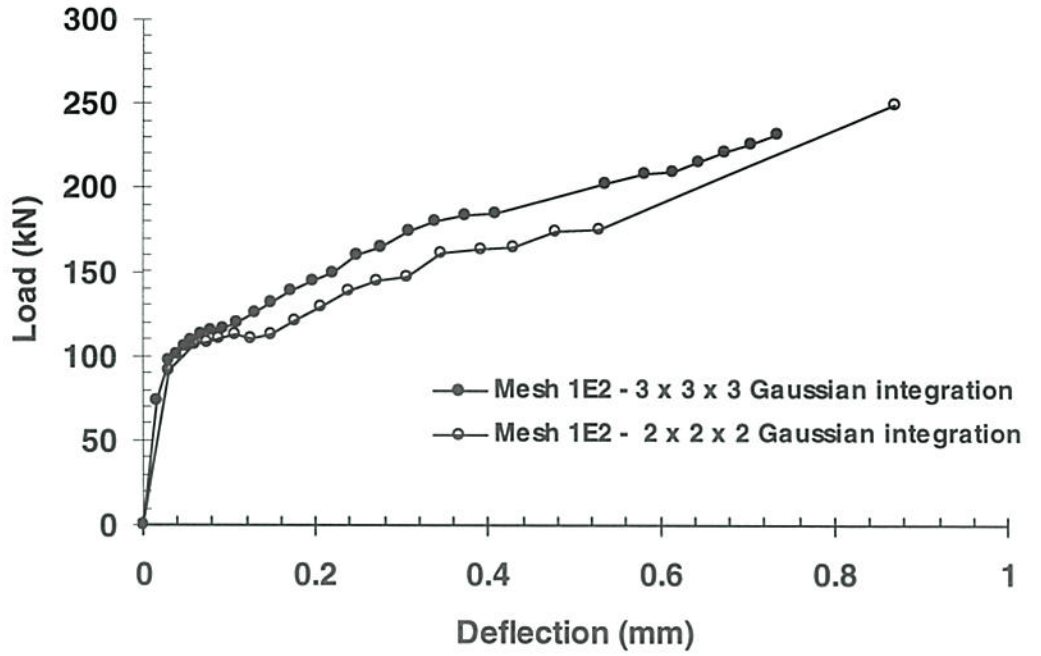

Figure 3.7 - Load versus deflection curves for slab 1E2 with different integration schemes

3.3 Upper bound solution

The model studied in Section 3.2 of this report is similar to that of punching shear in plain concrete. In order to assess the validity of the model the results are compared with the plasticity solution of Nielsen et al. (1978).

Nielsen et al. proposed a plasticity model for the pullout of circular discs in concrete. The failure surface is formed by a solid of revolution, with the remainder of the slab

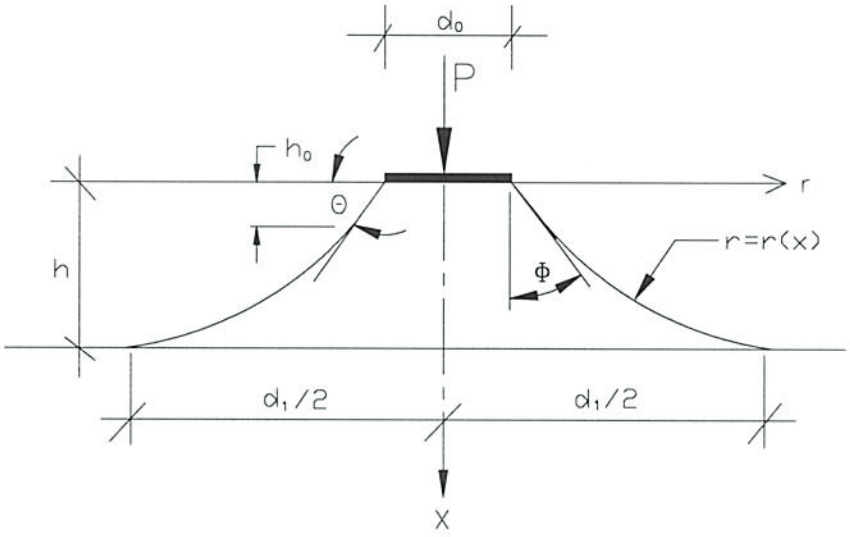

Figure 3.8 – Failure surface (Nielsen et al., 1978).

remaining rigid. The failure surface that gives the lowest failure load P, as shown in Figure 3.8, is given by

$$r = \frac{d_0}{2} + x \tan\phi \qquad \text{for } 0 \le x \le h_0$$

$$r = a \cosh\left(\frac{x - h_0}{c}\right) + b \sinh\left(\frac{x - h_0}{c}\right) \qquad \text{for } h_0 \le x \le h \qquad (3.1)$$

where $c = \sqrt{a^2 - b^2}$, d_0 is the diameter of the rigid plate; ϕ is the angle of internal friction for the concrete; and h_0 is the depth of conical part in the failure surface. The function generated by equation 3.1 consists of a catenary curve, joined by a straight line and is constrained by the boundary conditions

$$a = \frac{d_0}{2} + h_0 \tan\phi$$

$$\frac{b}{c} = \tan\phi \Rightarrow b = \frac{a\tan\phi}{\sqrt{1+\tan^2\phi}} \tag{3.2a}$$

$$\frac{d_1}{2} = a\cosh\frac{h-h_0}{c} + b\sinh\frac{h-h_0}{c} \tag{3.2b}$$

The pullout load, P, is calculated by minimising the function

$$P = \frac{\pi\nu f_{cp}}{2}\left[h_0\left(d_0 + h_0\tan\phi\right)\frac{1-\sin\phi}{\cos\phi} + lc(h-h_0) + l\left(\frac{d_1}{2}\sqrt{\left(\frac{d_1}{2}\right)^2 - c^2} - ab\right) - m\left(\left(\frac{d_1}{2}\right)^2 - a^2\right)\right] \tag{3.3}$$

where ν is the effectiveness factor; f_{cp} is the compressive strength of the in place concrete; d_1 is maximum diameter of the failure surface; and l and m are the material constants and expressed as

$$l = 1 - (k-1)\frac{f_t}{f_{cp}} \tag{3.4a}$$

$$m = 1 - (k+1)\frac{f_t}{f_{cp}} \tag{3.4b}$$

where

$$k = \frac{1+\sin\phi}{1-\sin\varphi} \tag{3.4c}$$

The ratio f_t/f_{cp} is notionally based on the ratio of the tensile strength to the compressive strength of the concrete, but, in reality is a calibration factor used to correlate the dimension d_1 with experimental observations. Nielsen et al. (1978) found that a value $400 \le \sigma_c/\sigma_t \le 1000$ gives the best fit with the experimental data. In equation 3.3 the efficiency factor, ν, is introduced to account for the imperfect assumption that concrete is a perfectly plastic material and to calibrate the model with experimental data. Based on their observations assuming a square root dependence on concrete strength, Nielsen et al. (1978) proposed that

$$v = \frac{4.22}{\sqrt{f_{cp}}} \leq 1.0 \tag{3.5}$$

In verifying the model with experimental data, Nielsen et al. showed a reasonable mean strength correlation but with a coefficient of variation as high as 21%. The coefficient of variation, however, was generally smaller when individual series were considered.

Nielsen et al. (1978) also recommended a simplified relationship to calculate the average shear stress through the depth of the section taking $\theta = 26^\circ$ to the soffit of the slab (refer Figure 3.8). This leads to

$$\tau = \frac{P}{\pi(d_0 + 2h)h} \tag{3.6}$$

If a lower bound to the failure surface is taken at $\theta = 45^\circ$ (as per ACI 318, 1999 and AS 3600, 1994) then the shear stress is given by

$$\tau = \frac{P}{\pi(d_0 + h)h} \tag{3.7}$$

With an angle of internal friction of $\phi = 30^\circ$, taking $d_0 \cong \frac{2}{\sqrt{\pi}} d_c$ where d_c is the depth of a square column (that is taking an equivalent circular area) and with $\tau = 0.33\sqrt{f_{cp}}$, $h = 100$ mm and $d_c = 100$ mm, by equations 3.6 and 3.7 the bounds of the ultimate load are

$$110 \text{ kN} \leq P_u \leq 162 \text{ kN}$$

With the Nielsen et al. refined model given by equations 3.1 to 3.5, and with the bounds of $\frac{f_t}{f_{cp}} = 400$ and 1000, the failure load for the pullout of a 100 mm square plate at the depth of 100 mm into the concrete are

$$184 \text{ kN} \leq P_u \leq 193 \text{ kN}$$

The finite element results (given in Table 3.7) compare favourably with the model proposed by Nielsen et al. (1978) and suggest that taking a 45^0 failure surface (as given by ACI 318 and AS 3600) is overly conservative.

3.4 Conclusions

In this section, mesh grading is shown to have significant influence on the results of the FE analyses. The integration scheme adopted is important in terms of the solution time required for the analysis but has little effect on the overall results.

The FE model predictions are in reasonable agreement with the closed form plasticity model of Nielsen et al. (1978) and in close agreement with the Nielsen et al.'s simplified model with $\theta = 26^{\circ}$. The numerical model also suggests that the ACI 318 and AS 3600 codes are conservative in taking the failure plane at an angle of $\theta = 45^{\circ}$ to the surface of the slab.

The results of the finite element models studied in Sections 3.2 reflect the variability in the results of finite element analyses. Considering all the aspects discussed above, including the results of the plasticity model of Nielsen et al. (1978), it is concluded that the model 1D2-2 is the best compromise for efficiency and accuracy for the study of punching type failures. That is, a fine mesh within the critical region with a maximum plan aspect ratio of two. Two elements through the thickness of the slab is sufficiently accurate and efficient for solving punching problems. Further, the reduced 2 x 2 x 2 Gaussian integration scheme gives similar results to the full integration, that is integration on a 3 x 3 x 3 Gauss quadrature. The reduced integration saves storage and considerably reduces the solution time without significantly sacrificing accuracy. Away from the punching zone the aspect ratio of the mesh may be increased without loosing accuracy.

4 Influence of Flexural Reinforcement on the Punching Strength of Slabs

4.1 Introduction

Dragosavic and van den Beukel (1974) and Park and Gamble (1980) established that the punching shear strength of flat slabs is not sensitive to the reinforcement content. In this section, the influence of the reinforcement content on the punching shear strength predicted by finite element modelling is assessed. The effect of the integration scheme on the results of the finite element models is also considered. For this purpose the behaviour of a concentrically loaded reinforced concrete slab, resting on the central square column, with varying amounts of steel is investigated. The results are compared with the results obtained from the punching predictions of the Nielsen et al. (1978) model and with flexural theory.

4.2 Effect of Negative Moment Reinforcement on the Punching Strength of Slabs

To study the effect of flexure-shear interaction a 150-mm thick slab resting on a square concentric column (shown in Figure 4.1) is considered. The slab is uniformly loaded and is reinforced with 21 bars at 100 mm spacing in each direction. The depth to the centroid of all reinforcements (in both directions) was taken as 40 mm from the top surface.

The slab, shown in Figure 4.1, was modelled using 363 by 20 node isoparametric solid elements using the mesh shown in Figure 4.2. One quarter of the slab is modelled due to symmetry. The reinforcing bars were modelled as embedded line elements within the concrete elements. The CEB-FIP Model Code (1993) states that dowel effects are not significant when only flexure reinforcement is used due to the thin layer of concrete above the steel. The finite element formulation used here does not allow for any dowel shear. The finite element model, Model 2, consisted of 2064 nodes for the concrete with 44 additional nodes used to model the 22 embedded reinforcing bars in the concrete and include the two ½ area bars at the lines of symmetry. The bottom face of the central element was restrained against vertical movement to simulate a stiff column support.

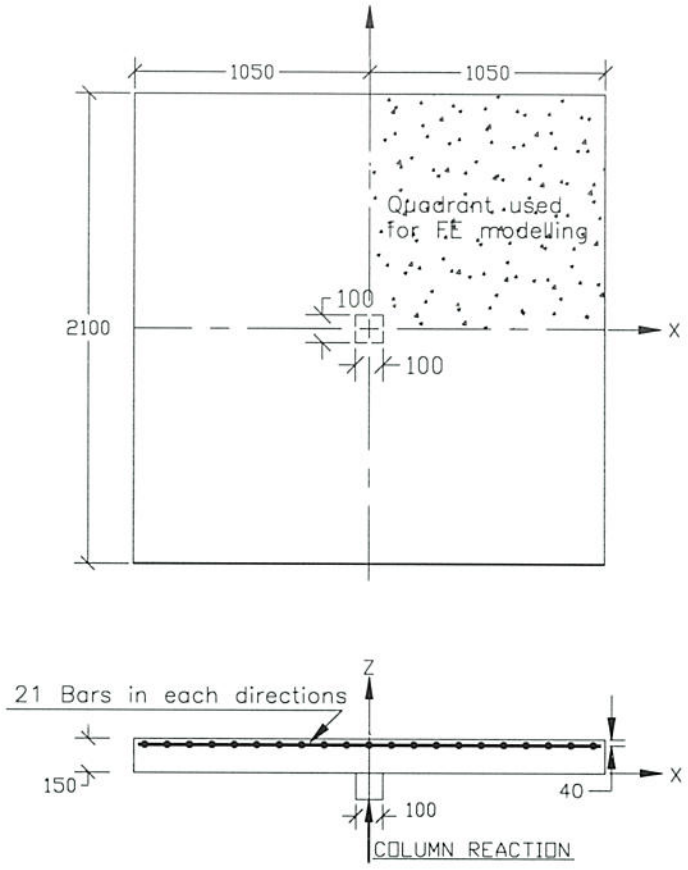

Figure 4.1 - Reinforced slab resting on square column and its cross-section.

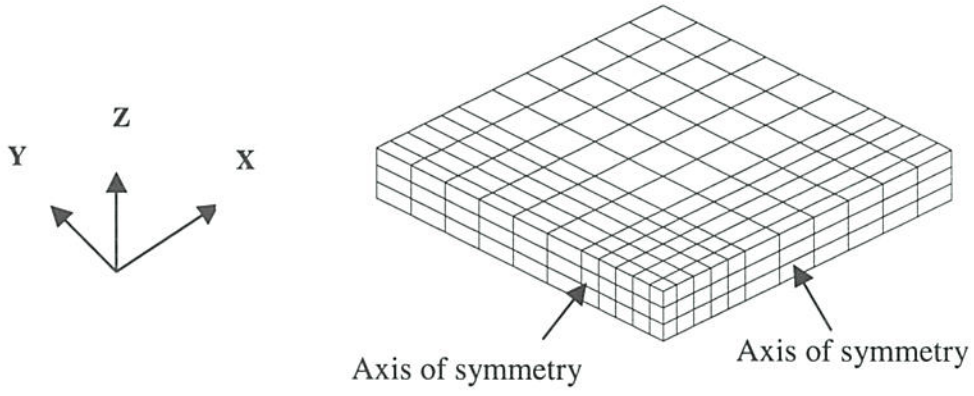

Mesh for Model 2

Figure 4.2 - Mesh for analyses with reinforced slab on column – Model 2.

The material properties used for the concrete were

$f_{cp} = 25$ MPa $\quad f_t = 1.65$ MPa $\quad E_c = 25.3$ GPa.

$\alpha_1 = 15.3 \quad \beta = 0.2 \quad \phi = 30\ 0$

$\psi = 12.6^0 \quad \alpha = 15^0 \quad \mu = 0.2$

$\varepsilon_0 = 0.002$

An elastic plastic stress-strain model was used to model the reinforcing steel with perfect bond assumed between the reinforcing steel and the concrete. The yield strength of the bars was taken as 400 MPa and the elastic modulus as 200 GPa. Analyses were undertaken for reinforcement ratios of ρ = 0.0045, 0.0101, 0.0140, 0.0182, 0.0235, 0.0285 and 0.0318 with the ratio being calculated using the effective depth of 110 mm. The governing yield line pattern is as shown in Figure 4.3. The flexural strength of the slab is found to be

$$P_{flex} = 6.36m \tag{4.1}$$

where m is flexural strength of a unit width and is approximately given by $m = 0.9\rho\ f_{sy}\ d^2$; $\rho = A_{st}/bd$; and f_{sy}, A_{st}, b, and d are the yield stress of the reinforcing bars, the bar area, the width of the panel and the effective depth from the extreme compression fibre to the centroid of tension force, respectively. In determining the punching shear capacity of the slab, the dowel effect was not considered and, hence, the punching shear capacity is not a function of amount of flexural reinforcement.

4.3 Finite Element Results

The ultimate loads determined for different percentages of longitudinal steel are presented in Table 4.1. With the increase in the reinforcement ratio the ultimate load is also increased but at a decreasing rate with the increasing reinforcement content. The load deflection curve for each of the analyses (with numerical integration over 27 Gauss points) is presented in Figure 4.4. In the elastic region the load versus deflection responses of the slab are similar, but significant variation is observed in the post-cracking stage with the post-cracking response being a function of the reinforcement content.

At the punching shear limit as predicted by the Nielsen et al. (1978) model, the slab fails in a non-ductile mode and the volume of reinforcement has only a small influence on the

failure load. The load versus strain in the reinforcement near the column for the different analyses is shown in Figure 4.5. Ductile failures, accompanied by the yielding of reinforcement, are observed for the lower reinforcement contents. The shear capacity of the slab can be obtained using the model of Nielsen et al. (1978), as discussed in Section 3.3 of this report. The flexural capacity is obtained using yield line theory for the critical yield line pattern as shown in Figure 4.3. The failure load for the slab versus reinforcement content is plotted in Figure 4.6 and it is shown to compare favourably with the theoretical model.

Table 4.1 – Ultimate load from the FEM for mesh 2.

Reinforcement Ratio, ρ (%)	Ultimate Load (kN)	Failure Mode
0.45	148	Flexural
1.01	223	Flexure Shear
1.82.	287	Punching shear
2.85	320	Punching shear
3.18	336	Punching shear

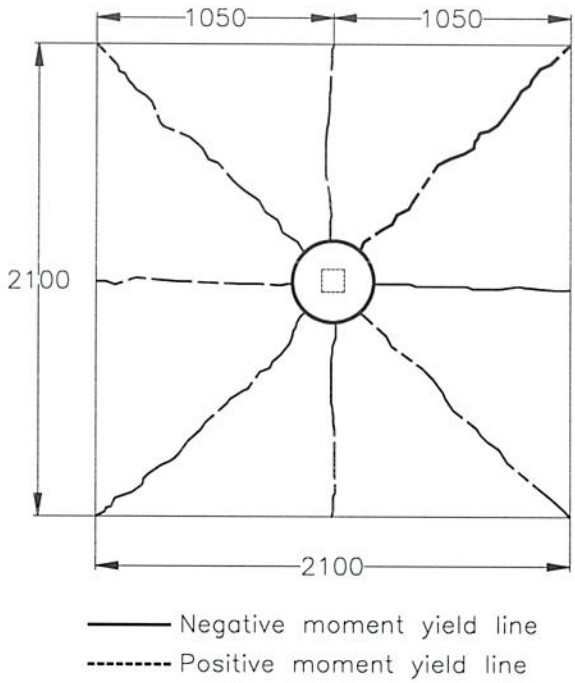

Figure 4.3 - Failure pattern for yield line method.

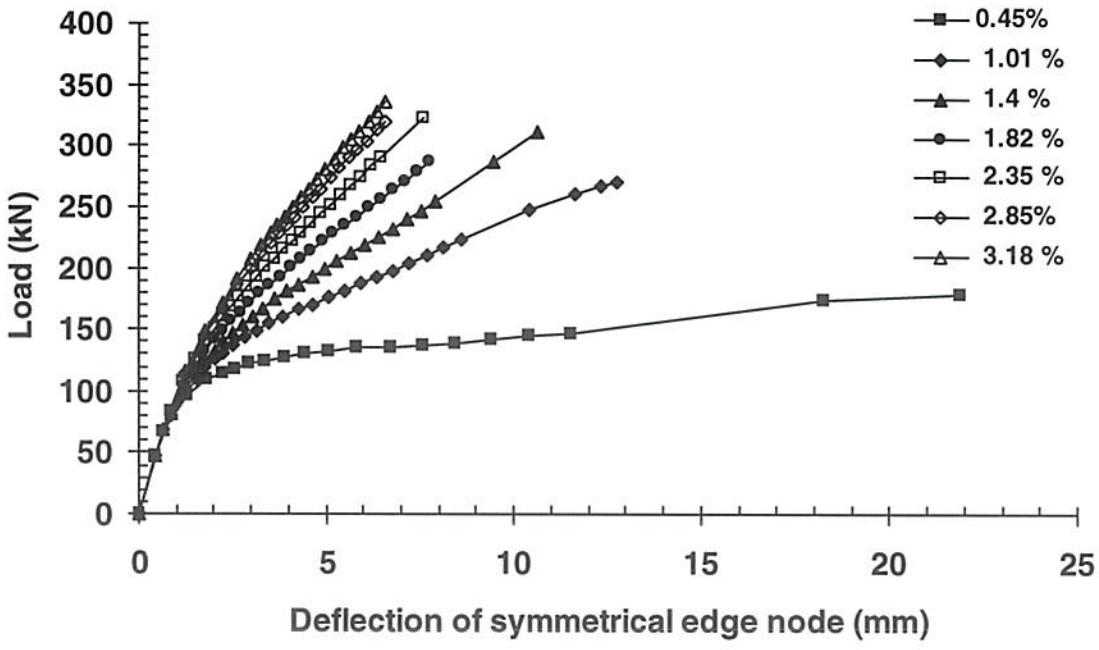

Figure 4.4 - Load – deflection curves for different reinforcement contents.

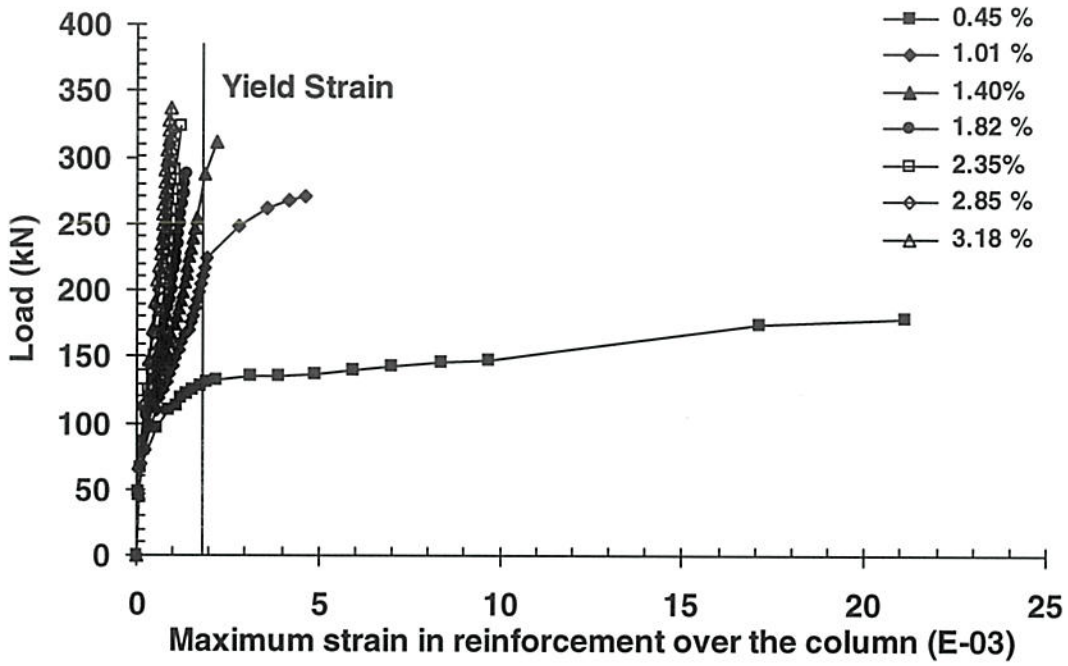

Figure 4.5 - Load – strain developed in steel for various reinforcement contents.

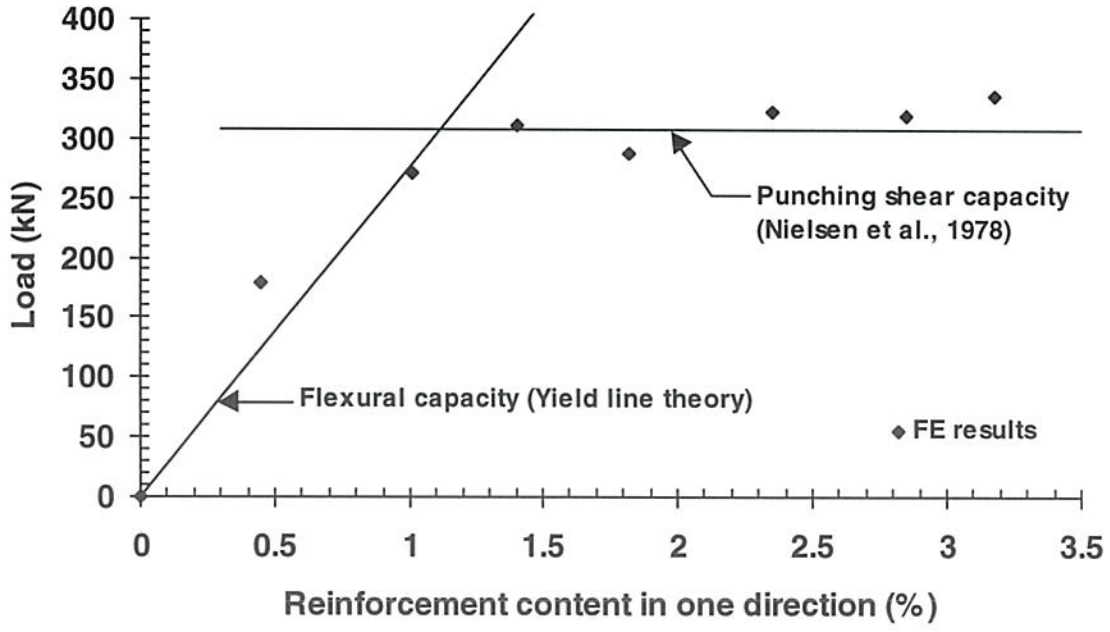

Figure 4.6 - Ultimate load versus reinforcement content.

For the slab with reinforcement ratios of 0.0101, 0.0182 and 0.0318 further analyses were undertaken using integration on a 2 x 2 x 2 Gaussian quadrature. The load versus deflection results and load versus maximum steel strain for these analyses are shown in Figure 4.7 and 4.8, respectively. Ultimate loads are presented in Table 4.2. The figures show that the order of integration has little influence on the results of the finite element analyses. The CPU time required for the analyses is given Table 4.3 and it is seen that the integration on the reduced 8-point integration is 30 percent more time efficient than that for the analyses on the full 27-point quadrature.

Table 4.2 - Ultimate load for the analyses with different Gauss sampling points.

Reinforcement Ratio, ρ (%)	Ultimate load (kN)	Gaussian Quadrature
1.01	221	2 x 2 x 2
	223	3 x 3 x 3
1.82	250	2 x 2 x 2
	287	3 x 3 x 3
3.18	321	2 x 2 x 2
	336	3 x 3 x 3

Table 4.3 - CPU time used for nonlinear analyses with 2 x 2 x 2 and 3 x 3 x 3 Gaussian integration.

Reinforcement Ratio, ρ(%)	CPU time (seconds)	
	2 x 2 x 2 Quadrature	3 x 3 x 3 Quadrature
1.01	3558	4278
1.82	3325	5187
3.18	3910	5648

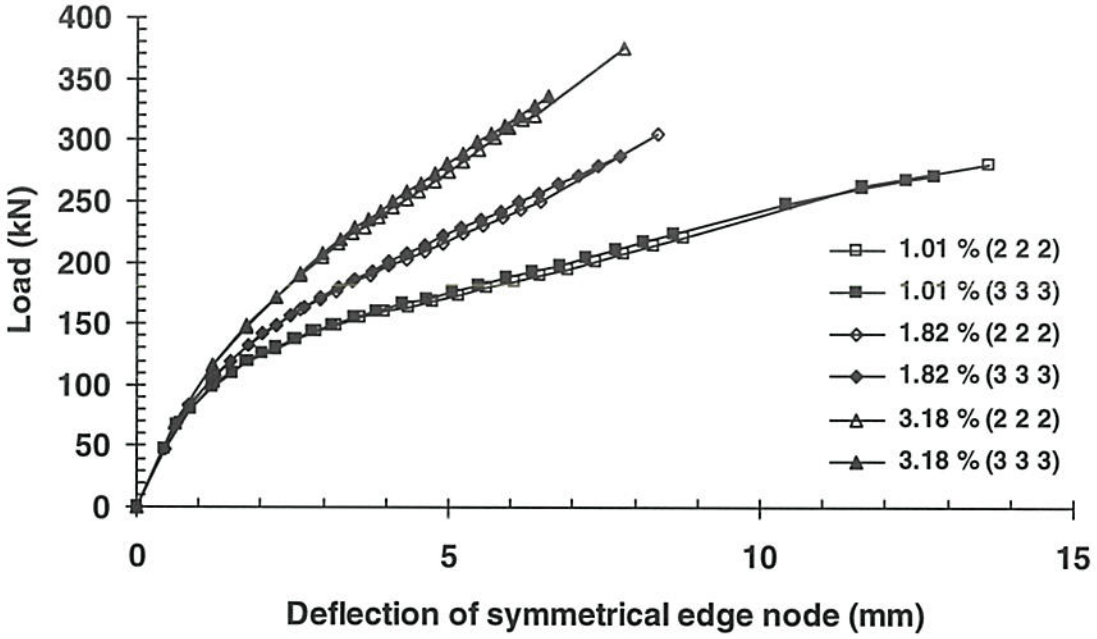

Figure 4.7 – Load deflections curves found from 3 X 3X 3 and 2 x 2 x 2 Gaussian integration rule.

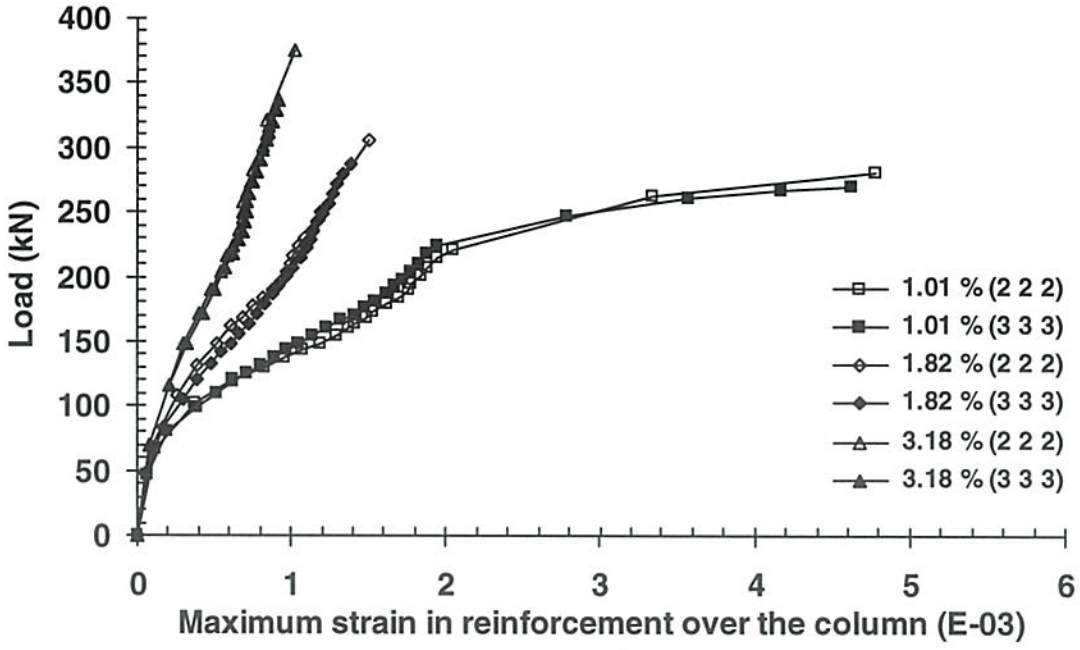

Figure 4.8 – Load versus steel strain curves found using 3 x 3 x 3 and 2 x 2 x 2 integration rules.

4.4 Conclusions

Two modes of failure are clearly seen from the model, that of flexure and that of shear. Once the punching limit is reached increasing the quantity of steel leads to only a small increase in the capacity of the slab. This observation is made, however, in the absence of any dowel effects.

The results of the finite element modelling for a reinforced concrete flat slab in punching shear show that using a reduced 8 point integration scheme gives a good solution without sacrificing accuracy. Thus, as for the plain concrete slab analysed in Section 3.3 of this report the use of a reduced integration scheme is appropriate in the numerical modelling of flat slabs.

The results of the finite element model are consistent with the observation of Dragosavic and van den Beukel (1974) in that the negative moment reinforcement does not significantly influence the punching shear strength. The finite element results are also consistent with the theoretical model for strength. It is concluded, therefore, that the finite element formulation is capable of predicting punching failure in reinforced concrete slabs.

5 Sensitivity Analyses of FE modelling Parameters

5.1 Introduction

The behaviour of cracked reinforced concrete structures is complex. While micro and fracture models are becoming more widely available to study the mechanics of concrete cracking, they require intensive computing resources. At present, these models have limited applications to large-scale concrete structures. Other less numerically demanding, smeared and discrete crack models are available. The 3D element in DIANA is such a model, but it requires the calibration of a number of parameters. The element response is modelled by using factors for tension stiffening, compression softening and shear retention. In this study, a linear tension-softening model was used, as discussed in Section 2.4. The tension softening model depends on three factors, the tensile strength of the concrete f_t, the initial elastic modulus, E_c, and ultimate cracking strain of the concrete for zero stress, ε_u. Of these parameters ε_u is selected using van Mier's (1987) equation (equation 2.30). In the analyses performed in this study a shear retaining factor of $\beta = 0.2$ was used unless stated otherwise.

5.2 Sensitivity to the Concrete Tensile Strain at Zero Stress, ε_u.

With the development of cracks, the stiffness of the concrete reduces with the rate of stiffness degradation given by the slope of the tension softening curve. In reinforced concrete structures an increase in the slope of concrete constitutive model over that of concrete in uniaxial tension is needed to account for the tension stiffening effects.

In this study the concrete tension strain at zero stress is taken as

$$\varepsilon_u = \alpha_1 . \varepsilon_{cr} \tag{5.1}$$

where ε_{cr} is the cracking strain and is taken as $\varepsilon = {f_t'}/{E_c}$. The uniaxial tension strength is taken as $f_t' = 0.33\sqrt{f_{cp}}$ where f_{cp} is the in-situ concrete strength (ACI-318, 1999).

To study the sensitivity of the finite element modelling to ε_u the reinforced concrete plate modelled in Section 4.2 with $\rho = 2.85$ percent was analysed for different values of α_1. All other parameters were unchanged and the shear retention factor was taken as $\beta = 0.2$.

The results of the analyses are shown in Figure 5.1.and Figure 5.2, where the load versus deflections and load versus maximum steel strain, respectively, are shown. The parameter α_1 is found to have significant effect in the deflection response of the slab and on the failure load. The development of steel strains are also affected by the selected values for α_1 in the range from cracking of concrete to the point where the tension stress in the concrete is zero. The load versus strain curve converge to a common line once the tension stiffness of the concrete is zero.

5.3 Sensitivity of the Finite Element Model to the Shear Retention parameter, β.

With the development of cracks, the shear stiffness of the concrete is reduced but not to zero due to the effects of dowel shear and aggregate interlock. The shear retention factor β is used to calibrate the shear capacity for cracked concrete, however, its exact calibration is a function of the aggregate type, the concrete strength, crack widths and spacing and the amount of reinforcement crossing the cracks. As such, a realistic mathematical model for this factor is yet to be determined.

Although the importance of this factor is recognised in the nonlinear finite element simulation of the concrete structures, no consensus is found amongst researchers on a mathematical model. Some studies have taken a constant value, while others use a variable factor based on the tension strain. In studies by van Mier (1987), Channakeshava and Iyengar (1988), Barzegar (1989) constant values for β were used varying between $\beta = 0.1$ and $\beta = 0.5$. Other studies such as those by Al-Manaseer and Phillips (1987), and Foster (1992) used a variable shear retention factor model. In this section the sensitivity of the finite element results is examined for different values of β. The other parameters were kept constant.

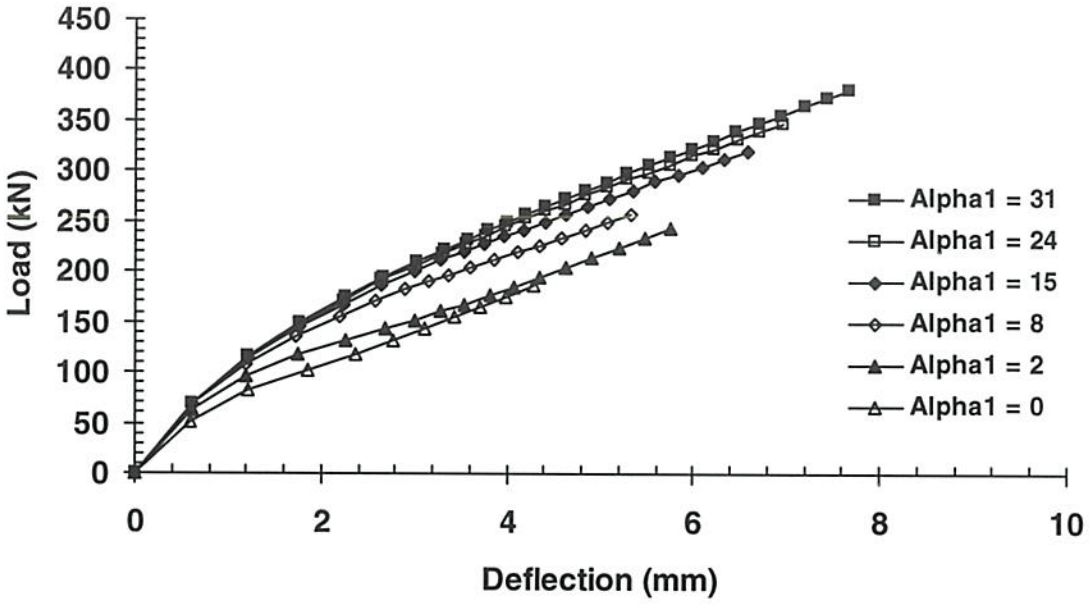

Figure 5.1 – Load versus deflection curves for model 2 with ρ = 2.85 % for different values of α_1.

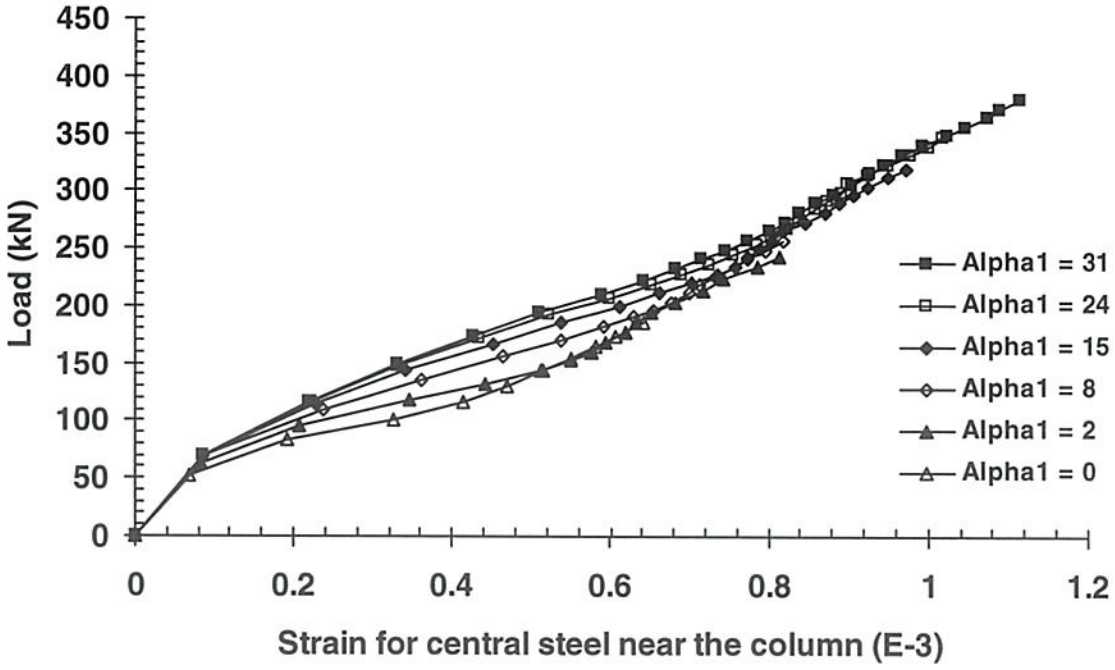

Figure 5.2 – Load versus strain in steel near the midspan for model 2 with $\rho = 2.85$ % for different values of α_1.

The reinforced plate subjected to punching shear shown in Figures 4.1 and 4.2 were used for the study with a reinforcement content of ρ = 2.85 percent. The results of the analyses for load versus deflection and load versus maximum strain in the reinforcement are plotted in Figure 5.3 and Figure 5.4, respectively. The results of the analyses show that the trend of the load deflection response is not affected by β, however, the ultimate load is influenced by the value of β selected. The observations from the load versus strain response in the reinforcement, shown in Figure 5.4, are similar to those for the load versus deflection response. Thus the value of β adopted, while not influencing the overall stiffness behaviour of the slab, has significant effect on the failure load.

5.4 Sensitivity of the Finite Element Model to Friction Angle, ϕ.

An angle of internal friction of 30 to 35 degrees (Vermeer and de Borst, 1984) is commonly used for the concrete. However values as high as 37 degrees (Nielsen et al., 1978) have been adopted. In this section sensitivity analyses are undertaken to determine the influence of ϕ on the finite element results. Values of ϕ = 25, 30 and 35 degrees were used for the parametric study.

As for the previous sensitivity studies the reinforced concrete plate shown in Figures 4.1 and 4.2 with ρ = 2.85 percent were used for the analyses. The other parameters were taken as

$\alpha_1 = 15.3$	$\beta = 0.2$	$\psi = 12.6^0$
$\alpha = 15^0$	$\mu = 0.2$	$\varepsilon_0 = 0.002$

The results of the analyses for load versus deflection and load versus strain in the reinforcement are presented in Figure 5.5 and Figure 5.6, respectively. The analyses show that for the range of ϕ examined the general response of the slab is unaffected. There is a small influence, however, on the failure load.

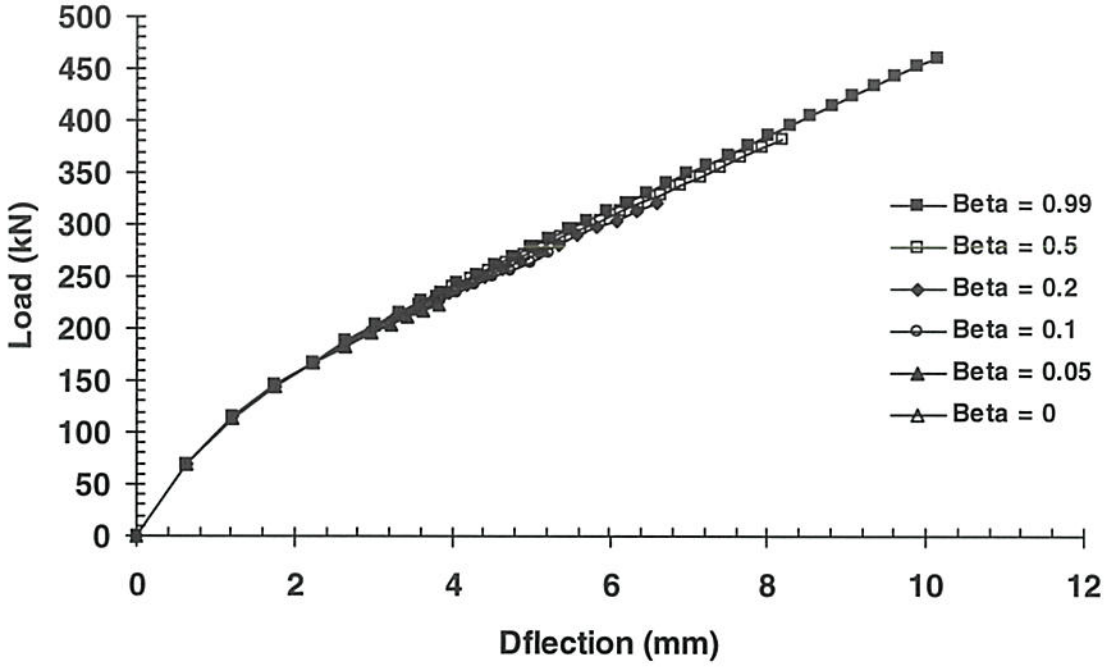

Figure 5.3 – Load versus deflection curves for model 2 with $\rho = 2.85$ % for different values of β.

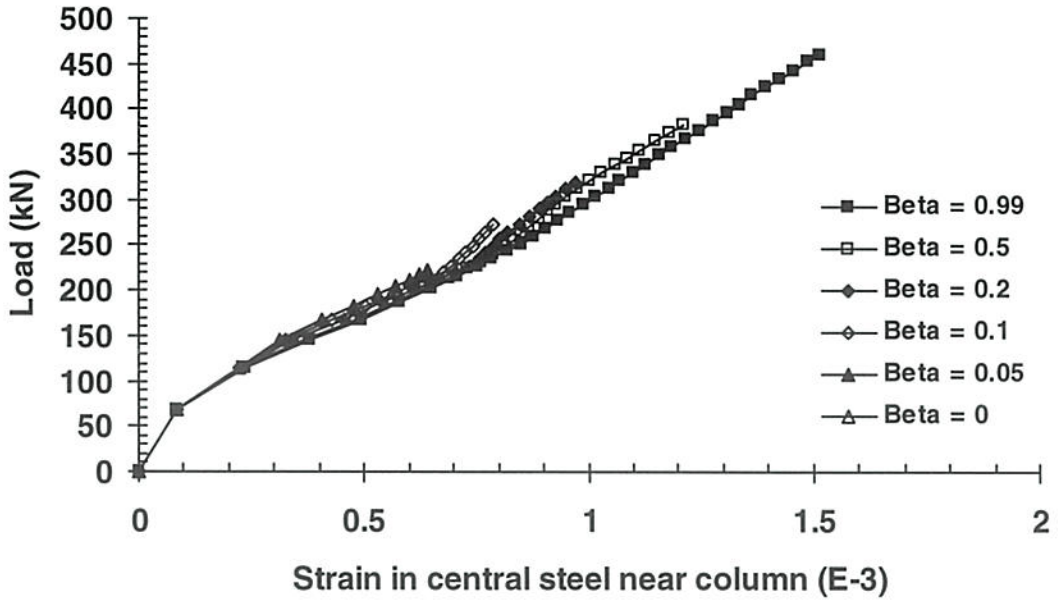

Figure 5.4 – Load versus strain in the steel near the midspan for model 2 with $\rho = 2.85$ % for different values of β.

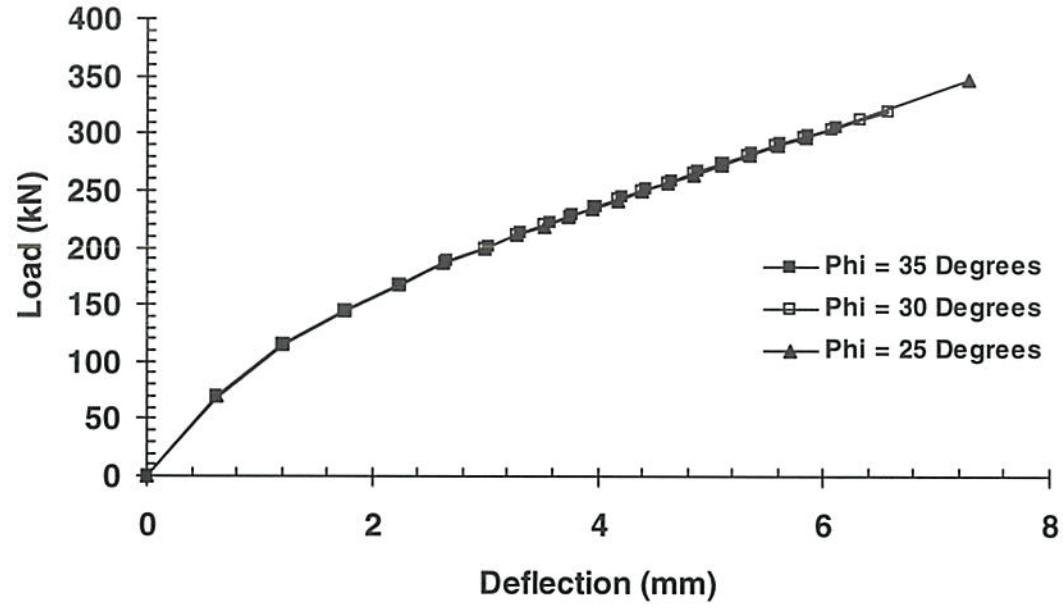

Figure 5.5 – Load versus deflection curves for model 2 with $\rho = 2.85$ % for different values of ϕ.

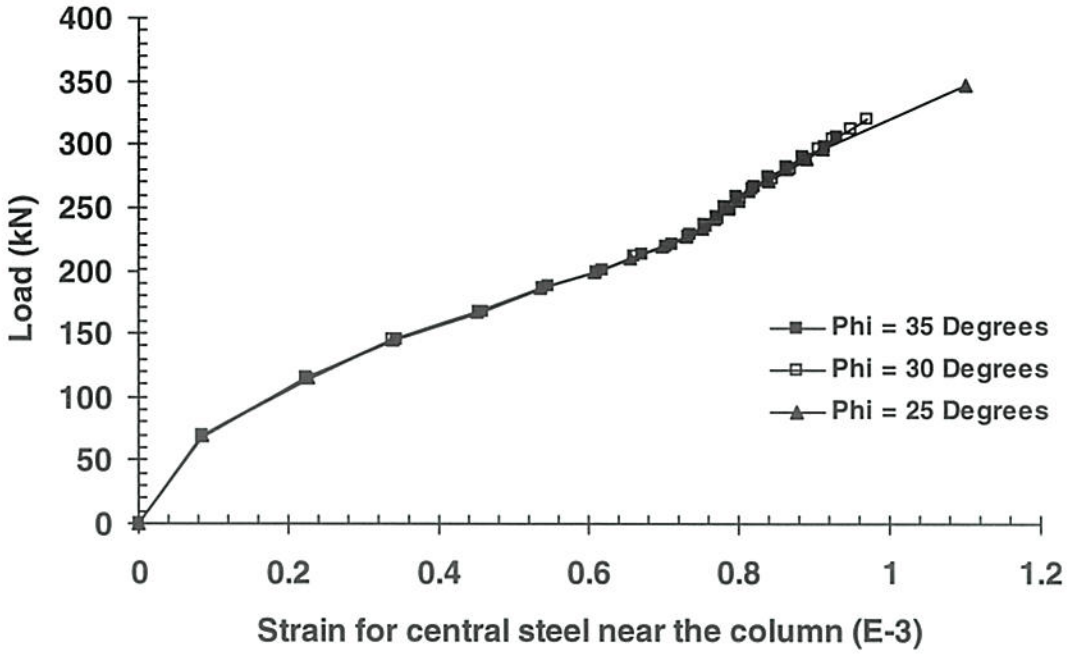

Figure 5.6 – Load versus strain in steel near the midspan for model 2 with $\rho = 2.85$ % for different values of ϕ.

5.5 Sensitivity of the Finite Element Model to the Dilatancy Angle, ψ.

In the non-associated plasticity model the dilatancy angle ψ is always less than the friction angle ϕ and reduces to zero for concrete subject to high confining pressure. Vermeer and de Borst (1984) adopted a value of $0^\circ \leq \phi \leq 20^\circ$. A value of 12.6^0 was used in this study as recommended by Vermeer and de Borst. For the sensitivity test the analyses was carried out for values of $\psi = 7^0$, 12.6^0 and 18^0. The other parameters were fixed at

$\alpha_1 = 15.3$ $\beta = 0.2$ $\phi = 30.^0$

$\alpha = 15^0$ $\mu = 0.2$ $\varepsilon_0 = 0.002$

The reinforced concrete plate given in Figures 4.1 and 4.2 was again used for the analyses with ρ = 2.85 percent. The results of the analyses for load versus deflection and load versus strain in the reinforcement are presented in Figure 5.7 and Figure 5.8 respectively.

The analytical results show that the trend of load deflection and the load versus strain response in the reinforcement plot are not affected by ψ, however, the ultimate loads are influenced to some extent, for ψ less than 12.6^0. Thus the value of ψ adopted, while not influencing the pattern of general response of the slab, has some marginal effect on the failure load.

5.6 Sensitivity of the Model to Compression Softening Slope, E_{cf}.

The slope of the softening brance of the concrete stress-strain curve, E_{cf}, is given by $E_{cf} = \frac{E_c}{\zeta}$. In Hognestad (1951) model $E_{cf} = -\frac{f_{cm}}{0.012}$ and for f_{cm} = 25 MPa this gives E_{cf} = -2083 MPa and ζ = -12.

The sensitivity test of the compression softening slope E_{cf} in the results of the nonlinear finite element analyses was conducted using Model 2 with a reinforcement content of 2.85 percent . The other parameters were set at

$\alpha_1 = 15.3$ $\beta = 0.2$ $\phi = 30.^0$

$\alpha = 15^0$ $\mu = 0.2$ $\varepsilon_0 = 0.002$

$\psi = 12.6^0$

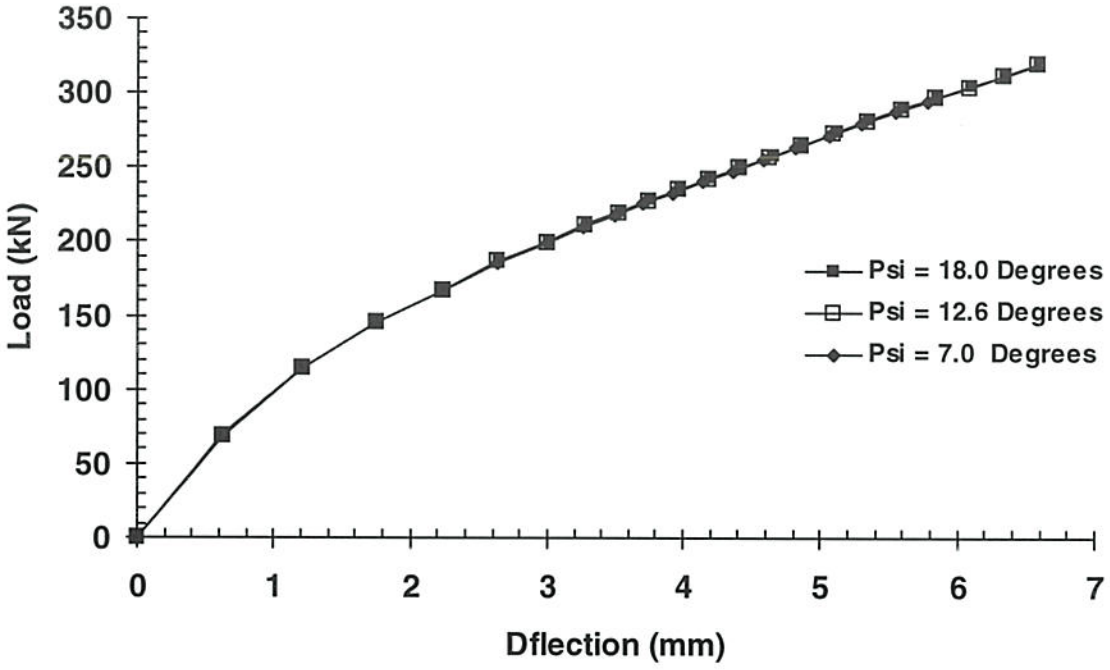

Figure 5.7 – Load versus deflection curves for model 2 with $\rho = 2.85$ % for different values of ψ.

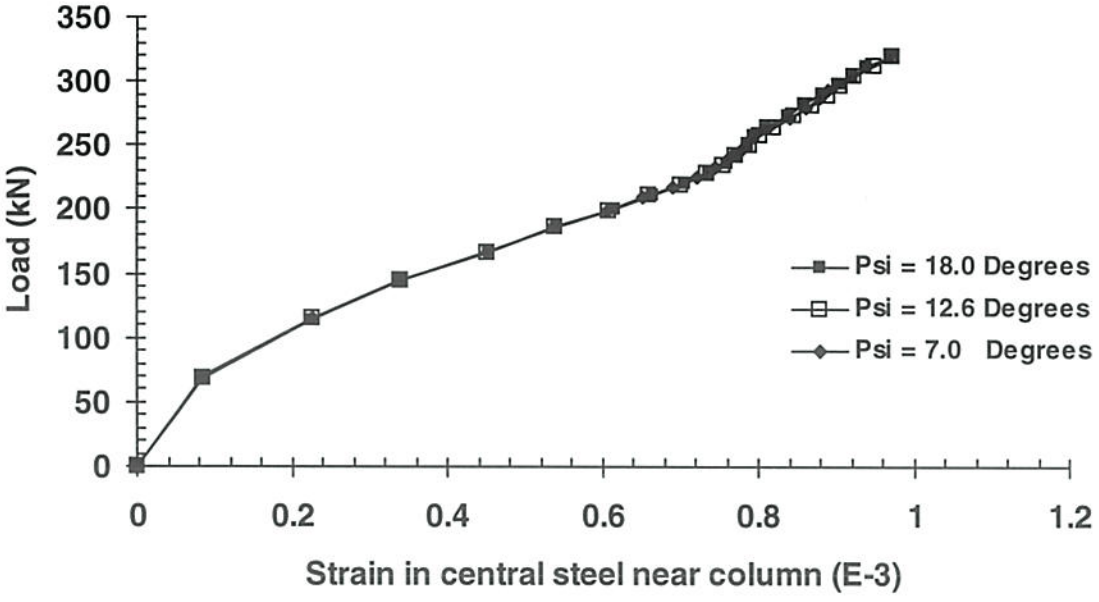

Figure 5.8 – Load versus strain in steel near the midspan for model 2 with $\rho = 2.85$ % for different values of ψ.

The study was undertaken for ζ = -24, -12, and -6. The results of the analyses for load versus deflection and load versus strain in the reinforcement are presented in Figure 5.9 and Figure 5.10 respectively. No effect is observed in the results for varying E_{cf}.

5.7 Conclusions

The sensitivity tests of the different parameters give important insights to understanding the finite element results. The shear retention factor β and the descending slope of the tension stress-strain law (as given by α_1) were observed to have a significant influence on the results of the finite element analyses. The other parameters have only minor effect on the results. The commonly used values may be adopted for all these parameters in the finite element modelling of punching shear type problems. The value of $\beta = 0.2$ for the shear retention factor is found to be suitable. The value of α_1 must be carefully chosen to represent the tension stiffening effect, which is a complex phenomenon involving the interaction between concrete and bonded reinforcing steel.

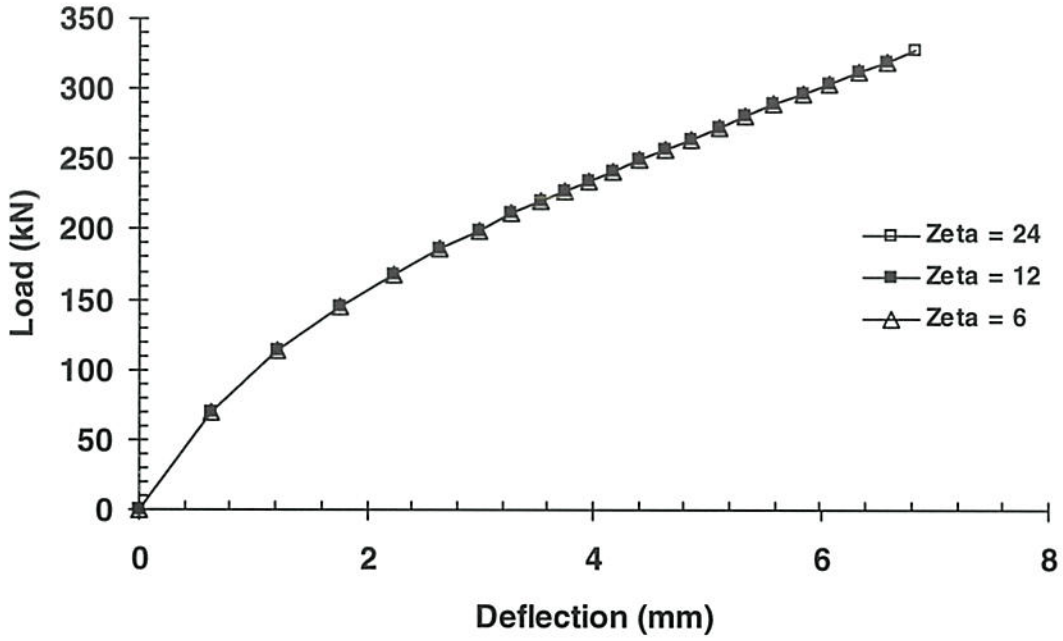

Figure 5.9 – Load versus deflection curves for model 2 with $\rho = 2.85$ % for different values of ζ.

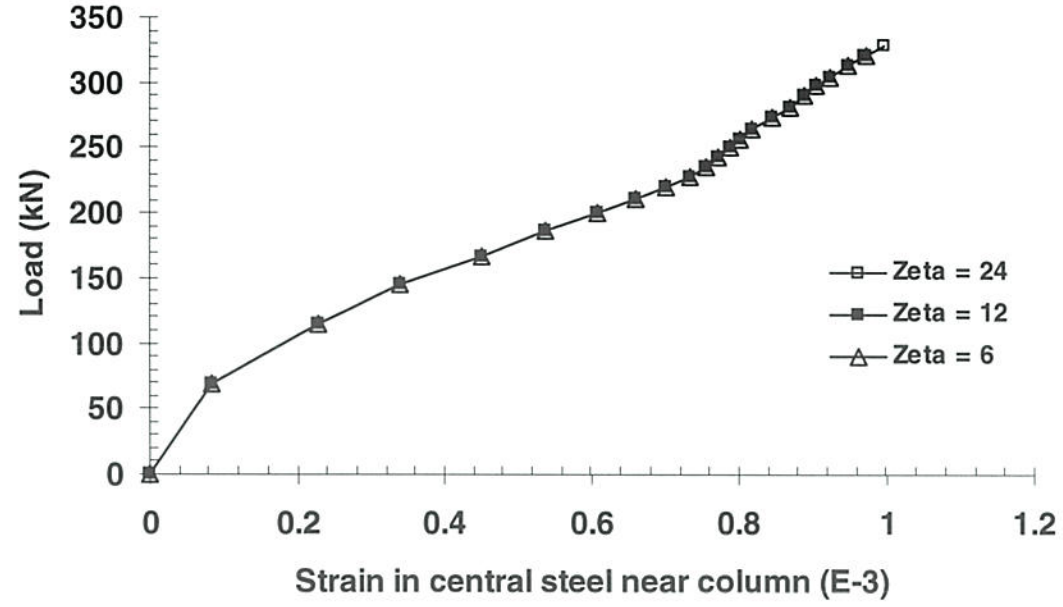

Figure 5.10 – Load versus strain in steel near the midspan for model 2 with $\rho = 2.85$ % for different values of ζ.

6 Verification of the Finite Element Model

6.1 Introduction

To verify the generality of the finite element model, described in Sections 2 to 5 and implemented in the finite element program DIANA (1997), a number of experimental studies have been numerically simulated. The problems selected comprised of a beam failing in flexure, shear and torsion to more complex systems like slab-column connections. The specimens selected were based on the level of details provided in the experimental study reports. The aim was to test the model against a range of applications failing in shear and torsion modes including slab-column connections failing in punching shear.

6.2 Reinforced Concrete Beam of Mansur and Rangan (1978)

Mansur and Rangan (1978) tested a series of floor beams framing into spandrel beams. The beams were subjected to combined flexure, shear, and torsion. Beam SB-2 is selected for the analyses. The specimen consisted of a floor beam spanning 3.0 metres and attached to the midspan of the spandrel beam of 1.5 metres span. Both the floor beam and the spandrel beam had a depth of 300 mm and a width of 180 mm. Details of the specimen and the loading arrangements are shown in Figure 6.1 and the details of the steel reinforcement arrangements are shown in Figure 6.2. The properties of reinforcing steel are given in Table 6.1.

The finite element mesh used for the analysis is shown in Figure 6.3 with one half of the specimen modelled on one side of the line of symmetry. The model consisted of 992 nodes and 148 elements to model the concrete with an additional 401 nodes for the reinforcing steel modelled as embedded bar elements.

The ends of the spandrel beam were fully retrained against vertical translation and twist. The material properties used for the concrete elements were

$f_{cm} = 44.8$ MPa	$f_t = 4.0$ MPa	$E_c = 29.0$ GPa
$\alpha_1 = 13.1$	$\beta = 0.2$	$\phi = 30^0$
$\psi = 12.6^0$	$\alpha = 15^0$	$\mu = 0.2$
$\varepsilon_0 = 0.002$		

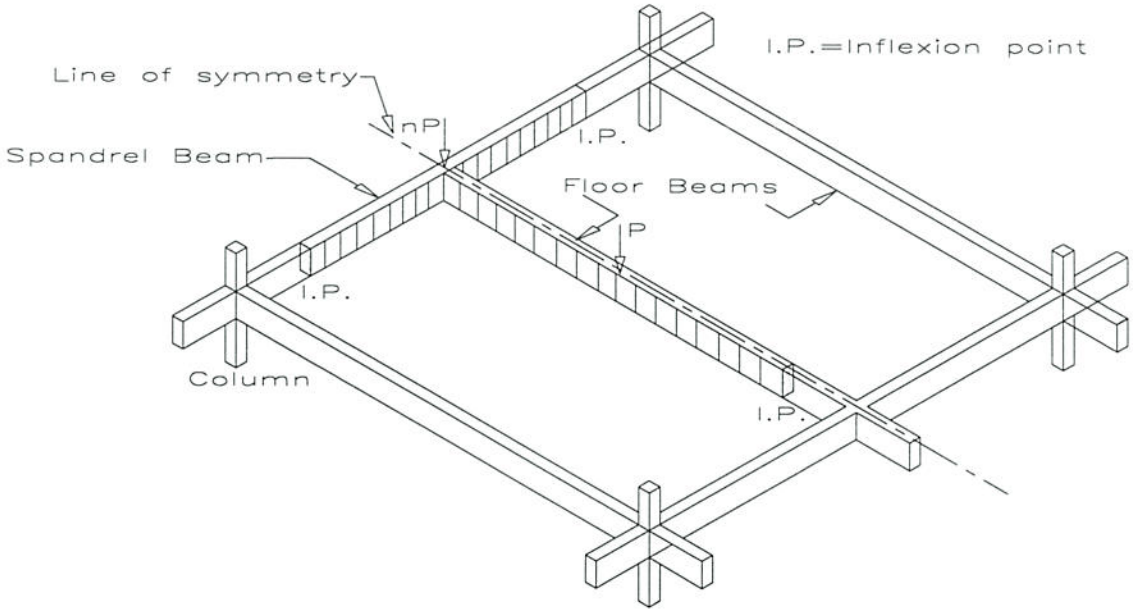

(a)

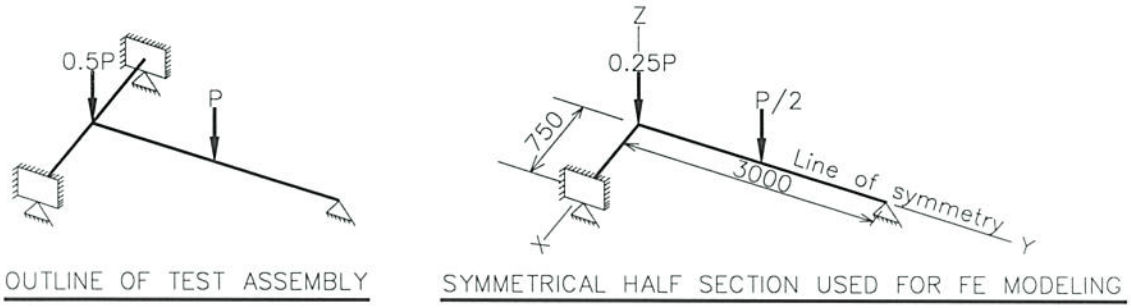

(b)

Figure 6.1 - (a) Idealisation of the spandrel and floor beam system within the frame; (b) outline of test assembly and symmetrical half portion used for FE modelling.

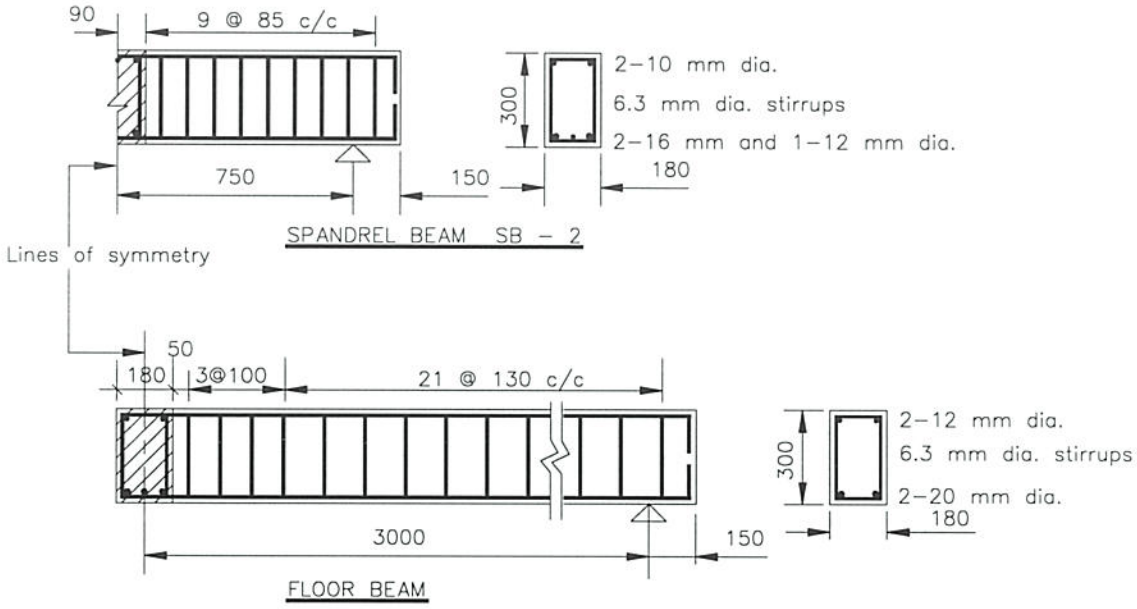

Figure 6.2 – Specimen detail of the T-beam (Mansur and Rangan, 1978).

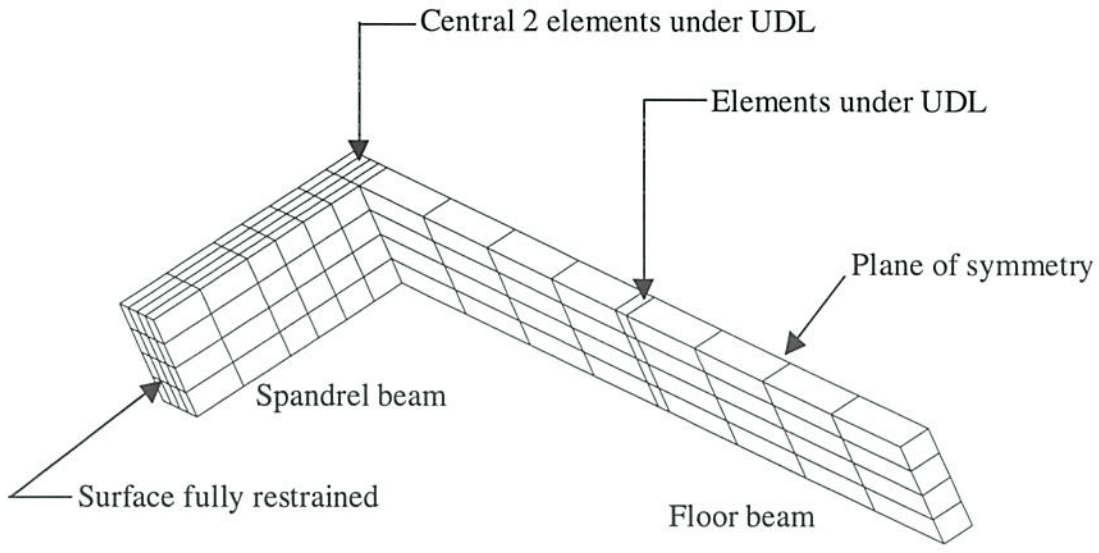

Figure 6.3 – Finite element model of specimen SB-2 (Mansur and Rangan, 1978).

Table 6.1 – Material properties of reinforcing bars (Mansur and Rangan, 1978).

Material Property	Nominal Bar Diameter				
	6.3 mm	10 mm	12 mm	16 mm	20 mm
Actual Bar diameter (mm)	6.60	10.2	11.7	15.3	20.8
Yield strength (MPa)	540	289	488	502	510
Ultimate strength (MPa)	506	442	597	605	608
Young's modulus (GPa)	202	202	201	202	200

In Figure 6.4 to Figure 6.7 and Figure 6.9 to Figure 6.11 the results of the finite element analyses are compared with the experimental results for deflections, twists, torque and reinforcement strains. The load versus deflection curves of the analytical results generally compare well with the experimental results (Figure 6.4) but give a slightly stiffer response than that of the experiment.

The load versus average angle of twist in the spandrel beam, shown in Figure 6.5, and the torque developed in the spandrel beam, shown in Figure 6.6, both compare well with the experimental data. In Figure 6.7 the torque versus the angle of twist at the centre of spandrel beam are compared for the finite element and the experimental data. While the cracking torque was slightly higher for the numerical model, the general trend is in reasonable agreement.

Strains in the top and the bottom reinforcing bars in the floor beam were monitored at the locations shown in Figure 6.8. The results of the load versus strain are shown in Figure 6.9 and a good correlation is observed between the finite element and experimental data. Strains near the middle of the bottom longitudinal bars and in the stirrups near the mid-span of the spandrel beam were measured at the locations shown in Figure 6.8. The finite element results are compared with the experimental data in Figure 6.10 and Figure 6.11 for the longitudinal bars and the stirrups, respectively. The finite element results for the longitudinal bars compare well with the experimental data. The results for the stirrups show a reasonable overall trend but are significantly different before cracking of the section.

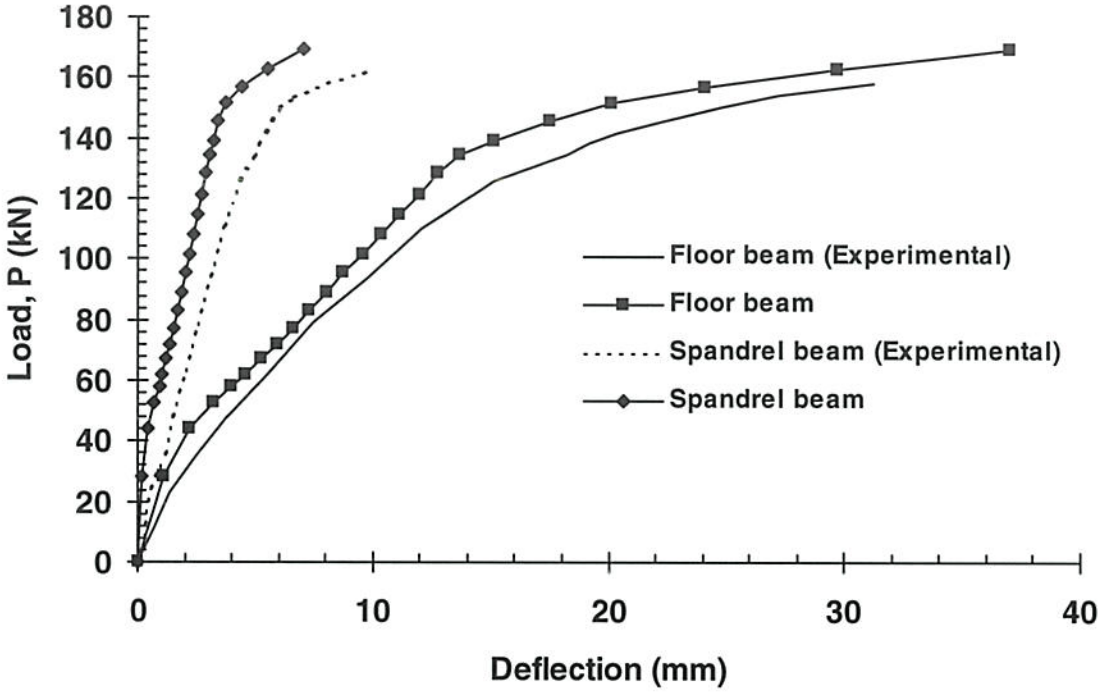

Figure 6.4 - Load versus deflection curves of floor and spandrel beams.

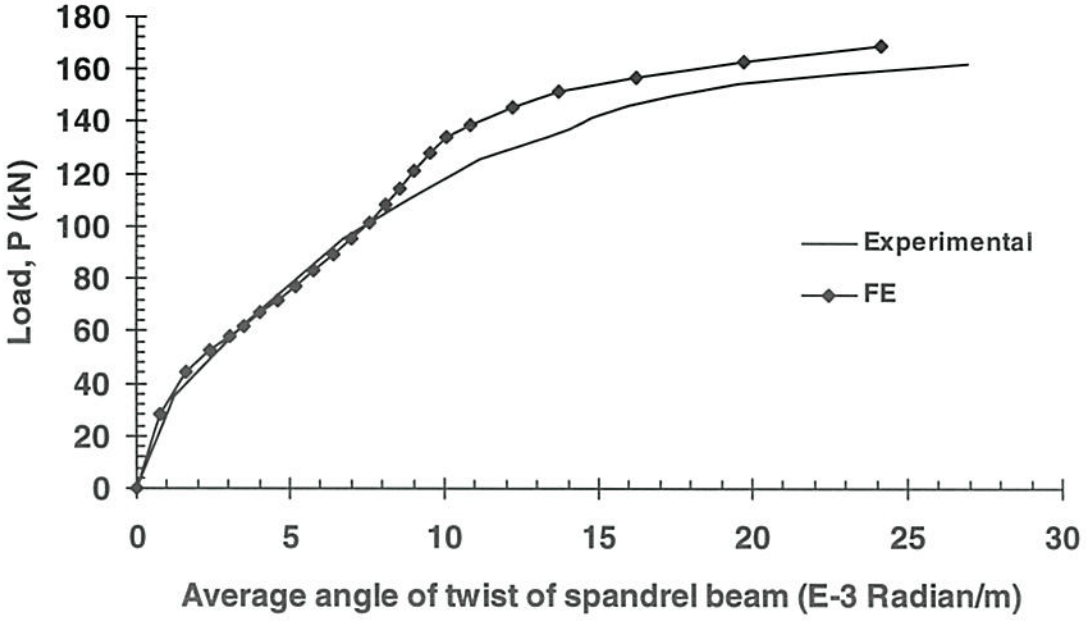

Figure 6.5 – Load versus Twist curves.

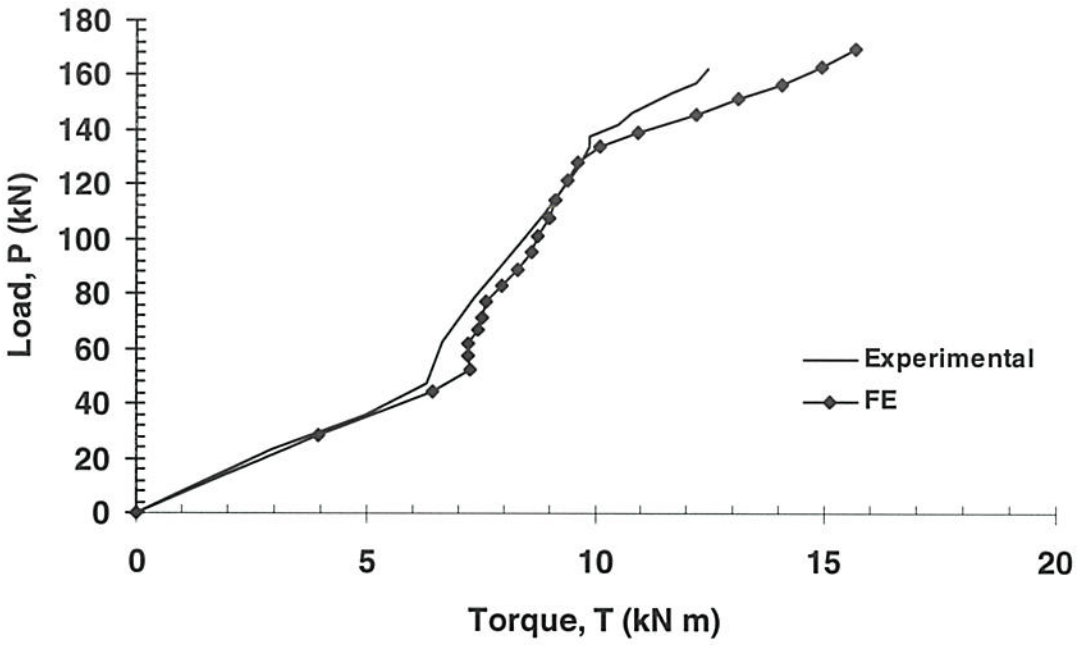

Figure 6.6 – Load versus torque curves.

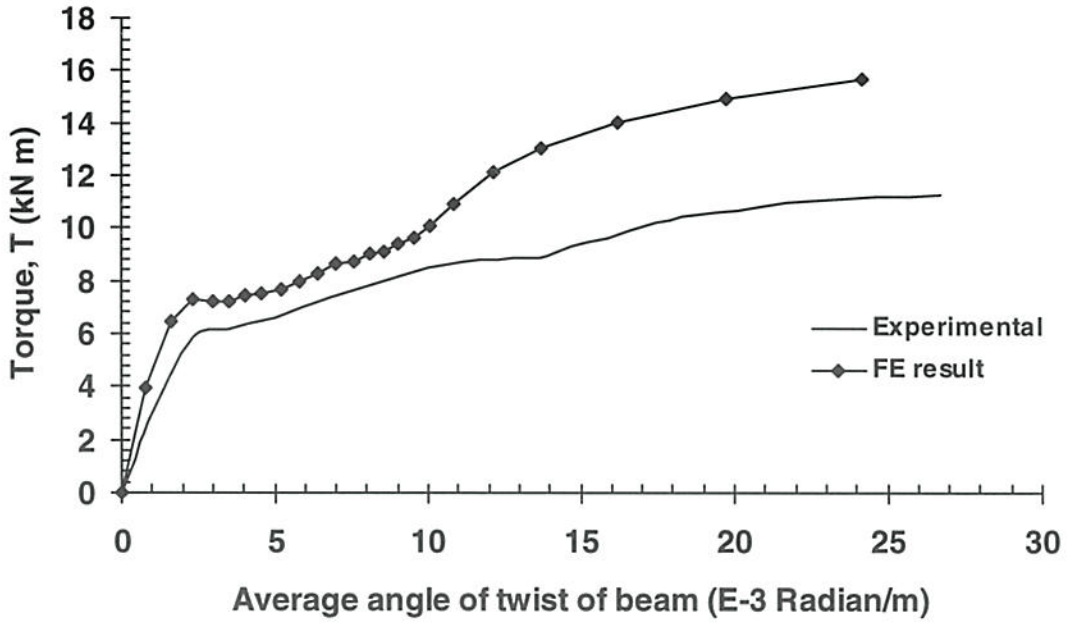

Figure 6.7 – Torque versus twist curves for spandrel beam.

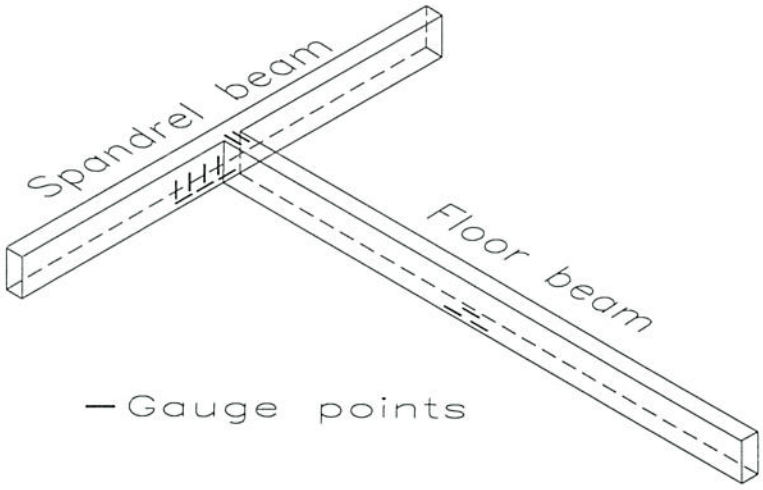

Figure 6.8 – Locations of gauge points for measuring strain in steel (Specimen SB-2 Mansur and Rangan 1978).

The relatively high strains in the gauged stirrup at low loads in the spandrel beam (shown in Figure 6.11) and the stiffer response of the sections than that evidenced in the load displacement curves, indicate that the beam may have been subject to some pre-cracking before testing. On the whole, however, it is concluded that the finite element model gives a good prediction to the overall response of the floor-spandrel beam system.

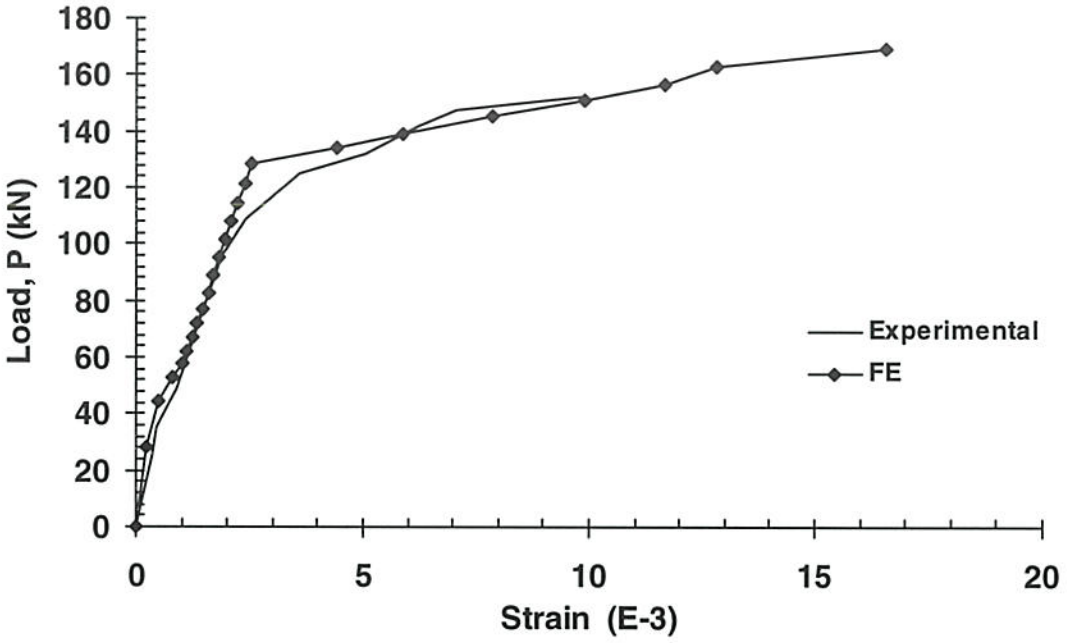

(a) Bottom bar

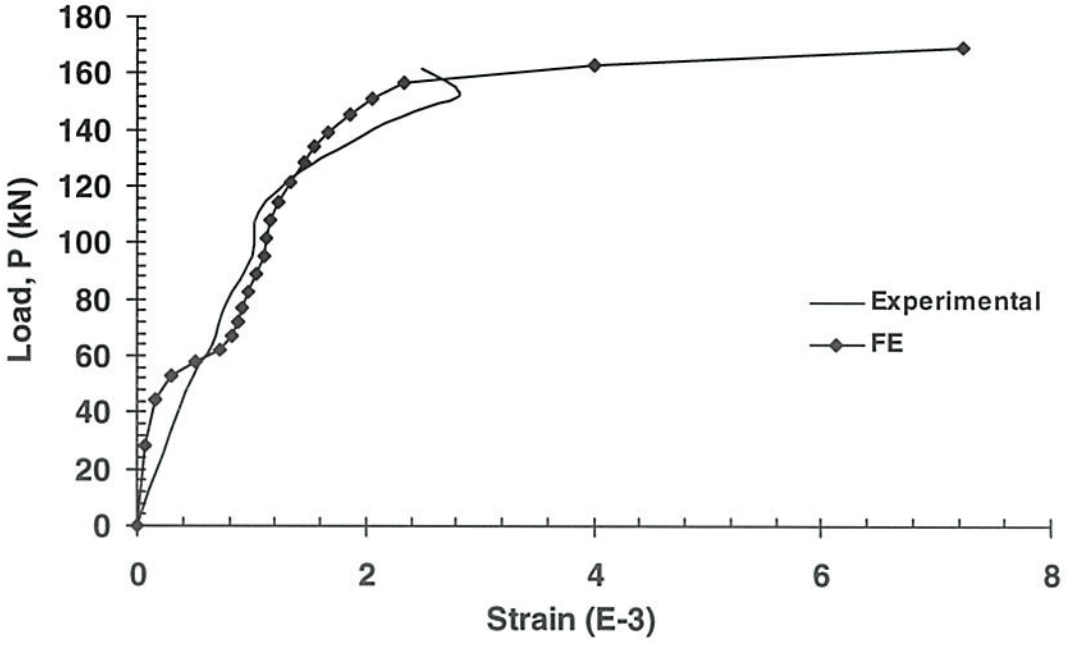

(b) Top bar

Figure 6.9 – Load versus steel strain curves for floor beam (a) Bottom bar b) Top bar.

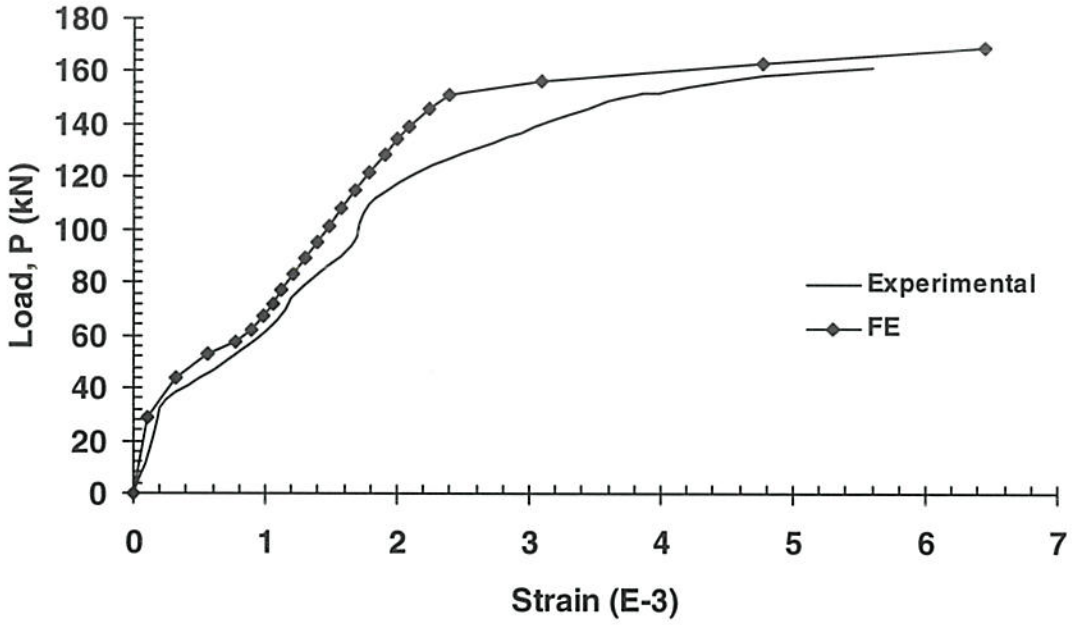

Figure 6.10 - Load versus steel strain curves for the bottom longitudinal bars of the Spandrel beam.

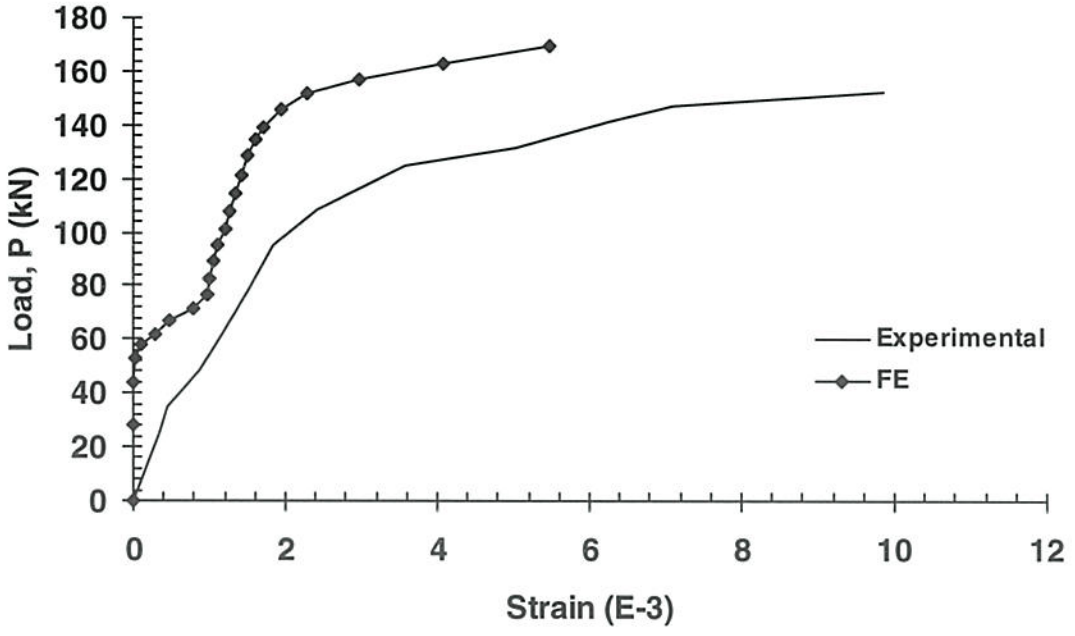

Figure 6.11 - Load versus steel strain curves for the stirrup of the spandrel beam.

6.3 RC Slab-Column Connection of Rangan and Lim (1992)

6.3.1 Finite Element Modelling

Lim and Rangan (1992) tested three slab-column connections for punching shear with two of the three specimens containing shear studs at the connections to increase the punching shear strength of the slab. Specimen Slab 1 contained no shear connectors and was analysed in this study.

Specimen Slab 1 consisted of a 4950 by 3170 mm slab with a column of 250 mm square located at the middle of its free edge. The specimen details and the arrangement of the steel reinforcement are shown in Figure 6.12. The base of the column was pin supported. The slab edge adjacent to the column was free while the opposite edge and the side edges rested on I-beams. The slab was restrained against lifting at the corners by placing a beam across all top corners of the slab. However, no direct connection was made from the supports to the slab and, thus, the slab was free to slip horizontally against the boundaries. The equilibrating horizontal forces for the horizontal reaction measured at the base of column could then only have come from friction of the slab against the I-beams, or from restraint developed at the corners where the slab was prevented from lifting, or both. The slab was loaded via 24 equal point loads evenly distributed across the slab simulating a uniform loading.

The finite element mesh used for the analyses is shown in Figure 6.13 and the boundary conditions are shown in Figure 6.14. One half of the slab-column connection was modelled due to symmetry (Figure 6.13). The slab-column connection was modelled using 504 by 20-node isoparametric brick elements. The reinforcing steel was modelled using 78 embedded bar elements. To model the boundary friction the corners of the slab (marked A and B in Figure 6.14) were restrained in the x, y, and z directions and the fixity of the column in x was replaced with a spring of variable stiffness. These boundary conditions being statically equivalent to fixing the column base in the x-direction and applying horizontal springs at the corners. The stiffness of the spring at the base of the column was then tuned to simulate different boundary conditions.

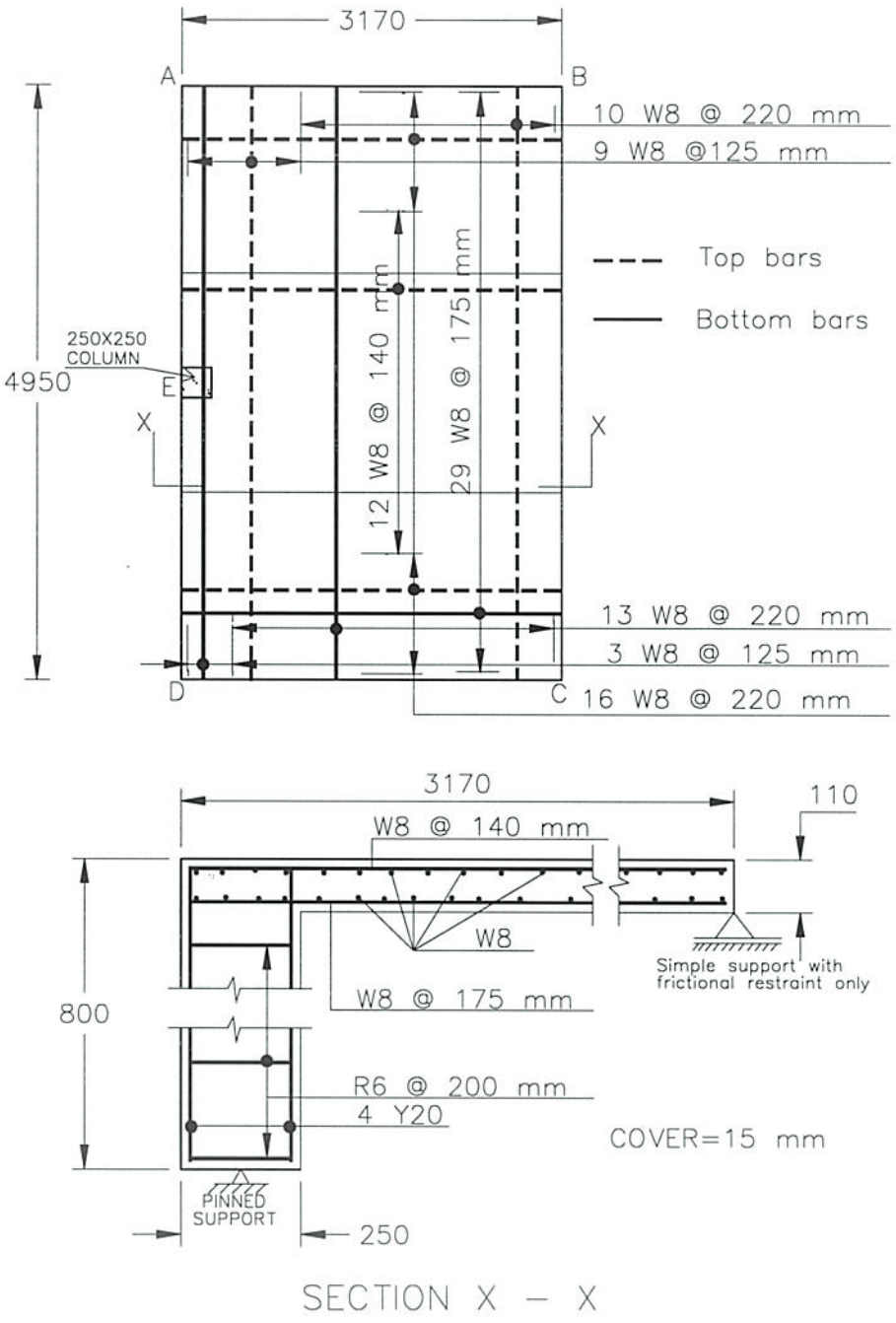

Figure 6.12 – Slab specimen S1 (Rangan and Lim, 1992).

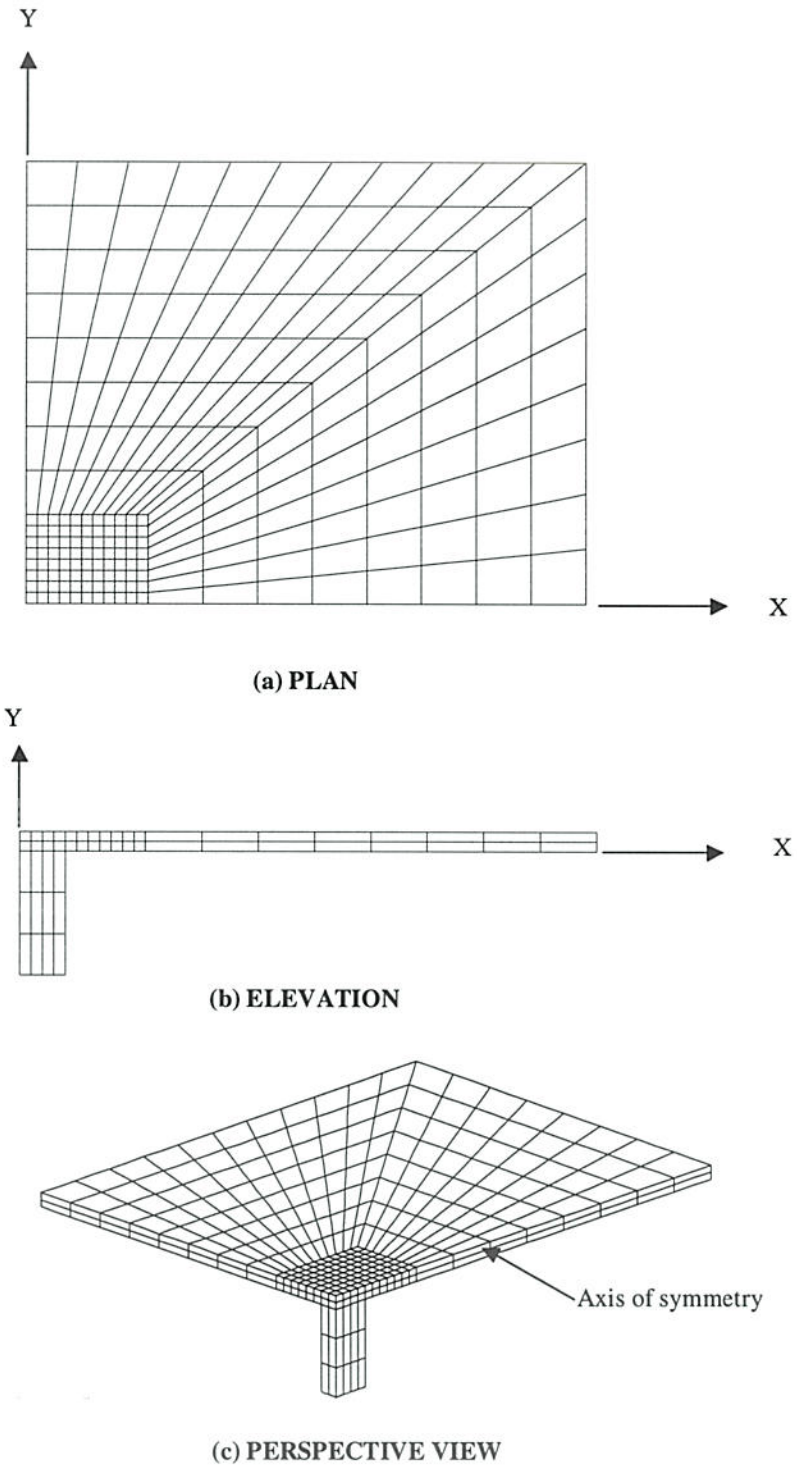

Figure 6.13 - Finite element model of the slab S1 (Rangan and Lim, 1992). (a) Plan, (b) Elevation and (c) Perspective view.

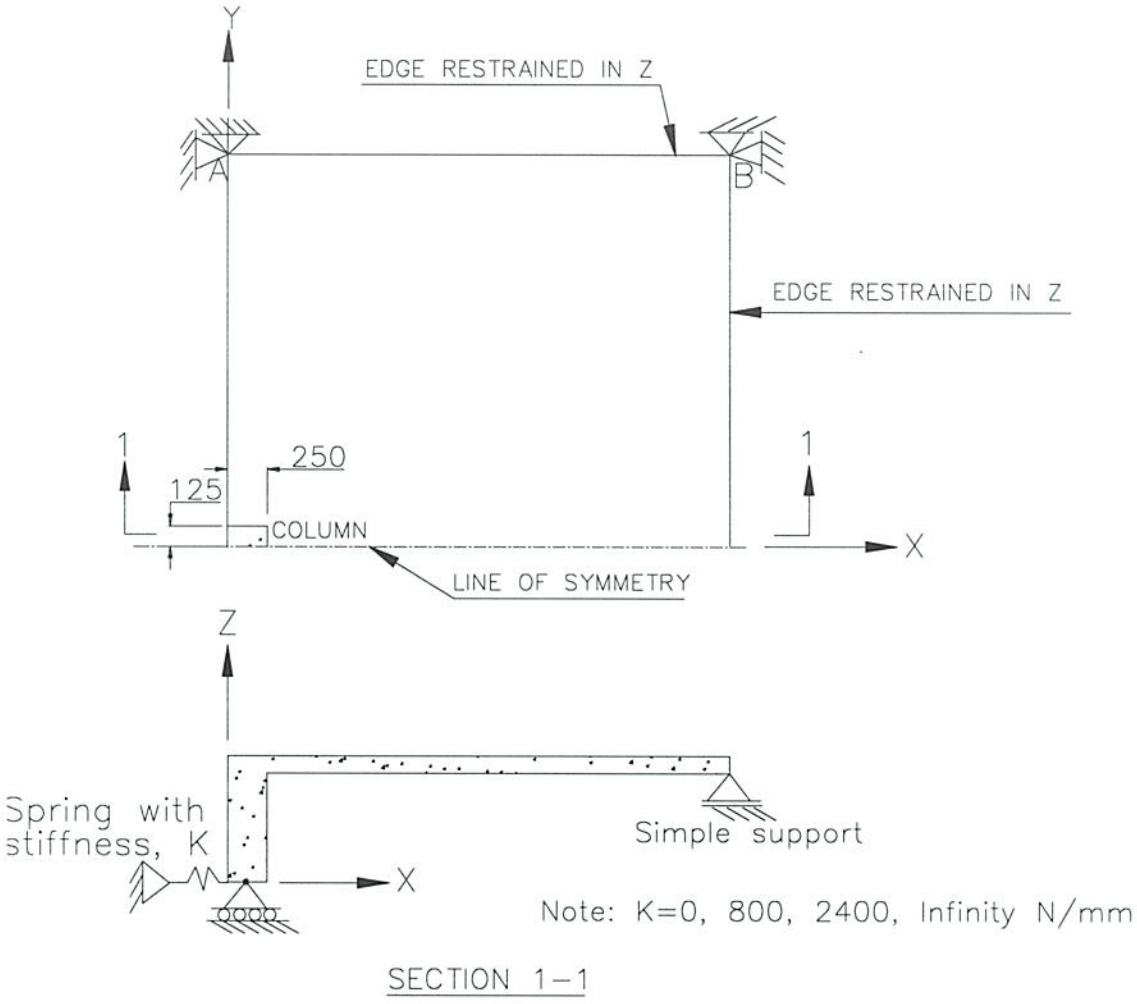

Figure 6.14 – Boundary conditions used in the FE model.

The recorded mean cylinder strength at the time of testing was 25 MPa. In the finite element modelling, the in-situ strength of the concrete was taken as $f_{cp} = 0.9 f_{cm}$. The material parameters for concrete were taken as:

f_{cp} = 22.5 MPa	f_t = 1.7 MPa	E_c = 26.0 GPa
α_1 = 12.	β = 0.2	$\alpha = 15^\circ$
$\phi = 30^0$	$\psi = 12.6^\circ$	μ = 0.2
ε_0 = 0.002		

The properties of the reinforcing bars used are given in Table 6.2.

The spring at the base of the column (in the x-direction) was modelled using stiffnesses of $K = 0$ N/mm (free), $K = 800$ N/mm, $K = 2400$ N/mm and $K = \infty$ (fully restrained). The stiffness $K = 800$ N/mm was selected to match the measured horizontal load in the column under elastic conditions.

The calculated failure loads from each of the analyses are presented in Table 6.3. The load versus mid-panel deflection and load versus vertical column reaction are given in Figure 6.15 and Figure 6.16, respectively. The vertical reaction versus the horizontal x-direction reaction is plotted in Figure 6.17.

With the increase of stiffness, the load carrying capacity of the system is found to decrease. The transfer of load through the connection depends on the combined effect of the shear and the moment interaction. With the increase of spring stiffness the bending moment transferred to the connection increases causing a reduction in overall load carrying capacity.

The mid-span deflections for the finite element analyses and the experimental slab are shown in Figure 6.15. A reasonable correlation is seen between the experimental data and the finite element model for the slab. Figure 6.15 also shows that the slab deflections are not sensitive to the spring stiffness. The main variance between the numerical deflections and those recorded in the laboratory is in the pre-cracked elastic range with negligible deflections being measured in the laboratory.

The vertical reaction at the base of the column is plotted against the total slab load in Figure 6.16. The figure shows that the vertical reaction in the column and hence, the shear transferred to the slab is not sensitive to the spring stiffness.

The greatest sensitivity to the boundary conditions is seen in the development of base shear at the column, shown in Figure 6.17. With $K = 0$, that is with no lateral restraint at the base of the column, no unbalanced moment occurs at the column-slab joint. With infinite spring stiffness the horizontal reaction and consequently the unbalanced moment at the connection is significantly greater than that measured in the laboratory. The best match is with K = 800 N/mm. In the load versus the horizontal reaction of the column the influence of boundary conditions is clearly demonstrated.

Table 6.2 – Material properties of reinforcing bars.

Material Property		6 mm Dia. Bar	8 mm Dia. Bar	20 mm Dia. Bar
Area A_s	(mm^2)	28	50.0	314
Yield strength	(MPa)	250	516	415
Ultimate strength	(MPa)	250	516	415
Young's modulus	(GPa)	200	173	200

Table 6.3 – Failure load for different base spring stiffnesses.

Stiffness, K (N/mm)	Failure Load (kPa)	Mode of Failure
0	39	Flexure
800	32	Flexure/Punching Shear
2400	25	Punching Shear
∞	19	Punching Shear
Experimental	22	Punching Shear

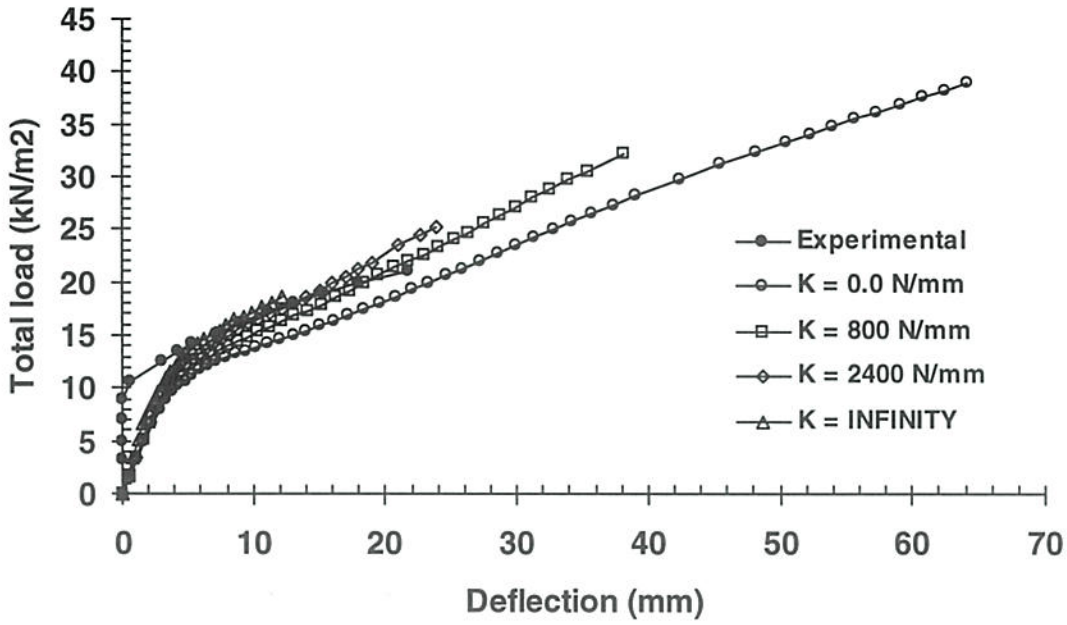

Figure 6.15 – Load deflection curves.

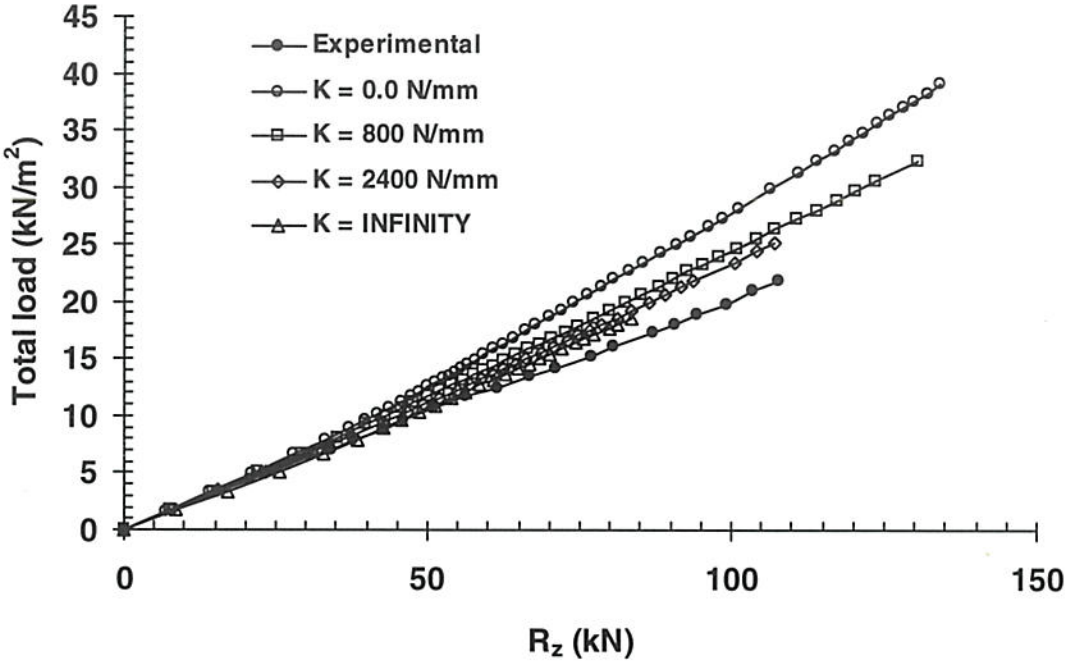

Figure 6.16 - Load shear force curves.

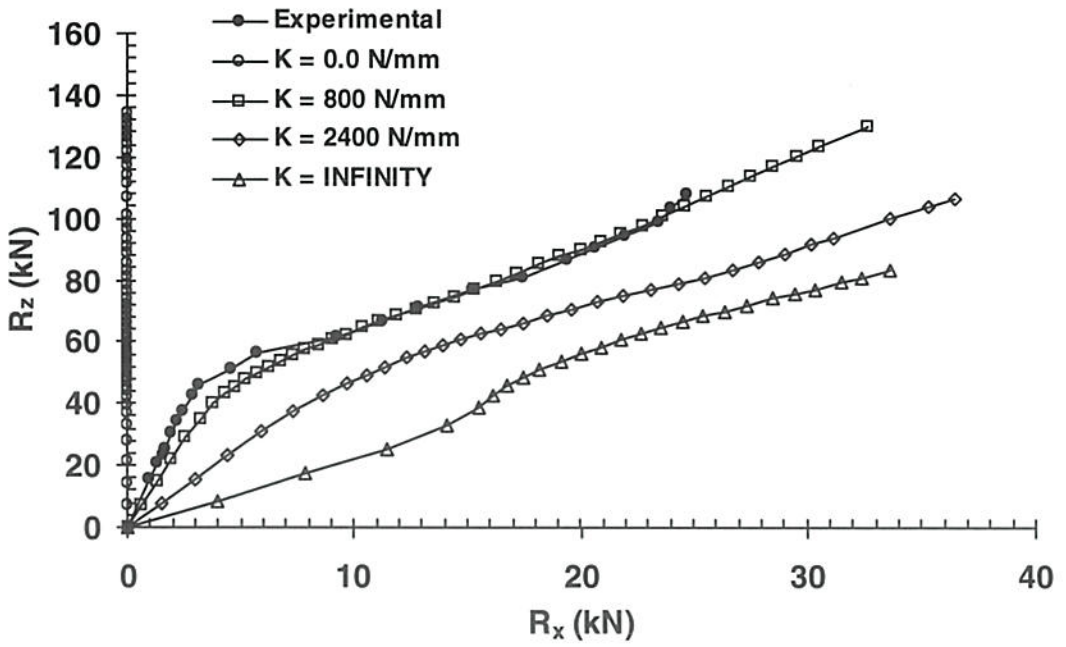

Figure 6.17 –Vertical reaction (R_z) versus the horizontal reaction (R_x) at the base of the column.

In addition to influencing the column base shear and, hence, the unbalanced moment in the column, the spring stiffness affects the strains in the negative moment reinforcing steel. Figure 6.18 shows the strain in the short span central top steel at the edge of the column. The strain is small when the lateral restraint is zero and increases with increasing spring stiffness. The maximum strain in the short span bottom reinforcement, near the midspan, is shown in Figure 6.19. The reinforcement for the spring stiffnesses of $K = 0.0$ N/mm and $K = 800$ N/mm were found to have yielded before the advent of punching failure. This indicates some load redistribution occurred in the slab prior to failure. No strain measurements on the steel were recorded in the experimental study.

This study shows the influence of boundary conditions in the laboratory test results. The boundary conditions have a significant effect on the moment transferred from the slab to the column in flat plate and flat slab structures. This in turn affects the capacity of the joint and puts into question how well the experimental model simulates a real structure. This study also showed that the slab deflections and the transfer of vertical load to the column are not significantly influenced by the boundary conditions.

6.3.2 Sensitivity Analyses

In modelling the punching type problems the behaviour of the cracked concrete is important in obtaining accurate and reliable results for the failure load and failure mechanism. In this respect, the sensitivity analyses presented in Section 5 show that the parameters α_1 and β are of fundamental importance. Model 2 ($K = 800$ N/mm) was chosen for further sensitivity analyses for the concrete tension parameters α_1 and the shear retention factor β.

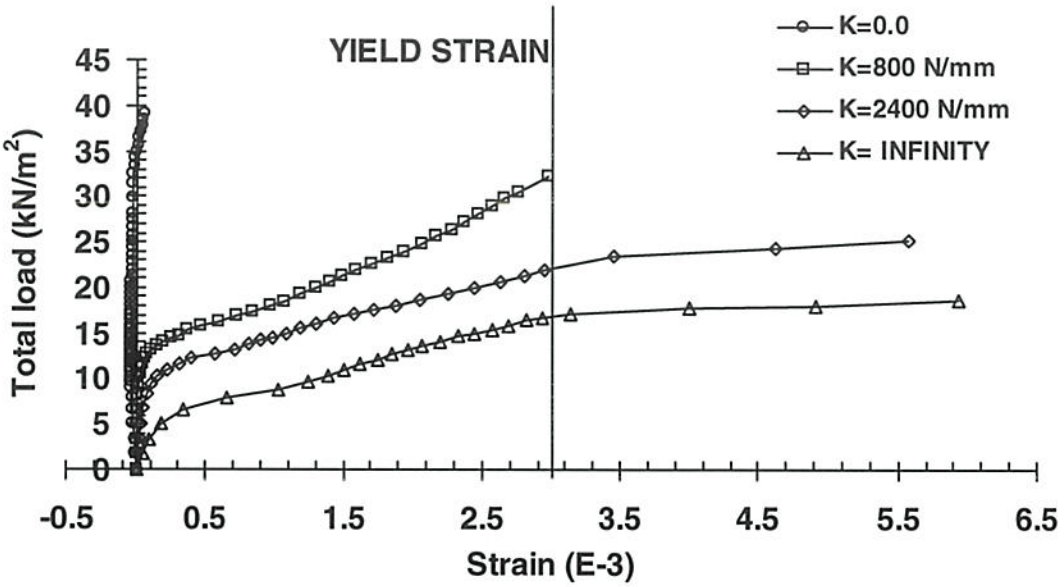

(a) Central top reinforcement bar

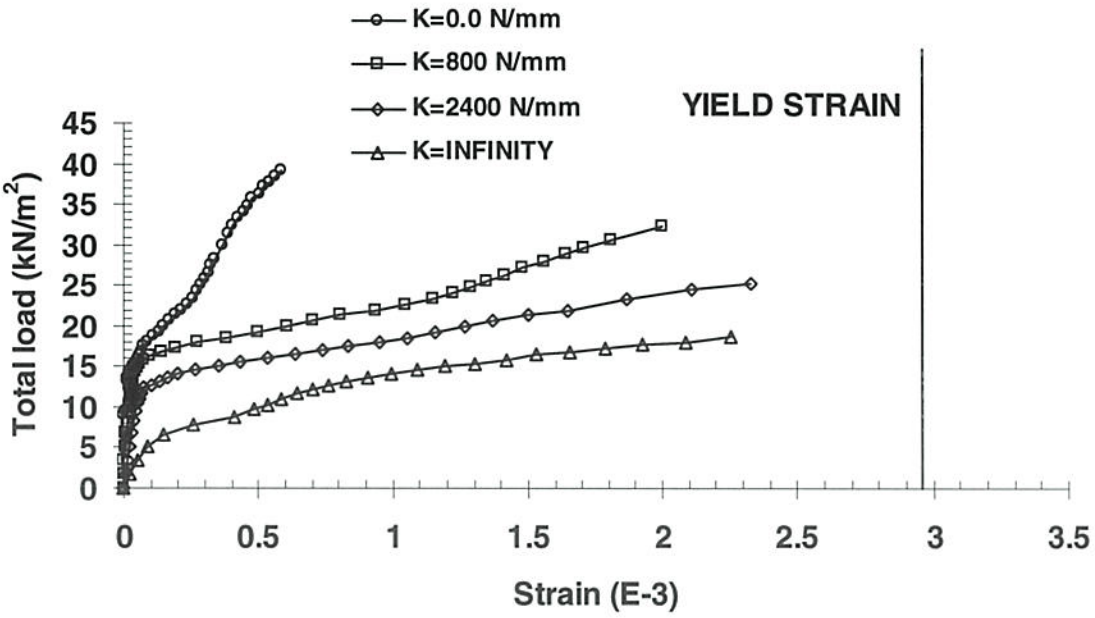

(b) Bar immediately adjacent to the column

Figure 6.18 - Maximum strains developed in the short span reinforcements.

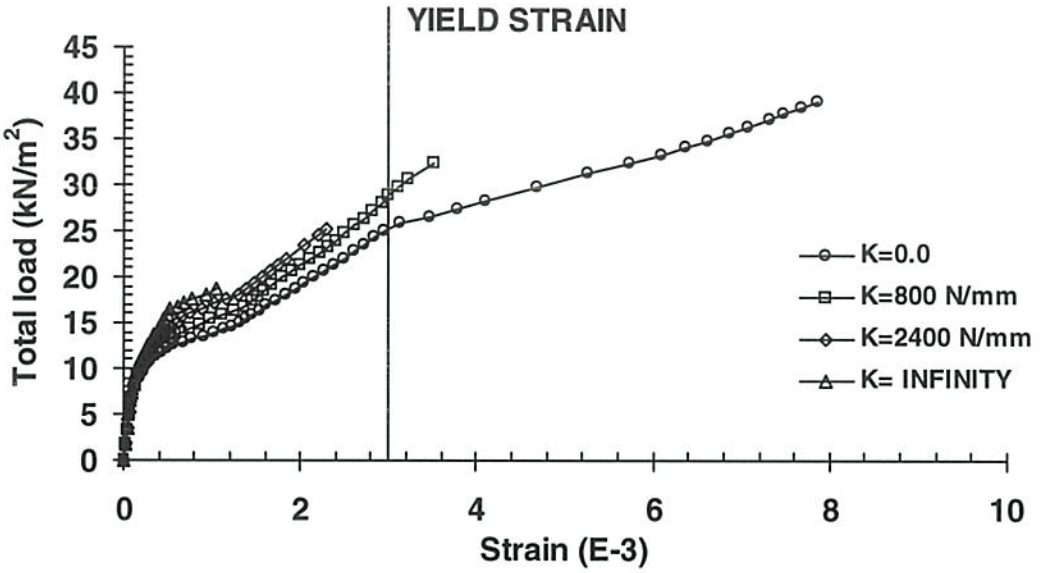

Figure 6.19 - Comparison of maximum strains developed in the short span central bottom reinforcement (mid-span) for varying degrees of lateral restraint.

Sensitivity to α_1

With the development of cracks, the stiffness of the concrete reduces. This reduction and its rate is dependent on ε_u (refer Figure 2.2). The ultimate uniformly distributed load on the slab predicted from the finite element analyses with a constant shear retention factor of $\beta = 0.2$ and for different values of the parameter α_1 are given in Table 6.4 and shown in Figure 6.20 and Figure 6.21. The failure load, the displacement of the slab and the shear to moment ratio at the junction of the column and the slab are significantly influenced by the slope of the descending branch of the tension stress-strain curve for the concrete. The development of strain history in one of the critical bars (central top bar in the short span) is presented in Figure 6.22. The parameter α_1 is seen to be influential in the strain history of the steel and the failure mode.

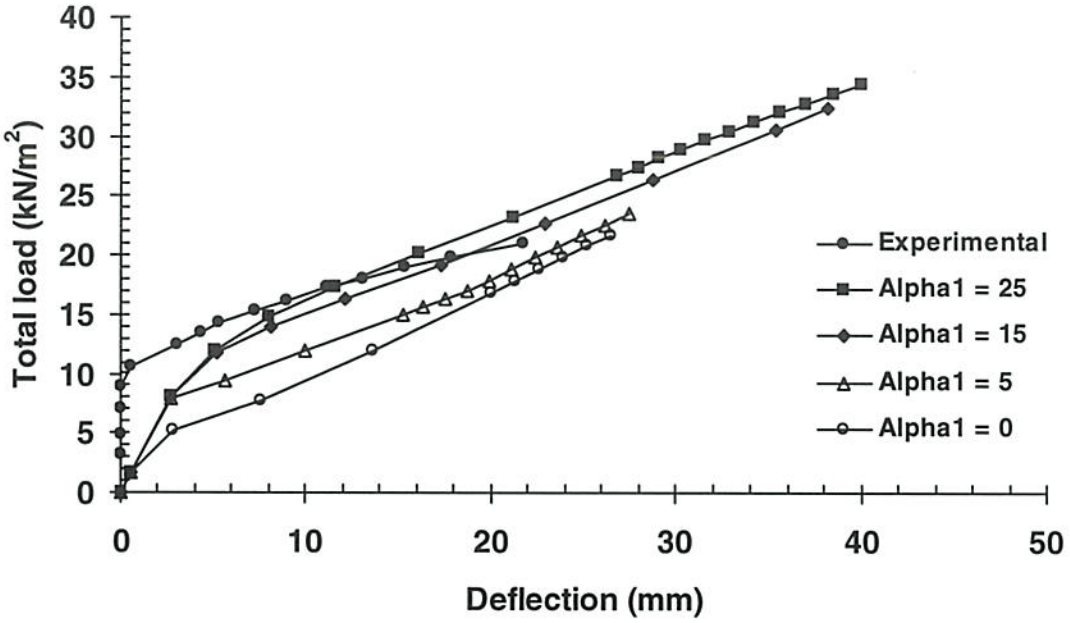

Figure 6.20 - Load versus deflection curves for the Rangan and Lim (1992) slab with different values of α_1.

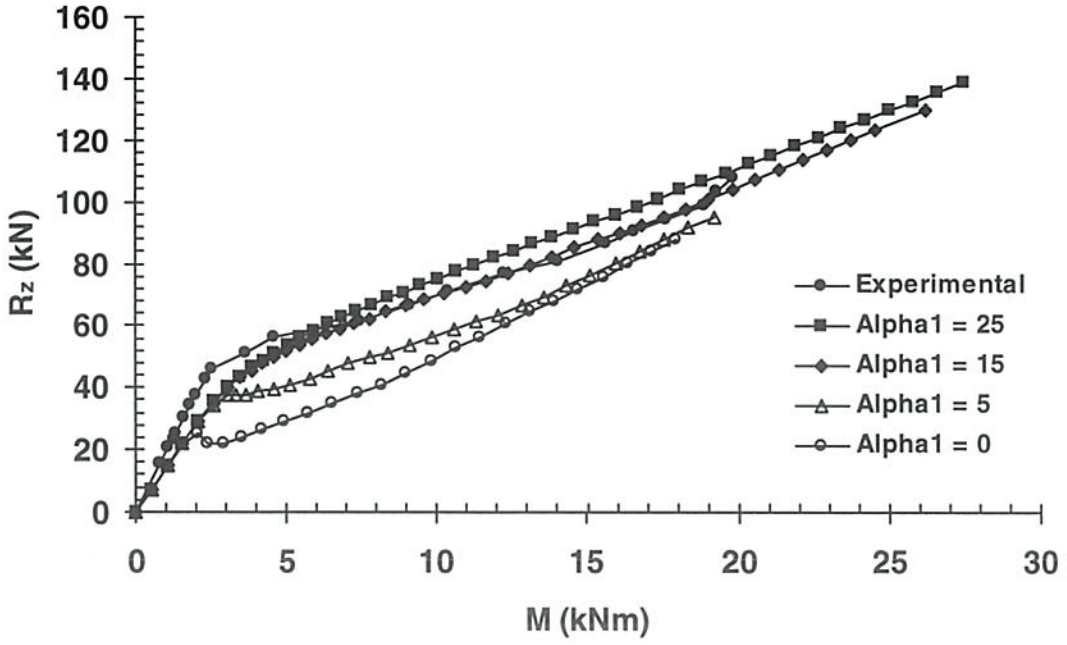

Figure 6.21 - Shear versus moment at the column slab connection for the Rangan and Lim (1992) slab with different values of α_1.

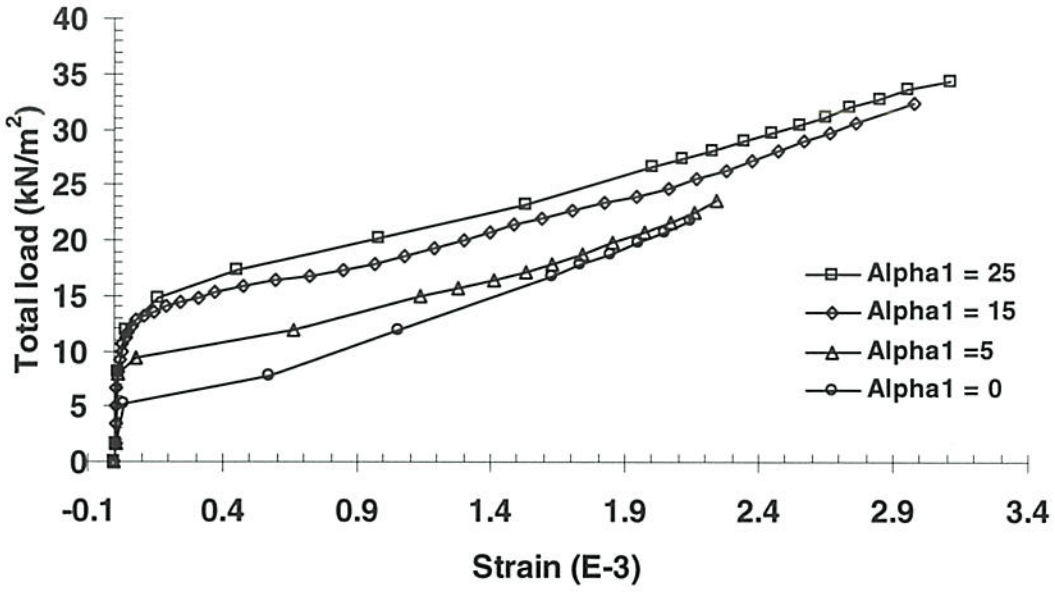

Figure 6.22 - Load versus strain for the central top bar for the short span for the Rangan and Lim (1992) slab S1 for different values of α_1.

Table 6.4 - Ultimate load for different values of α_1.

Model	Value of α1	Ultimate Load (kPa)
2-A	0	21.7
2-B	5	23.5
2	15	32.4
2-C	25	34.4
5	Experimental	22

Sensitivity to β

For fully cracked plain concrete the shear stiffness becomes small after the onset of cracking. However, in reinforced concrete the interaction of the reinforcement crossing the cracks on the influence of aggregate interlock is significant. Although the effect of shear stiffness of cracked concrete is acknowledged as important in the FE modelling community, no consensus is found amongst researchers on a satisfactory mathematical model. The model with *K=800* N/mm is analysed with $\alpha_1 = 15$ for different values of β.

The effect of the shear retention factor on the slab deflections, the distribution of vertical to horizontal loads at the base of the column, the development of strain in the top reinforcement at the centre of the column and on the failure loads are given in Figure 6.23 to 6.25 and Table 6.5, respectively. The analyses show that the shear retention factor does not influence the results of the load versus displacement; the distribution of horizontal to vertical reaction and, hence, the shear to moment ratio at the slab-column intersection; or the development of strain with increasing applied load in the negative moment reinforcement in the vicinity of the connection. However, the value of β chosen has a significant influence on the failure load. The failure load varied by up to a factor of two depending on β (see Table 6.5).

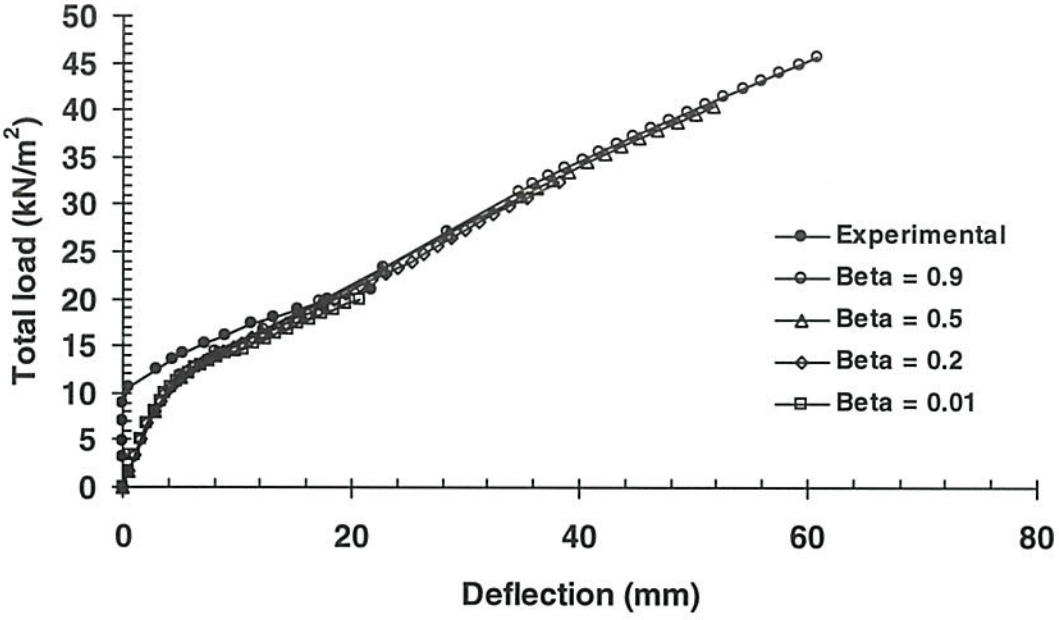

Figure 6.23 - Load versus deflection curves for the Rangan and Lim (1992) slab-column connection with different values of β.

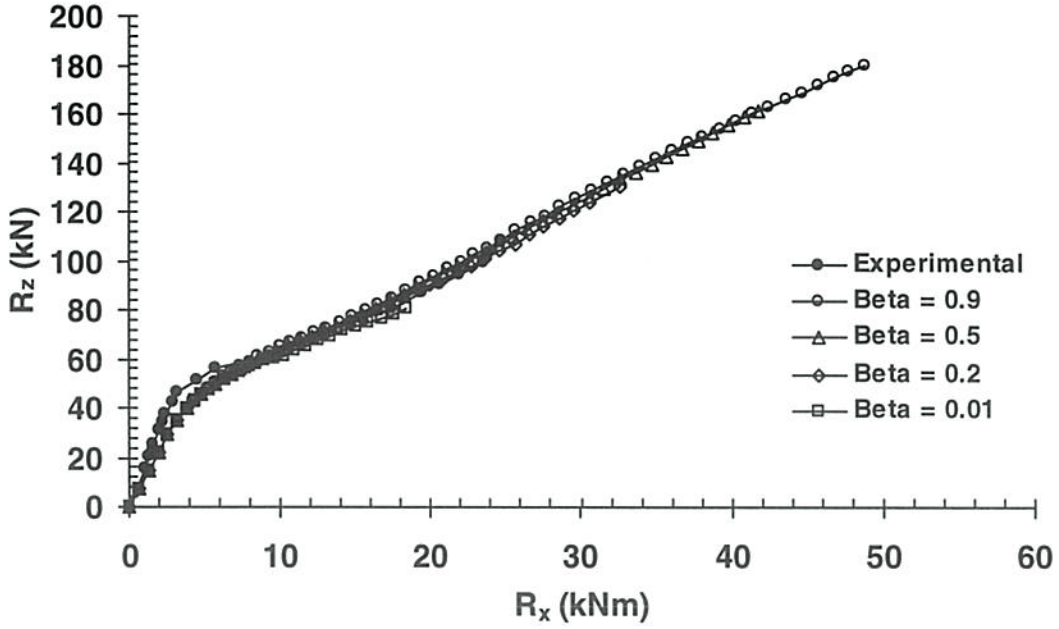

Figure 6.24 – Vertical versus horizontal reactions at the column for the Rangan and Lim (1992) slab S1 for different values of β.

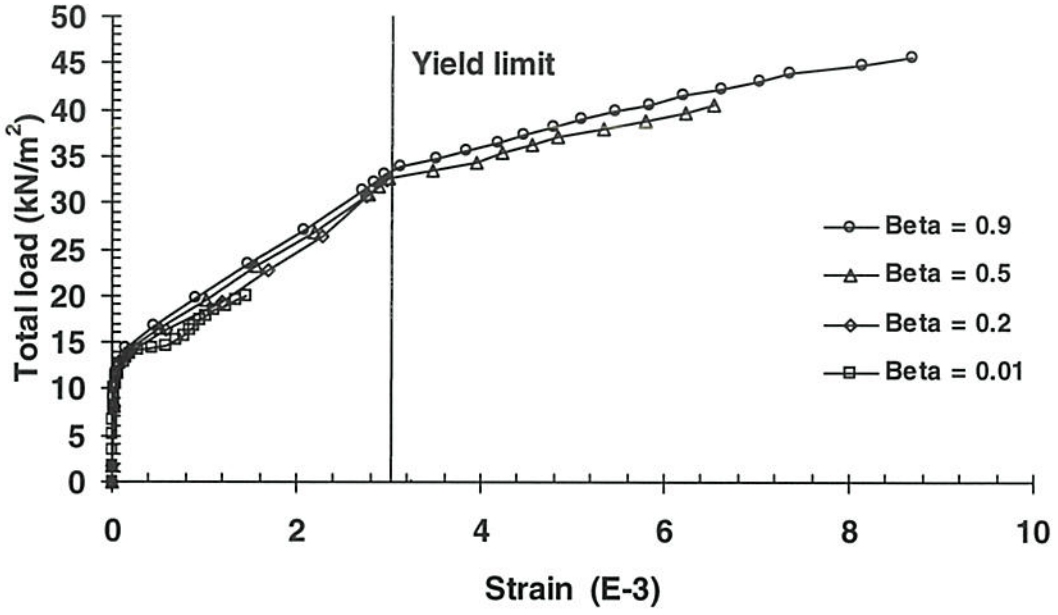

Figure 6.25 - Load versus strain for the central top bar for the short span for the Rangan and Lim (1992) slab S1 for different values of β.

Table 6.5 - Ultimate load for different values of β.

Model	Value of β	Ultimate Load (kPa)
2-D	0.01	20.0
2	0.20	32.4
2-E	0.50	40.5
2-F	0.90	45.7
5	Experimental	22.0

6.4 Prestressed Concrete Slab–Column Connections of Foutch et al. (1990)

Foutch et al. (1990) tested four post-tensioned slab-edge column connections. The specimens were based on a two-third scale model of a prototype structure. The specimens are identical in the external dimensions and had similar boundary conditions. The outlines of the specimens with the loading points are shown in Figure 6.26. The arrangement of the bonded non-prestressed reinforcement in the specimens is shown in Figure 6.27. The locations of the tendons for specimens S1 and S2 are shown in Figure 6.28a. The location of the tendons for specimens S3 and S4 are shown in Figure 6.28b.

The properties of the concrete, reinforcement and tendons used in the test are presented in Tables 6.6 to 6.8. The tests were carried out using whiffle tree to apply four vertical loads arranged symmetrically at a distance of 1.07, 0.61, 0.61 and 0.305 metres from the front face of the column for specimens S1, S2, S3 and S4 respectively (see Figure 6.26).

The specimens were modelled using the mesh shown in Figure 6.29 with one half of the specimen modelled due to symmetry. The finite element model had 276 20-node solid isoparametric concrete elements with 1755 nodes. The bonded reinforcement and the prestressing tendons were modelled using embedded elements defined by 120 nodes for specimens S1 and S2 and 114 nodes for specimens S3 and S4. The reinforcement was placed in the same location for all specimens. Perfect bond was assumed between the bonded non-prestressed reinforcement and the concrete. The pinned supports were applied at the top and at the bottom of the column, matching that of the experimental test set up. The Hognestad (1951) model was used to model the concrete compressive stress strain diagram with the concrete strength taken as $f_{cp} = 0.90\, f_{cm}$, where f_{cm} is the mean cylinder strength of the concrete at the time of test. The concrete tension strength was taken as $f_t = 0.33\sqrt{f_{cm}}$ MPa.

The ultimate loads are given in Table 6.9. Figure 6.30 to Figure 6.33 show the load versus displacement of the slab edge (shown as point A in Figure 6.26) for slabs S1 to S4, respectively. In Figure 6.34 to Figure 6.37, the load versus strain in the steel reinforcement is compared for different bonded reinforcements at the locations shown in Figure 6.27. In all cases the numerical model is in good agreement with the measured response of the slab-column connection.

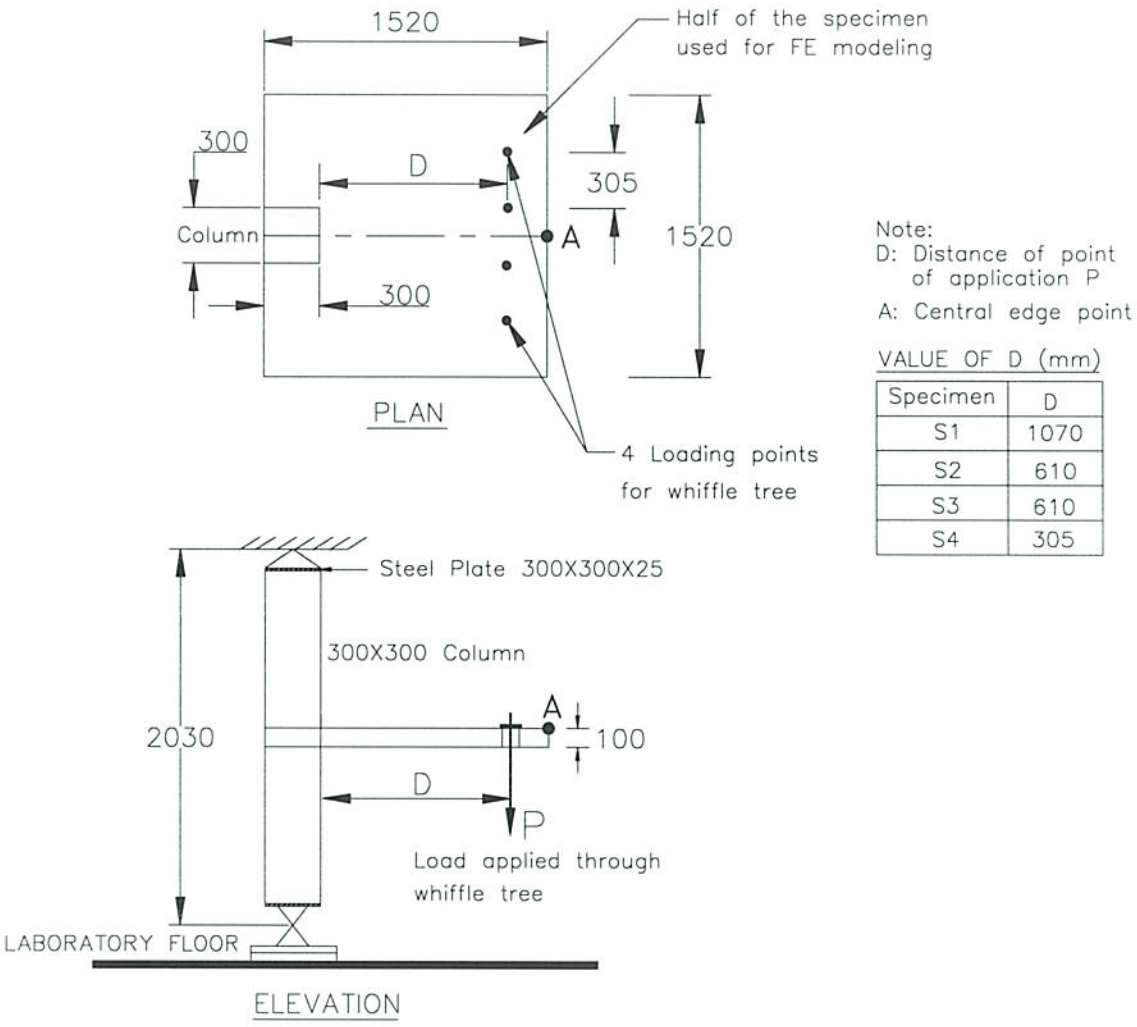

Figure 6.26 – Outline with key points for the Foutch et al. (1990) specimens.

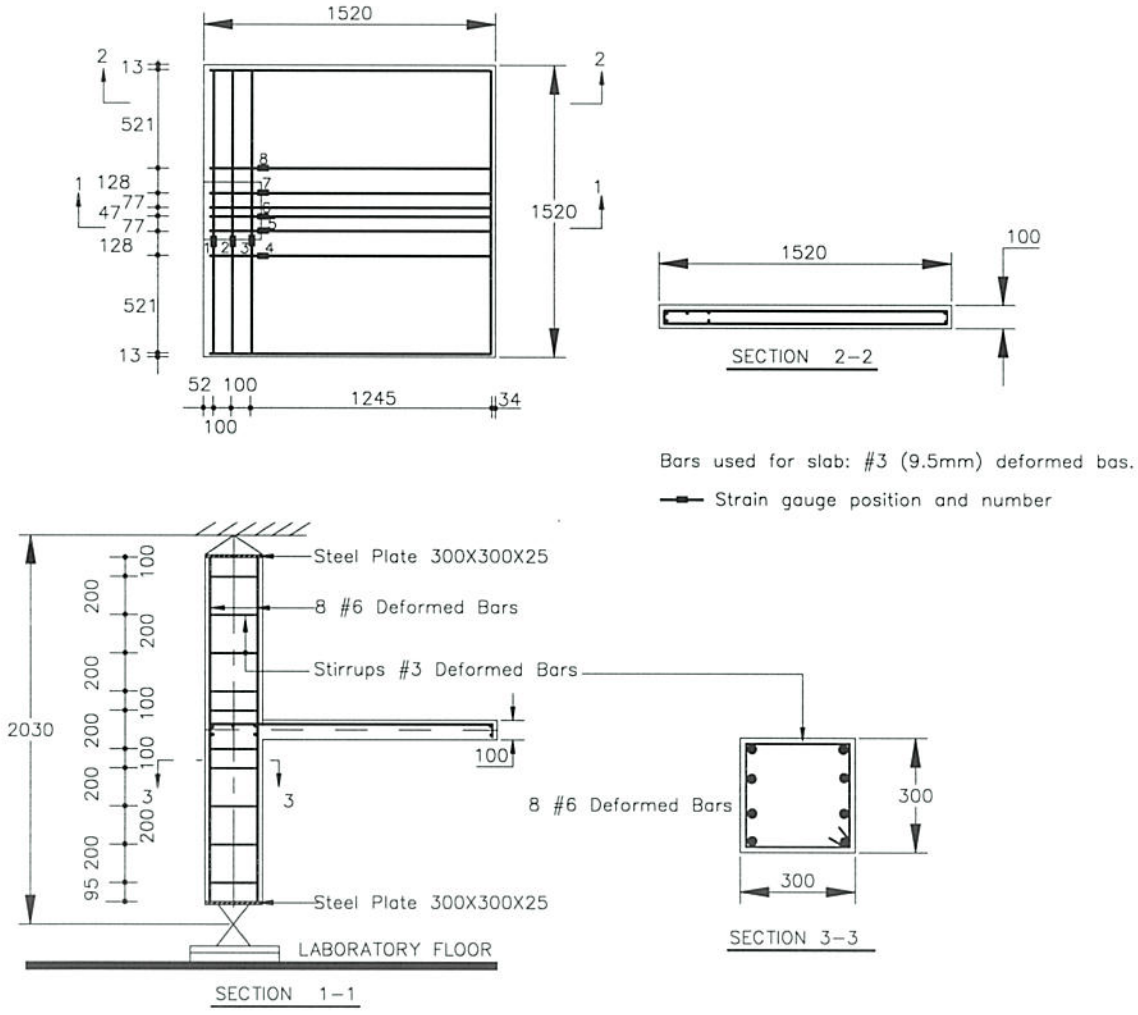

Figure 6.27 – Arrangement of non-prestressed reinforcement (Foutch et al., 1990).

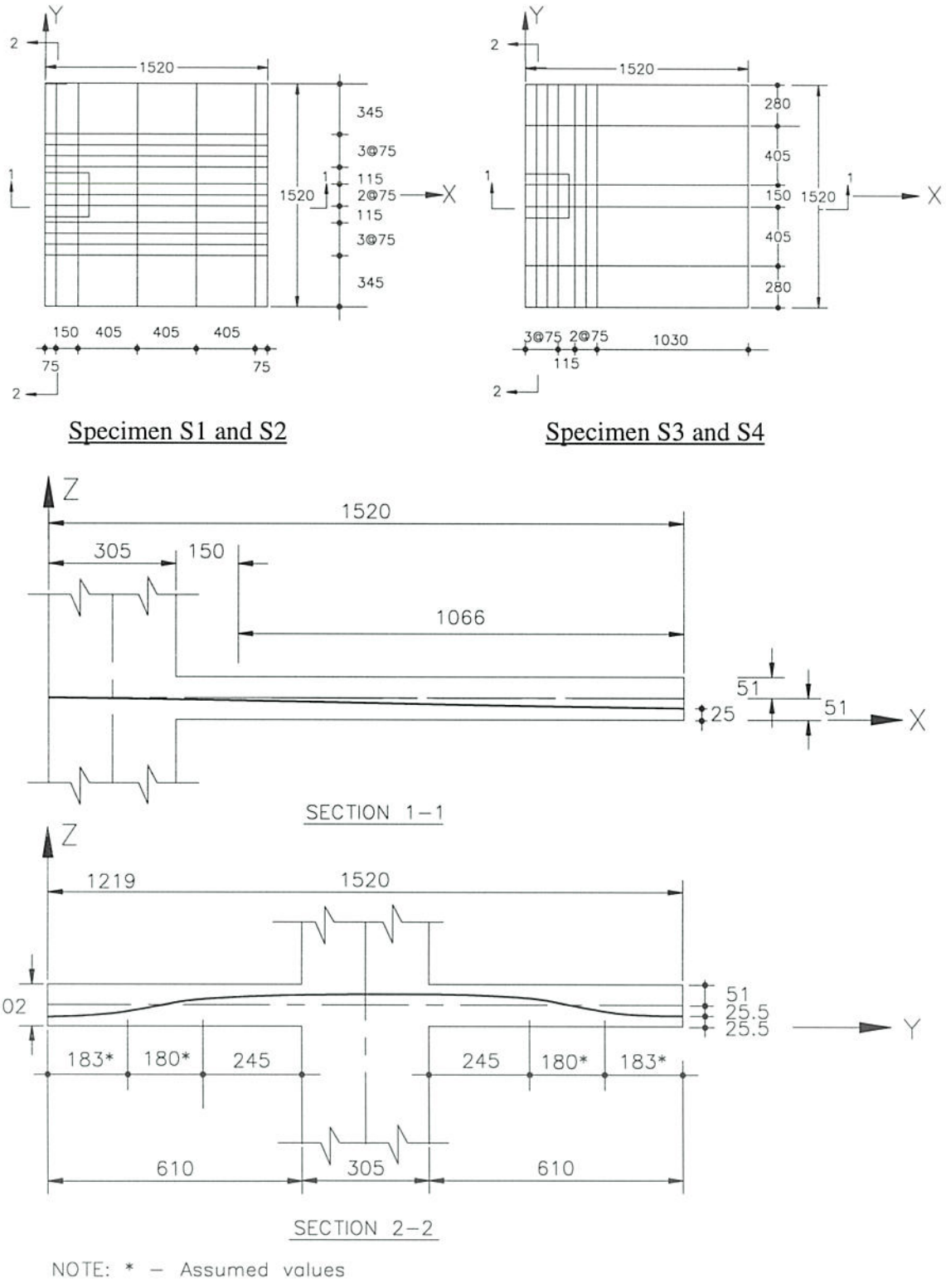

Figure 6.28 – Arrangement of tendons (Foutch et al., 1990).

Table 6.6 - Concrete properties used for the FE model (Foutch et al., 1990).

Material Property	Specimen S1	Specimen S2	Specimen S3	Specimen S4
$f_{cp} = 0.9\, f_{cm}$ (MPa)	45.3	38.5	37.9	43.4
f_t (MPa)	2.34	2.15	2.14	2.29
α (Degrees)	15	15	15	15
ϕ (Degrees)	30	30	30	30
ψ (Degrees)	12.6	12.6	12.6	12.6
α_1	17.6	17.4	17.5	17.5
μ	0.2	0.2	0.2	0.2
β	0.2	0.2	0.2	0.2
ε_0	0.002	0.002	0.002	0.002
E_c (GPa)	33.0	30.0	30.0	32.0

Table 6.7 – Material properties of reinforcing steel (Foutch et al., 1990).

Property		Bars	
		#3	#6
Area A_s	(mm^2)	71	284
Yield strength	(MPa)	501	501
Ultimate strength	(MPa)	835	793
Young's modulus	(GPa)	200	200
Ultimate strain	(%)	0.045	0.046

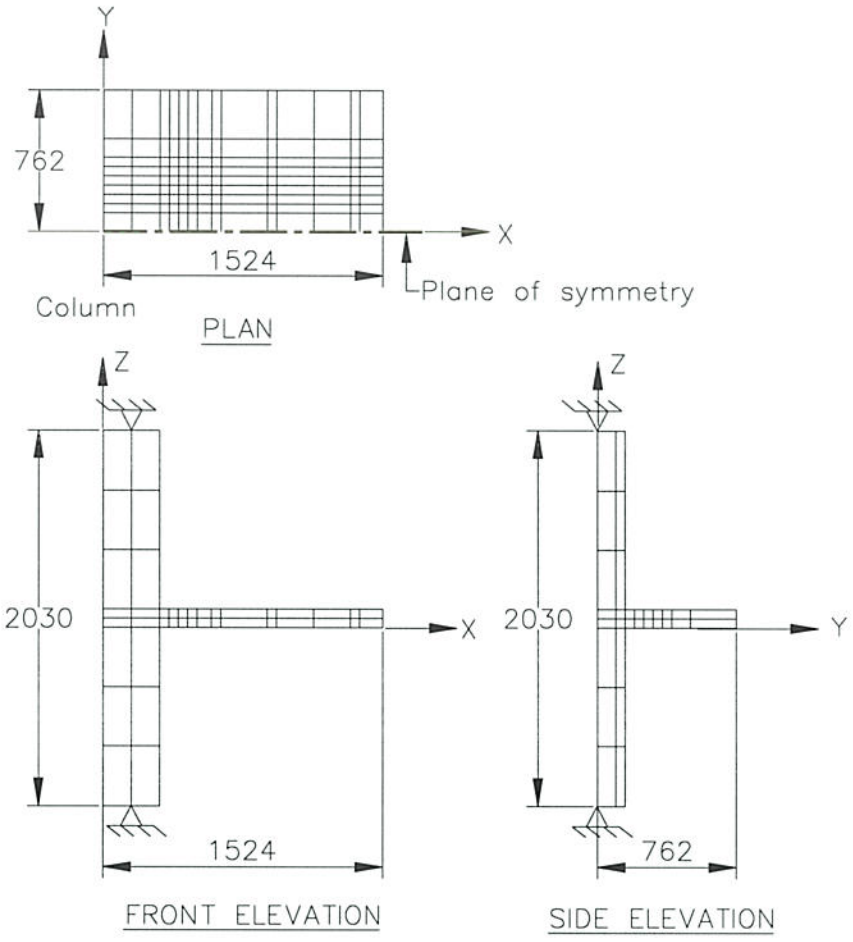

(a) Plan and elevations showing boundary conditions

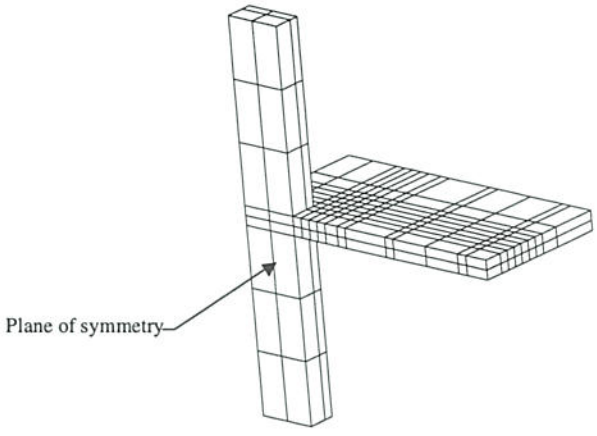

(b) 3D view

Figure 6.29 – Finite element model of the slab-column (a) Plan and elevations showing boundary conditions; and (b) 3D view.

Table 6.8 - Material properties of tendons, 3/8 inch - 7 Wire Strand.

Description		Values
Area A_s	(mm^2)	51.6
Yield strength	(MPa)	1900
Ultimate strength	(MPa)	1900
Young's modulus	(GPa)	195

Table 6.9 – Comparison of ultimate loads.

Specimen	Load Eccentricity (mm)	Ultimate Load (kN)	
		Experimental	Finite Element
Specimen S1	1070	58.0	61.0
Specimen S2	610	50.0	55.0
Specimen S3	610	40.0	44.0
Specimen S4	305	36.0	42.0

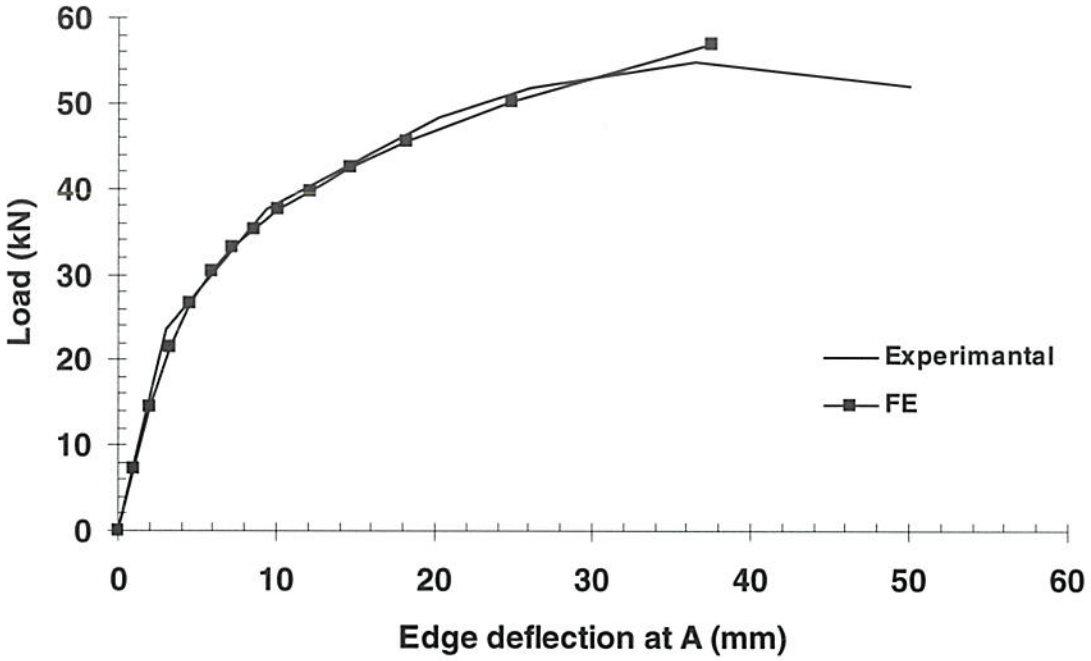

Figure 6.30 – Load versus deflection curves for Specimens S1.

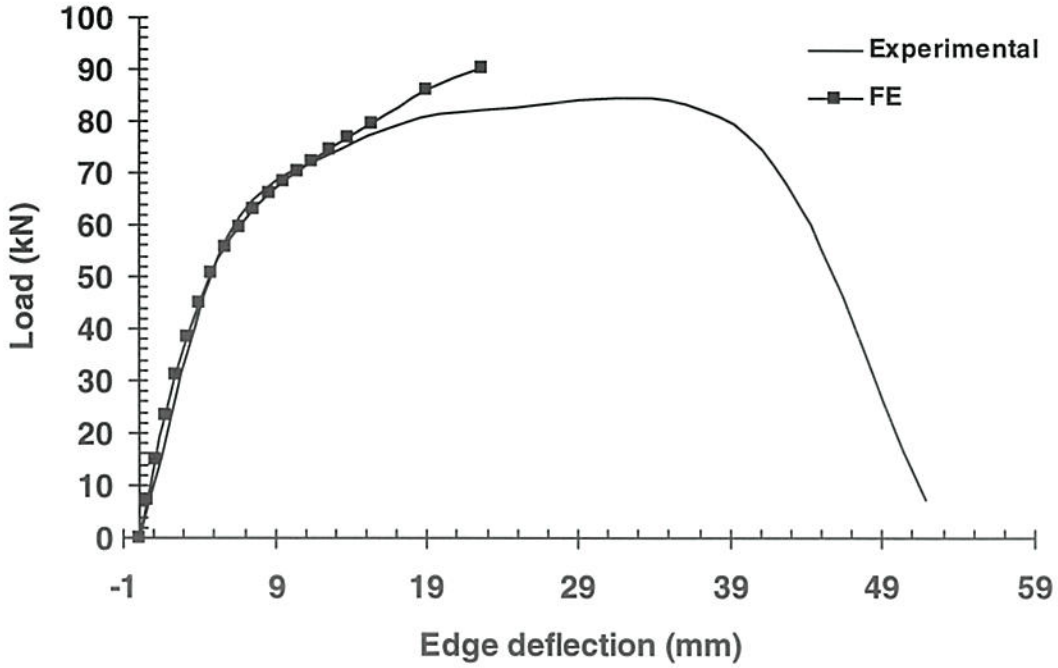

Figure 6.31 – Load versus deflection curves for Specimens S2.

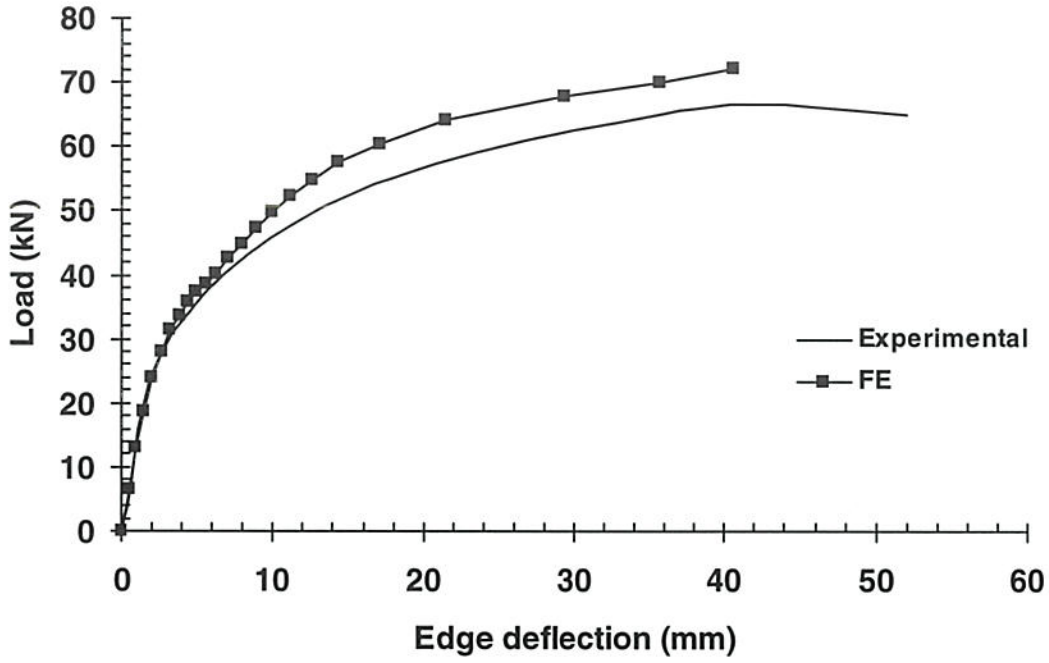

Figure 6.32 – Load versus deflection curves for Specimens S3.

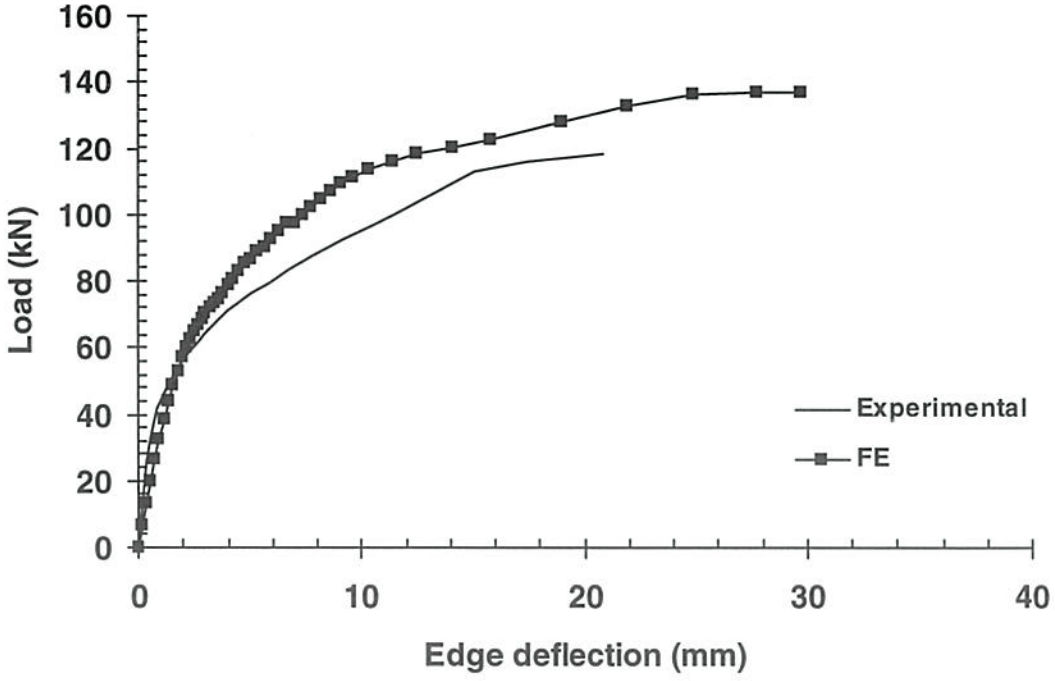

Figure 6.33 – Load versus deflection curves for Specimens S4.

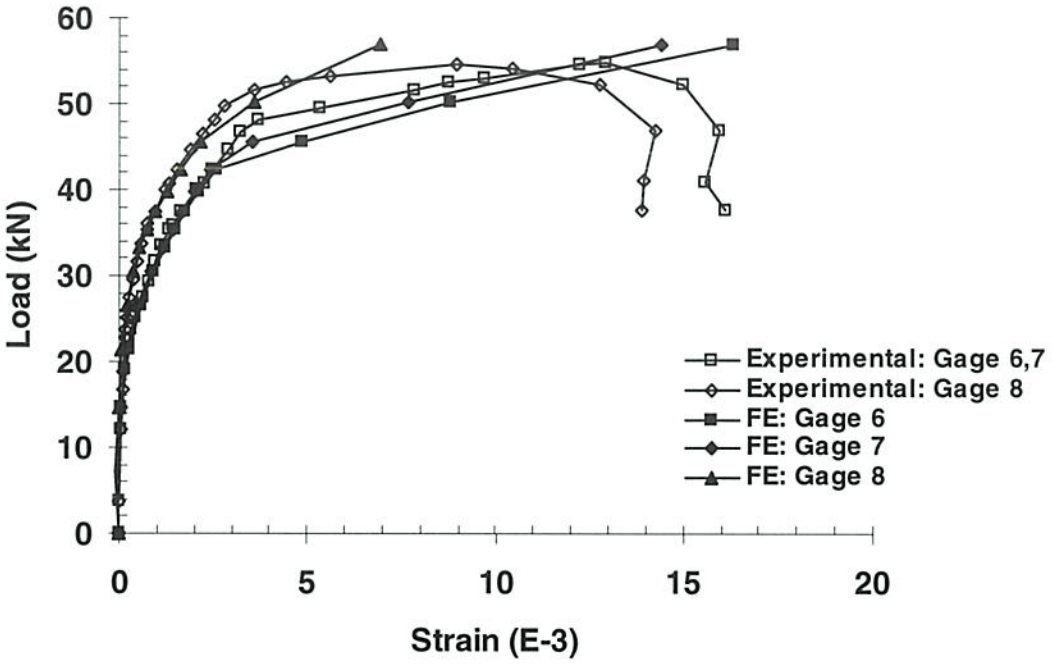

Figure 6.34 – Load versus reinforcement strain history for Specimen S1.

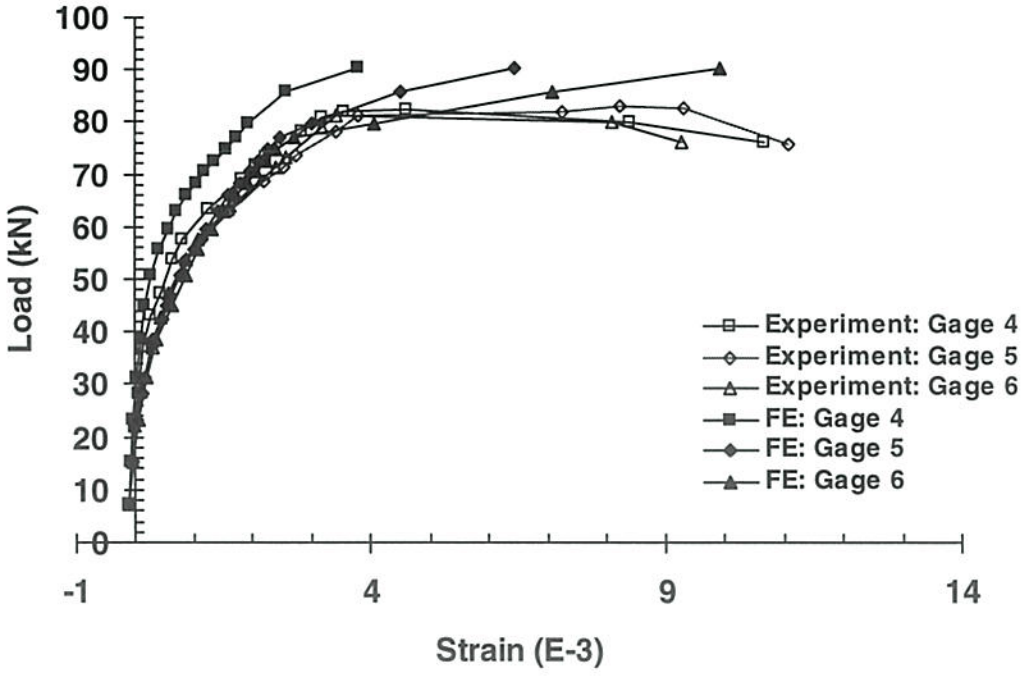

Figure 6.35 – Load versus reinforcement strain history for Specimen 2.

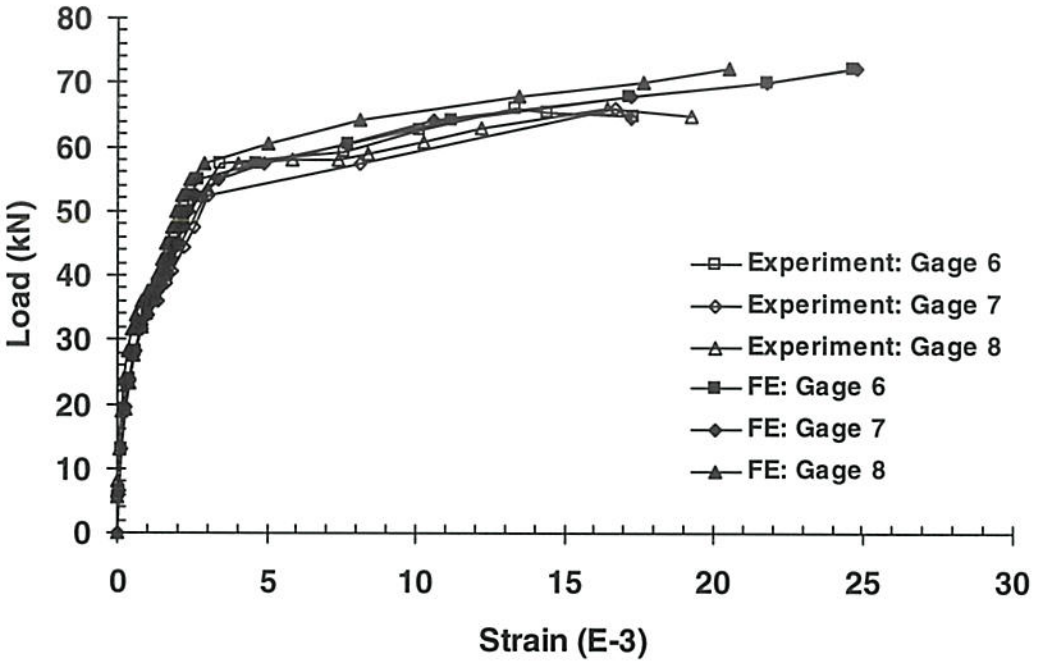

Figure 6.36 – Load versus reinforcement strain history for Specimen S3.

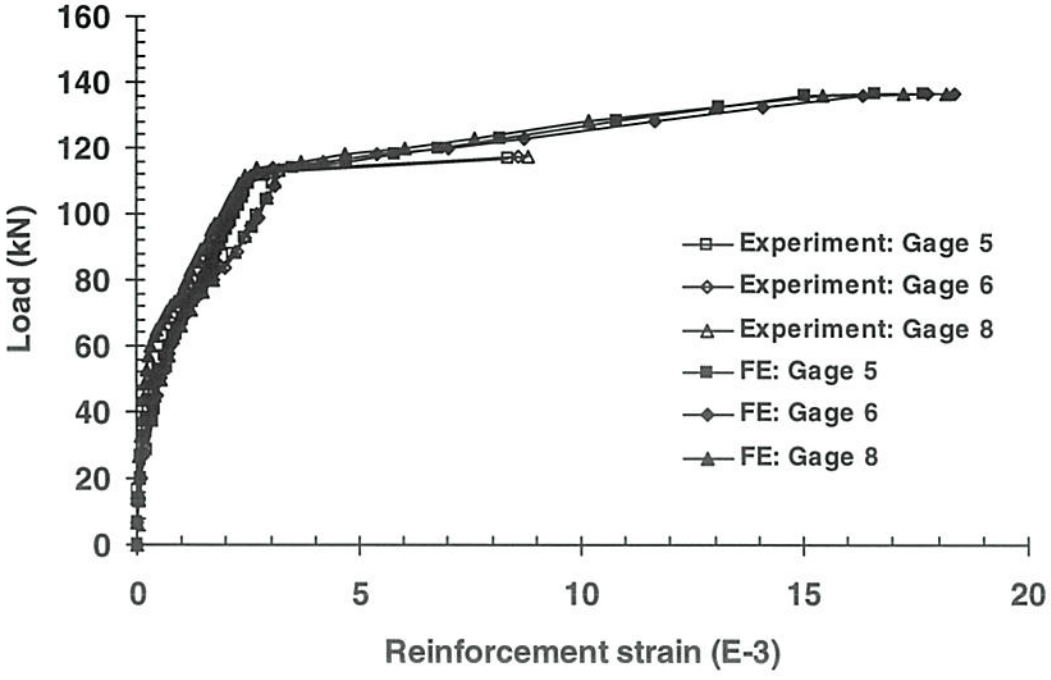

Figure 6.37 – Load versus reinforcement strain history for Specimen S4.

6.5 Prestressed Concrete Slab-Column connections of Burns and Hemakom (1977)

Burns and Hemakom (1977) conducted tests on a 1/3 scale specimen of prestressed concrete slab-column system. The specimen consisted of a 74 mm thick slab resting on 16 short columns representing a 3-bay frame structure in each direction (shown in Figure 6.38). Bonded reinforcing bars were used only in the negative moment regions (see Figure 6.39) with all positive moment reinforcement being unbonded prestressed tendons. The arrangements of the tendons were as shown in Figure 6.40. The slab was uniformly loaded and unloaded a number of times, with 16 different loading patterns, before being tested to destruction. In this study only the uniform load wad modelled.

For the purpose of the analysis the overhang potion of the slab was neglected and one quarter of slab was modelled with symmetry. The cable profile is also taken as symmetrical. The finite element mesh used is shown in Figure 6.41. The slab was modelled using 1282 twenty-node solid isoparametric elements with 7520 nodes. The bonded reinforcement was modelled as two-node embedded bars and the straight and curved tendons were modelled as embedded two-node and three-node unbonded bars, respectively. Additional 216 nodes were used to define the bonded bars and 310 nodes for the unbounded tendons.

The parameters used to define the concrete model were:

f_{cp} = 30.6 MPa	f_t = 1.92 MPa	E_c = 29.0 GPa
α_1 = 14.0	β = 0.2	$\phi = 30^0$
$\alpha = 15^0$	$\psi = 12.6^0$	μ = 0.2
ε_0 = 0.002		

with the in situ concrete strength was taken as $0.9f_{cm}$. The reported cylinder strength was 34.0 MPa. The properties of the non-prestressed reinforcement and tendons used in the test are given in Table 6.10 and Table 6.11.

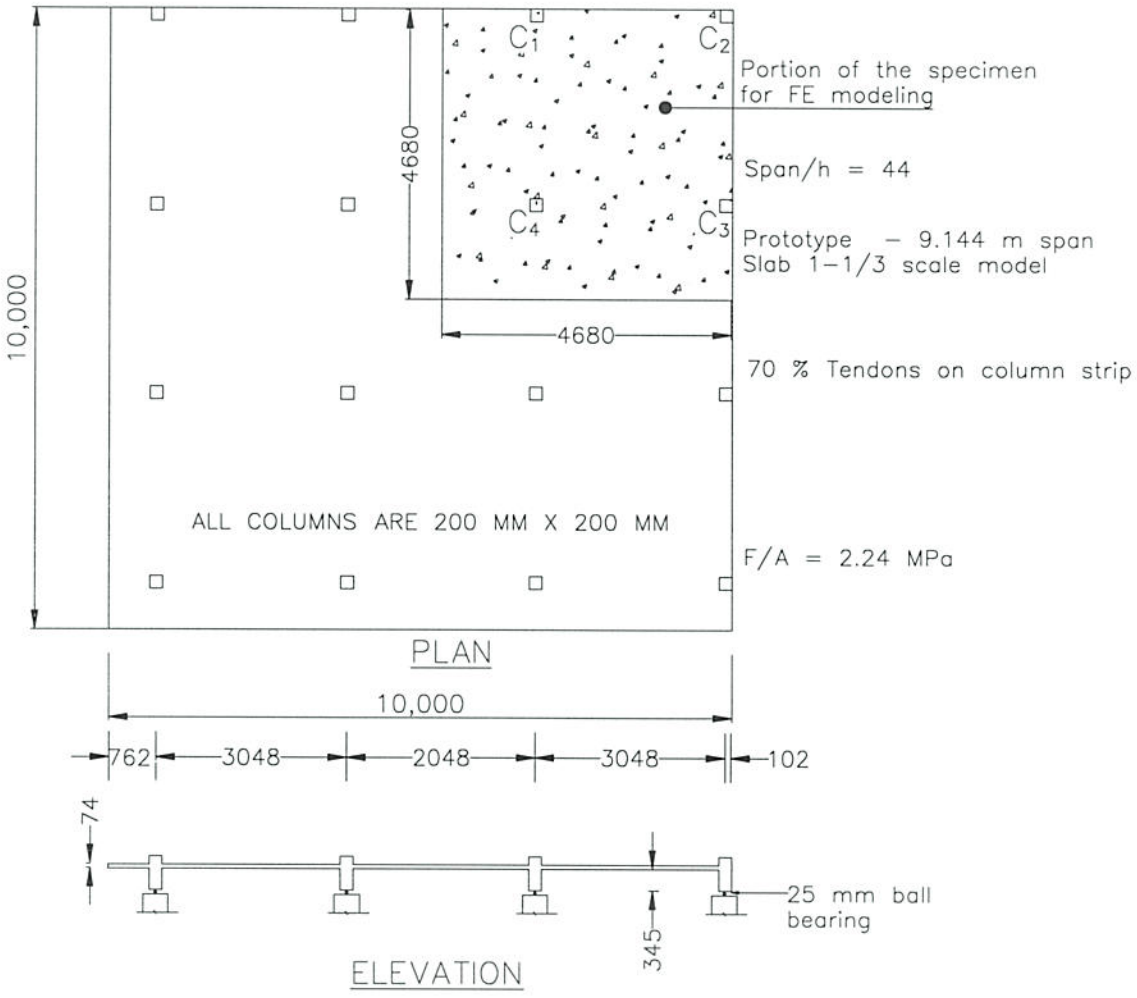

Figure 6.38 – Plan and elevation of slab-column connection with the portion used for finite element analyses for the Burns and Hemakom (1977) slab.

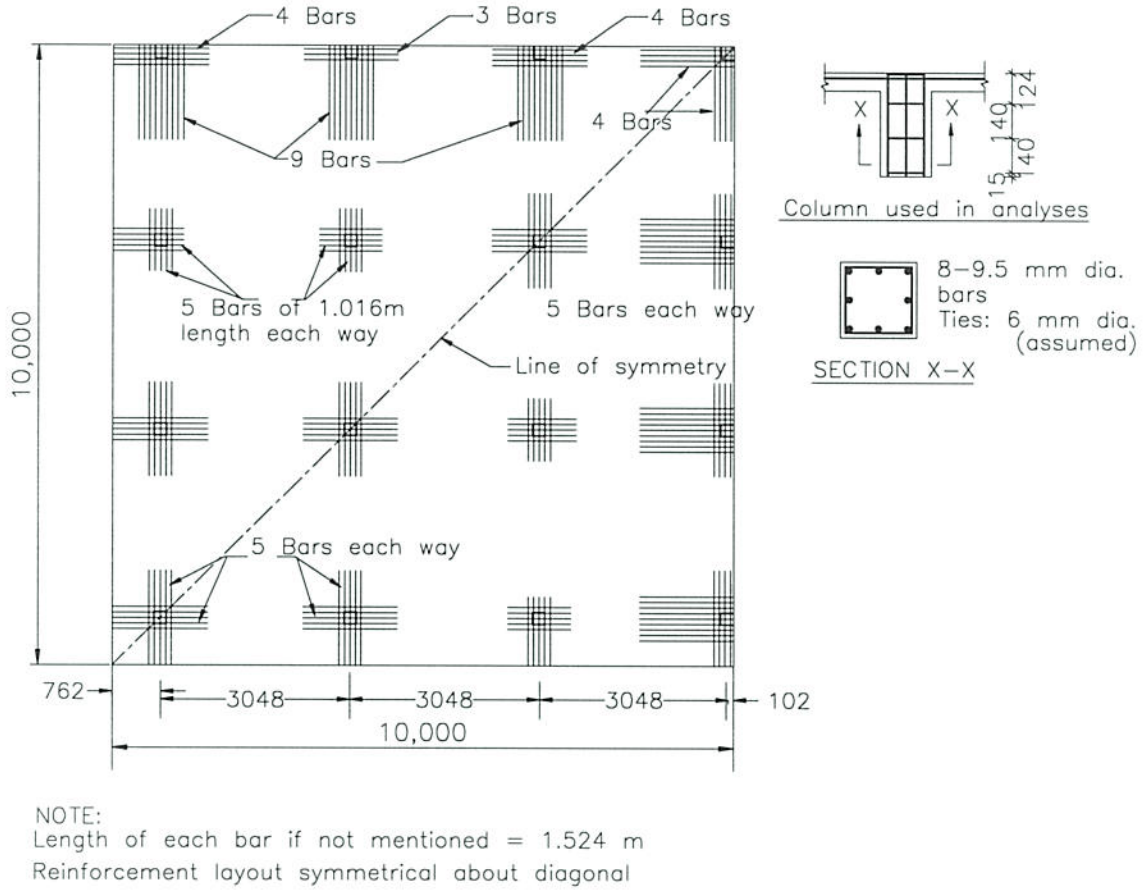

NOTE:
Length of each bar if not mentioned = 1.524 m
Reinforcement layout symmetrical about diagonal

Figure 6.39 – Arrangement of bonded reinforcement (Burns and Hemakom, 1977).

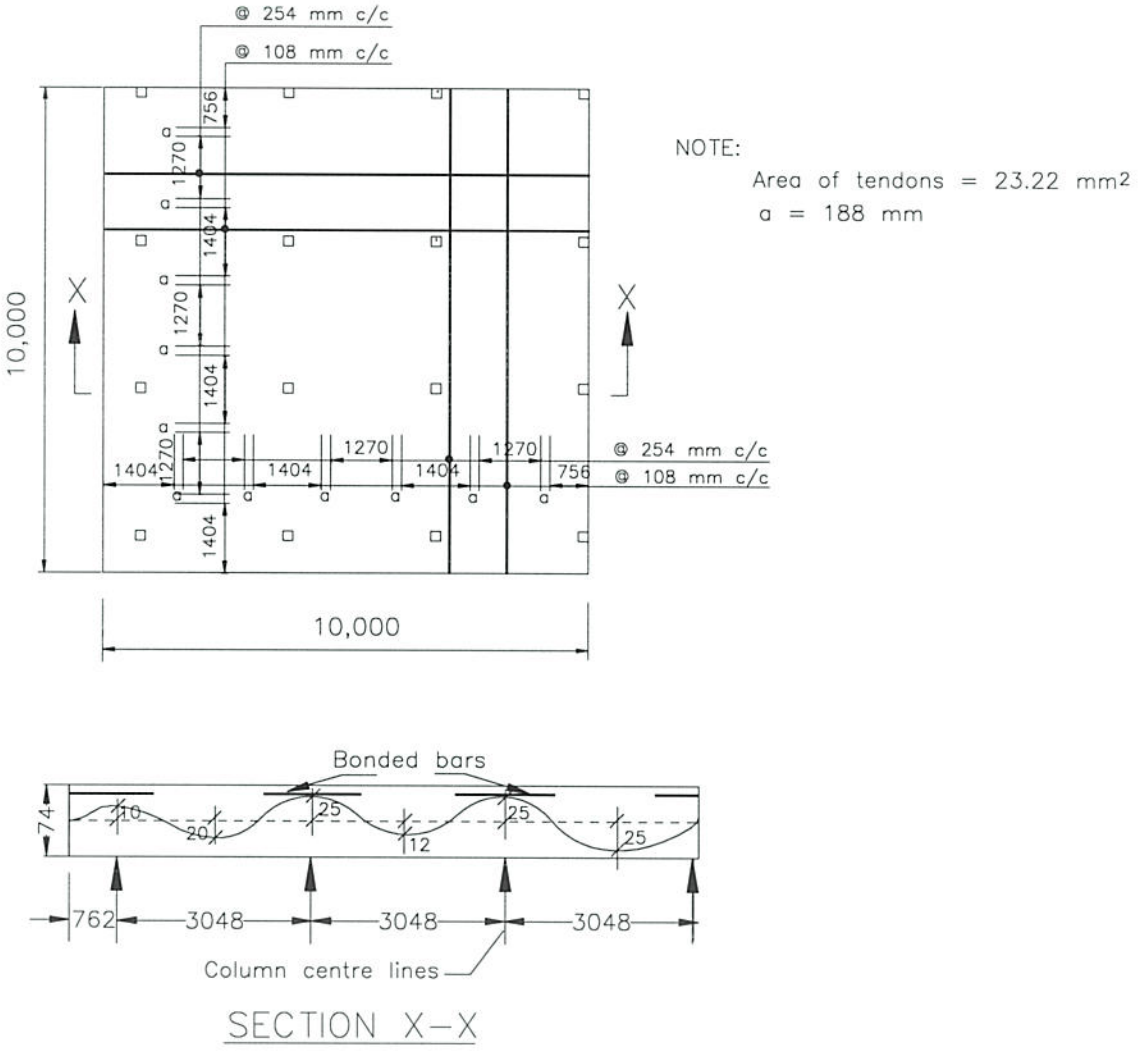

Figure 6.40 – Tendon arrangements (Burns and Hemakom, 1977).

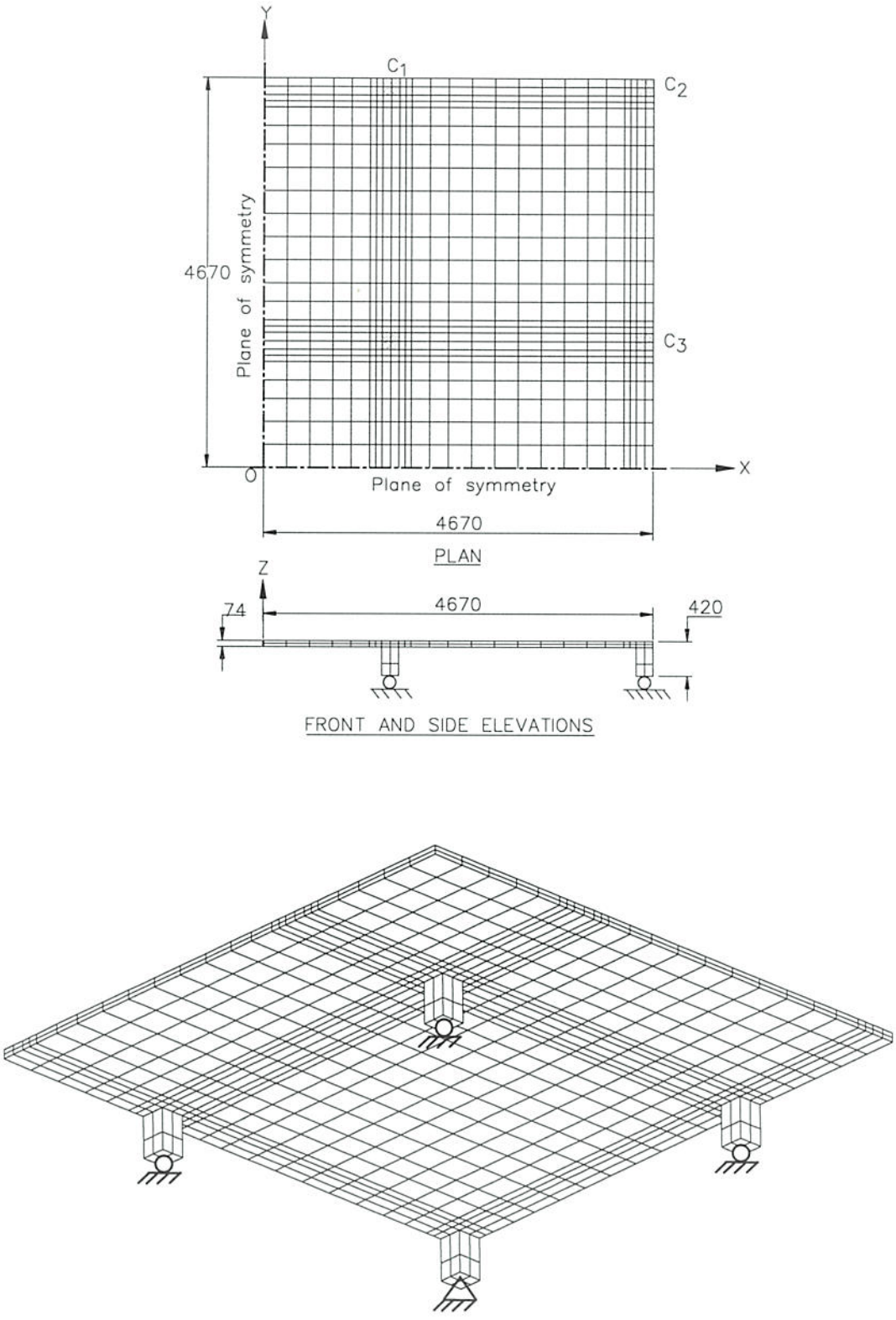

Figure 6.41 - Finite element model of Burns and Hemakom (1977) slab-column (Plan, elevations and 3D view with boundary from below).

Table 6.10 – Material properties of reinforcing steel (Burns and Hemakom 1977).

Material Property		Bars	
		# 2	# 3
Area A_s	(mm^2)	32	71
Yield strength	(MPa)	380	280
Young's modulus	(MPa)	200	200

Table 6.11 – Material properties of 3/8 inch -7 wire strand tendons (Burns and Hemakom, 1977).

Property		Value
Area A_s	(mm^2)	23.2
Yield strength	(MPa)	1725
Young's modulus	(GPa)	200

The locations of main points to measure the deflection (point C) and strain in steel (gage 1 and 2) are shown in Figure 6.42. Figure 6.43 compares the load versus mid-panel deflection response at C (see Figure 6.42) from the finite element model with the experimental data. A good correlation is observed. The failure load obtained in the finite element model was 9.8 kPa and compares well with the experimental result of 9.9 kPa. Calculated from the strains measured in the steel of the columns, the reaction in column C4 at failure was reported to be 150 kN. In the finite element model the load in column C4 at failure was 159 kN, within 6 percent of the experimental result.

No strain histories were gauged in the test. The maximum strain developed at key reinforcements locations in the finite element analyses are shown in Figure 6.42. The load versus strain plots in the bonded reinforcement for the FE model at these locations are shown in Figure 6.44. The plots show that these bars had yielded before failure. In the test the slab was reported to have failed by punching at the interior column connection C4. The FE results predict that the slab failed in flexure followed by punching failure at the interior column C4.

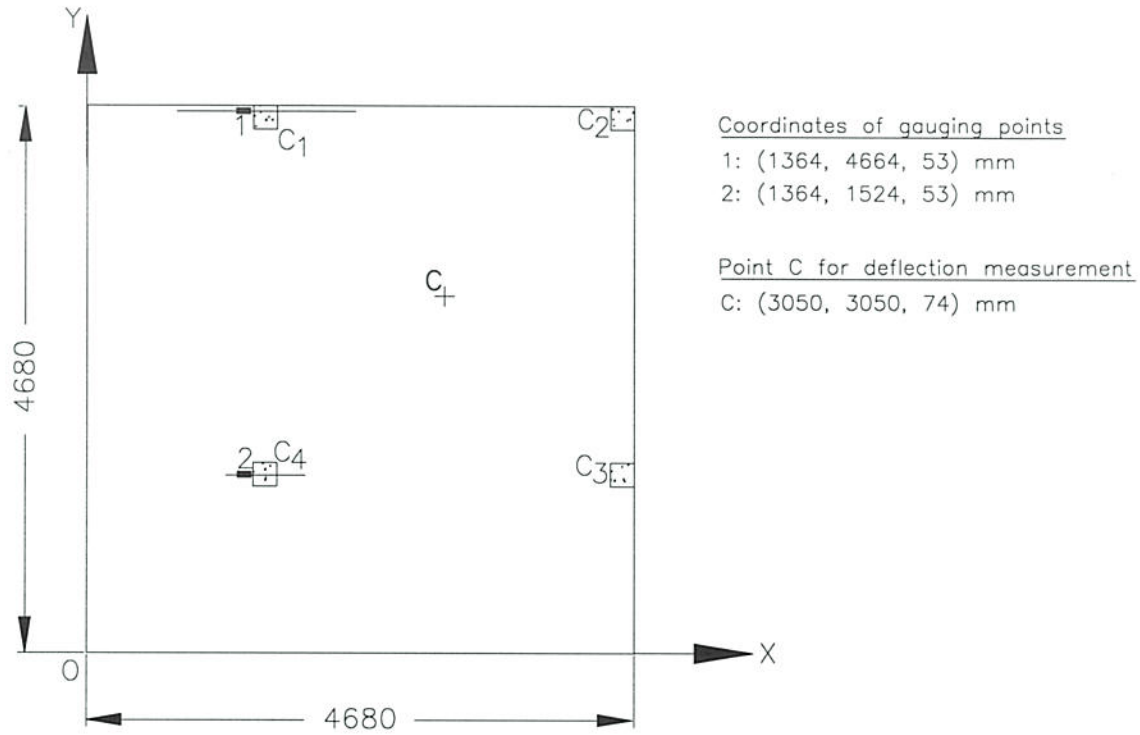

Figure 6.42 – Location of strain points for finite element analysis of Burns and Hemakom (1977) slab.

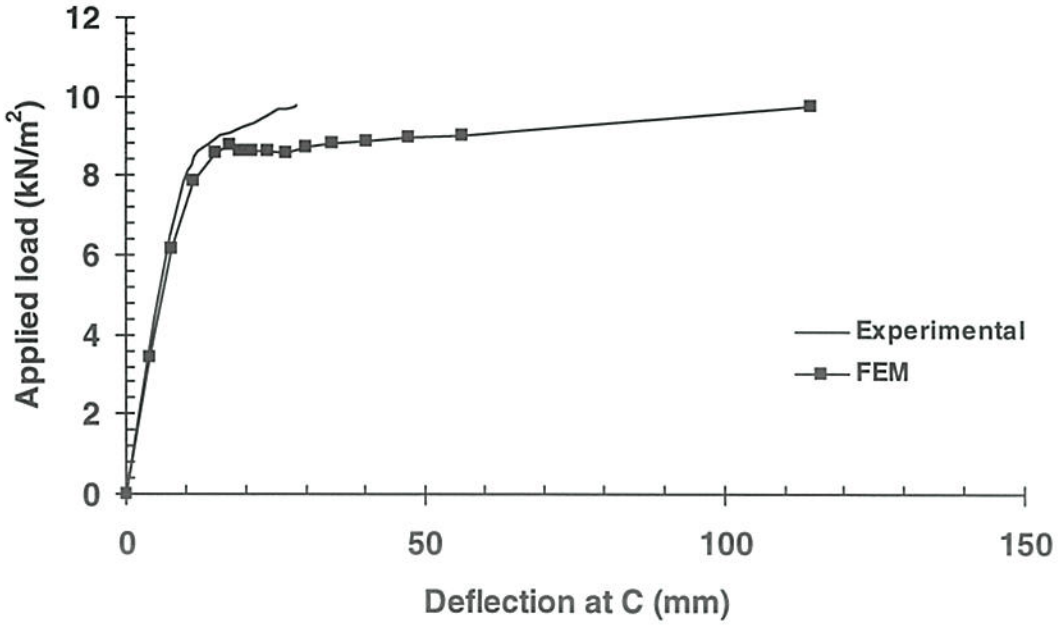

Figure 6.43 – Load deflection curves for the Burns and Hemakom (1977) slab.

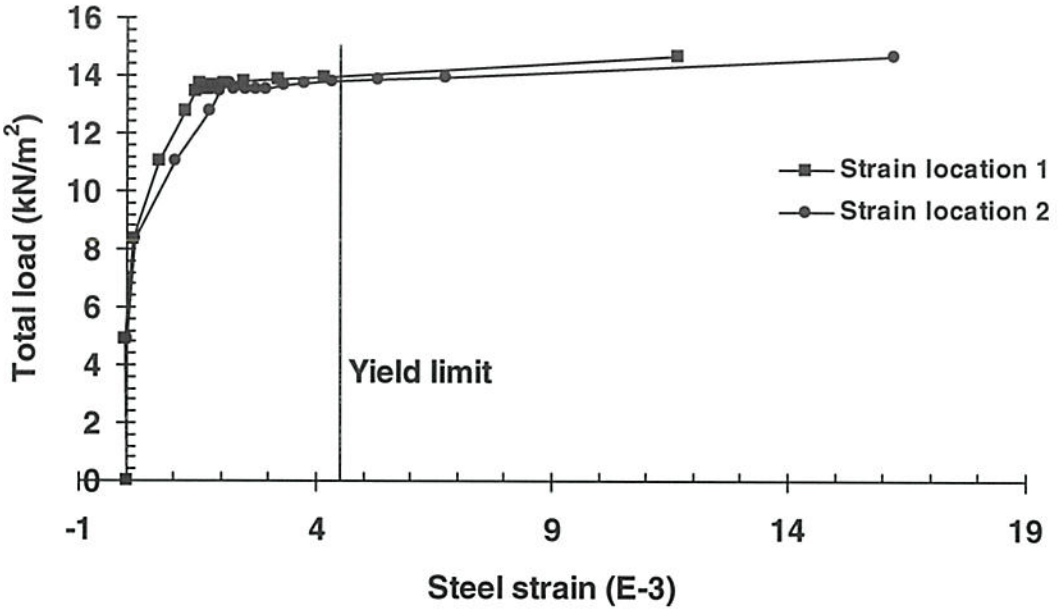

Figure 6.44 – Load versus strain curves for bonded bars in the negative moment region of the slab.

6.6 Conclusions

In this study finite element models were developed for beams and slab-column connections reported to have failed in shear-torsion or punching shear mode from four experimental studies. The overall observation is that finite element modelling is able to compute the failure loads and failure modes of the experiments. Measured data such as load versus deflection for example, were shown to correlate well for the numerical and the experimental results.

From this study it is concluded that the finite element models used in DIANA (1997) give reasonable results within a tolerable range. However, the studies must be accompanied with parameter sensitivity analyses. In particular the softening slope of the stress-strain curve for the concrete in tension was shown to dramatically effect the flexural response of the slabs and the shear retention factor was shown to highly influence the failure load, particularly for slabs failing in punching shear. In conclusion the model can be used for studying the behaviour of slabs failing in punching shear provided that it is appropriately calibrated and verified.

7 Conclusions

In this study the suitability of using the 20-node concrete brick element of DIANA (1997) is assessed for the modelling of concrete slabs failing in punching mode. It was shown that the pattern and the size of mesh, including that through the thickness of the slab, have significant influence on the results of the finite element analyses. To obtain an appropriate level of accuracy a fine mesh (in plan) is required within the critical region of the connection with an aspect ratio in plan of not greater than two. Two elements through the thickness of the slab with integration over an 8-point Gauusian quadrature was found to give a reasonable level of accuracy combined with the efficiency of solution.

The finite element model was shown to be sensitive to the shear retention factor β and strain for zero stress of the concrete in tension, ε_u. The shear retention factor was found to significantly influence the failure load. The strain for zero tension strength influences the load deflection response of the structures via tension stiffening.

In conclusion, the 20-node brick element and embedded bar elements of DIANA are capable of modelling punching shear failure in concrete slab-column connections provided that the model is calibrated for the structure being investigated.

References

Abdel Rahman, H. H. (1982). "Computational models for the nonlinear analysis of reinforced concrete flexural concrete slab systems", Doctoral thesis, University College of Swansea, Swansea, United Kingdom.

ACI 318 (1999)."Building code requirements for structural concrete (ACI 318M-99) and commentary (ACI 318RM-99)", American Concrete Institute, Michigan, 391 pp.

Al-Manaseer, A. A., and Philips, D. V. (1987). "Numerical study of some post-cracking material parameters affecting nonlinear solutions in RC deep beams", Canadian Journal of Civil Engineering, Vol. 14, pp. 655-666.

AS 3600 (1994). "Australian standard for concrete structures", Sydney, 154 pp.

Barzegar, F. (1989). "Analysis of RC membrane elements with anisotropic reinforcement", Journal of Structural Engineering, Vol. 115, No. 3, March, pp. 647-665.

Barzegar, F., and Schnobrich, W. C. (1990). "Post-cracking analysis of reinforced concrete panels including tension stiffening", Canadian Journal of Civil Engineering, Vol. 17, pp. 311-320.

Bazant, Z. P., and Oh, B. P. (1983). "Spacing of cracks in reinforced concrete", Journal of Structural Engineering, ASCE, Vol.109, No. 9, September, pp. 2066-2085.

Bazant, Z. P., and Oh, B. P. (1984). "Numerical simulation of progressive fracture in concrete structures: Recent developments", Proceedings, International Conference on Computer Aided Analysis and Design of Concrete Structures, Pineridge Press, Swansea, 1984, pp. 1-18.

Burns, N. H., and Hemakom, R., (1977). "Test of a scale model post-tensioned flat plate", Journal of the Structural Division, ASCE, Vol. 103, No. ST6, June, pp. 1237-1255.

Channakeshava, C., and Iyengar, K. T. S. R. (1988). "Elasto-Plastic cracking analysis of reinforced concrete", Journal of Structural Engineering, Vol. 114, No. 11, November, pp. 2421 – 2438.

Chen, W.F., and Han, D. J. (1988). "Plasticity for structural engineers", Springer-Verlag, New York, 606 pp.

Chiang, Y. J., and Lee, Y. L. (1994). "Evaluation of modeling accuracy of 20-node solid elements by statistical factorial design." Computers & Structures, Vol. 52, No. 6, pp. 1309 – 1314.

Chiang, Y. J., and Tang, C. (1995). "Accuracy assessment to applying 20-node solid elements to pressurized composite shells." Finite Elements in Analysis and Design, Vol. 20, pp. 219 – 231.

Cope, R. J., (1986). "Nonlinear analyses of reinforced concrete slabs." Computer Modelling of RC structures, Pineridge Press, Swansea, pp. 3-43.

de Borst, R., and Nauta, P. (1985). "Non-orthogonal cracks in a smeared finite element model", Engineering Computations, March, Vol. 2, pp. 35-46.

DIANA.- Release 6.2 (1997). TNO Building and Construction Research, Delft, The Netherlands.

Eurocode 2(1992). "Design of concrete structures – Part I: General rules and rules for buildings", European Committee for Standardization, Brussels.

Foster, S. J., (1992). "The structural behaviour of reinforced concrete deep beams" Doctoral thesis, School of Civil Engineering, The University of New South Wales, Sydney, Australia.

Foutch D. A., Gamble, W. L., and Sunidja, H. (1990) "Tests of post-tensioned concrete slab-edge column connections", ACI Structural Journal, March-April, Vol. 87, No. 2, pp. 167-179.

Gilbert, R. I. (1979). "Time dependent behaviour of structural concrete slabs", Doctoral Thesis, School of Civil Engineering, The University of New South Wales, pp. 361.

Gilbert, R. I., and Warner, R. F. (1978) "Tension stiffening in reinforced concrete slabs." ASCE Journal of Structural Division, Vol. 104, ST12, December, pp. 1885-1900.

Hemakom, R. (1975). "Strength and behaviour of post-tensioned flat plates with unbonded tendons", Doctoral Thesis, University of Texas, Austin, 272 pp.

Hognestad, E. (1951). "A study of combined bending and axial load in reinforced concrete members", University of Illinois Engineering Experimental Station, Bulletin Series No. 399, November, 128 pp.

Hu, H. H., and Schnobrich, W. C., (1988). "Nonlinear analyses of plane stress state reinforced under short time monotonic loading", Civil Engineering Studies, SRS No. 539, University of Illinois, Urbana, April.

Lim, K. F., and Rangan, B. V. (1995). "Studies on concrete slabs with stud shear reinforcement in vicinity of edge and corner columns", ACI Structural Journal, Vol. 92, No. 5, September-October, pp. 515-525.

Lin, C. S., (1973). "Nonlinear analysis of reinforced concrete slabs and shells", Doctoral Thesis, UC_SESM 73-7, University of California at Berkeley.

Lin, C., and Scordelis, A. C., (1975)."Nonlinear analysis of RC shells of general form", Proceedings ASCE, Vol. 101, ST3, March, pp. 523-538.

Mansur, M. A., and Rangan, B. V. (1978). "Torsion in spandrel beams", Journal of Structural Division, ASCE, Vol. 104, ST7, pp. 1061-1075.

Nielsen, M. P., Braestrup, M. W., Jensen, B. C., and Bach, F. (1978). "Concrete plasticity", Specialpublikation udgivet af Dansk Selskab, October, 129 pp.

Noor, A. K., and Babuska, I. (1987). "Quality assessment and control of finite element solutions", Finite Elements in Analysis and Design 3, pp. 1 – 26.

Ockleston, A. J. (1955). "Load test on a three storey reinforced concrete building in Johannesburg", Structural Engineer, London, Vol. 33, No. 10, October, pp. 304-322.

Park, R., and Gamble, W. L. (1980). "Reinforced Concrete Slabs", John Wiley & Sons, New York, 618 pp.

Petersson, P. E., and Gustavasson, P. J., (1980). "Numerical methods in fracture mechanics", Pineridge Press, Swansea, pp. 707-719.

Prakhya, G. K. V., and Morley, C. T., (1990). "Tension stiffening and moment-curvature relation of reinforced concrete elements" ACI Structural Journal, Vol. 87, No. 5, September-October, pp. 597-605.

Rangan, B. V., and Lim, F. K., "Test on concrete slabs with stud shear reinforcement in the vicinity of edge columns." Research Report No. 1/92, School of Civil Engineering, Curtin University of Technology, Perth, May 1992, 140 pp.

Roddeman, D. G., and Jansen L. F. (1993). "An a priori geometry check for a single isoparametric finite element", Computers & Structures, Vol. 47, No. 1, pp. 69 – 72.

Rots, J. G. (1988). "Computational Modeling of Concrete Fracture", Doctoral Dissertation, Delft University of Technology, The Netherlands, 134 pp.

Rots, J. G., Nauta, P., and Kusters, G. M. A., and Blaauwendraad, J. (1985) "Smeared crack approach and fracture localization in concrete", HERON, Vol. 30, No. 1, 48 pp.

Scanlon, A., (1971). "Time dependent deflection of reinforced concrete slabs" Doctoral thesis, University of Alberta, Edmonton, 174 pp.

Schnobrich, W. C. (1977). "Behavior of reinforced concrete structures predicted by the finite element method", Computers & Structures, Vol. 7, pp. 365 – 376.

Sih, G. C., and DiTommaso, A., (1985) (Editors), "Fracture mechanics of concrete: Structural application and numerical calculation", Martinus Nijhoff Publishers, Dordrecht, 276 pp.

Suidan, M., and Schnobrich, W. C. (1973). "Finite element analysis of reinforced concrete", ASCE Proceedings, Journal of Structural division, Vol. 99, ST10, October, pp. 2109 – 2121.

Sunidja, H., Foutch, D. A., and Gamble, W. L. (1982). "Response of prestressed concrete plate-edge column connections", Civil Engineering Studies, Structural Research Series No. 498, University of Illinois, Urbana, and March, 232 pp.

Swamy, R. N., and Andriopoulos, A. D., (1974). "Contribution of aggregate interlock and dowel forces to the shear resistance of reinforced beam with web reinforcement", SP 42.6 ACI Publication on Shear in Reinforced Concrete, Detroit, pp. 129-166.

van Mier, J. G. M. (1987). "Examples of non-linear analysis of reinforced concrete structures with DIANA", HERON, Volume 32, No. 3, 147 pp.

Vecchio, F. J., and Collins, M. P. (1990). "Investigating the collapse of a warehouse", Concrete International, Vol. 12, No. 3, March, pp. 72-78.

Vermeer, P. A., and de Borst, R. (1984). "Non-associated plasticity for soils, concrete and rock", HERON, Vol. 29, No. 3, 65 pp.